THESIS FOR THE DEGREE OF DOCTOR OF PHILOSOPHY

Fabrication and characterization of graphene-superconductor devices

NICLAS LINDVALL

Department of Microtechnology and Nanoscience
CHALMERS UNIVERSITY OF TECHNOLOGY
Göteborg, Sweden 2015

Fabrication and characterization of graphene-superconductor devices
NICLAS LINDVALL

ISBN 978-91-7597-248-0

Doktorsavhandlingar vid Chalmers Tekniska Högskola
Ny serie nr 3929
ISSN 0346-718X

ISSN 1652-0769
Technical report MC2-316

Quantum Device Physics Laboratory
Department of Microtechnology and Nanoscience (MC2)
Chalmers University of Technology
SE-412 96 Göteborg, Sweden
Phone: +46 (0)31-772 1000

Printed by Chalmers Reproservice
Göteborg, Sweden 2015

Fabrication and characterization of graphene-superconductor devices

NICLAS LINDVALL
Department of Microtechnology and Nanoscience (MC2)
Chalmers University of Technology, 2015

Abstract

Graphene is the first single-atom-thick two-dimensional material and exhibits a large set of interesting properties. This thesis consists of two parts. The first regards the growth of large-area graphene using chemical vapor deposition (CVD). Graphene is grown using CVD on copper catalyst showing high quality with charge carrier mobility exceeding 3000 cm^2/Vs.

Wet chemical etching is used to transfer graphene to insulating substrates. Cu is removed using either diluted HNO_3 or diluted HCl with a small amount of added H_2O_2. To allow for faster transfer and avoid consuming copper, a hydrogen-bubbling method is developed to delaminate graphene from Cu. Graphene transferred this way shows properties similar to those of graphene transferred using wet etching.

To avoid transfer-related issues, graphene is grown non-catalytically directly on insulating substrates such as SiO_2, Al_2O_3, and Si_3N_4. The grain size is only ~10 nm due to the lack of catalytic activity during growth. Such graphene shows inferior electronic properties with mobility in the order of ~tens of cm^2/Vs. Despite that, sheet resistance around kΩ, the possibility to grow several layer thick films, and optical properties similar to those of pristine graphene make it an interesting material.

A method for cleaning graphene mechanically using atomic force microscopy (AFM) is developed. By appropriate choice of the applied force, atomically smooth (roughness < 0.2 nm) graphene with improved mobility and reduced doping is achieved.

The second part of this thesis considers experiments combining graphene and superconductors. A graphene-based cold-electron bolometer is realized using graphene as absorber material. It shows response to 100 GHz radiation at 300 mK and a temperature responsivity of ~0.4 μV/mK at 300 mK.

The Aharonov-Bohm effect is studied in graphene having superconducting or normal metal mirrors. The mirrors improve the visibility of the Aharonov-Bohm oscillations, and up to third order oscillations are observed.

Weak localization in inhomogeneous magnetic fields is studied in graphene by putting it in close proximity to a type-II superconductor. A deviation from the homogeneous result is observed for fields smaller than the characteristic field B_φ.

Keywords: Graphene, Chemical vapor deposition, Synthesis, Mechanical cleaning, Atomic force microscopy, Bolometer, Aharonov-Bohm effect, Weak localization

This thesis is based partly on the following scientific papers:

I. J. Sun, N. Lindvall, M. Cole, K. Angel, T. Wang, K. Teo, D. Chua, J. Liu, and A. Yurgens, "Low partial pressure chemical vapor deposition of graphene on copper", IEEE Trans. Nanotechnol. vol. **11**, pp 255-260, 2012.

II. C. Lockhart de la Rosa, J. Sun, N. Lindvall, M. T. Cole, Y. Nam, M. Löffler, E. Olsson, K. B. K. Teo, and A. Yurgens, "Frame assisted H_2O electrolysis induced H_2 bubbling transfer of large area graphene grown by chemical vapor deposition on Cu", Appl. Phys. Lett. vol. **102**, p. 022101, 2013.

III. J. Sun, N. Lindvall, M. T. Cole, K. B. K. Teo, and A. Yurgens, "Large-area uniform graphene-like thin films grown by chemical vapor deposition directly on silicon nitride", Appl. Phys. Lett. vol. **98**, p. 252107, 2011.

IV. N. Lindvall, J. Sun, G. Abdul, and A. Yurgens, "Towards transfer-free fabrication of graphene nanoelectromechanical systems grown by chemical vapour deposition", Micro Nano Lett. vol. **7**, pp 749-752, 2012.

V. N. Lindvall, A. Kalabukhov, and A. Yurgens, "Cleaning graphene using atomic force microscope", J. Appl. Phys. vol. **111**, pp 064904-064904, 2012.

VI. M. Tarasov, N. Lindvall, L. Kuzmin, and A. Yurgens, "Family of graphene-based superconducting devices", JETP Lett. vol. **94**, pp 329-332, 2011.

VII. Y. Nam, J. S. Yoo, Y. W. Park, N. Lindvall, T. Bauch, and A. Yurgens, "The Aharonov-Bohm effect in graphene with metal mirrors", Carbon vol. **50**, pp 5562-5568, 2012.

VIII. N. Lindvall, A. Shivayogimath, and A. Yurgens, "Measurements of weak localization of graphene in inhomogeneous magnetic fields", accepted for publication in JETP Lett., 2015.

My contribution to these papers was as follows:

I. JS, TW, and I did the sample fabrication. JS, AY, and I did electrical characterization. MC and KT did Raman measurements. KA and DC did TEM characterization. JS wrote the paper with input from the co-authors.

II. CL, JS, and I did the sample fabrication. CR, JS, YN, AY, and I did the electrical characterization. CL, MC, ML, EO, and KT did the microscopy measurements. CL and JS wrote the paper.

III. JS and I did sample fabrication. MC and KT provided Raman characterization. JS, AY, and I did the electrical characterization. JS wrote the paper and completed the submission procedure with the help of the co-authors.

IV. I, JS, and AY developed the idea. JS, GA, and I did the sample fabrication. I did the measurements and wrote the paper.

V. I was responsible for the idea behind the paper. AK and I worked on sample fabrication. I did the measurements and data analysis. AY gave input on the data analysis. I wrote the paper with input from the co-authors and completed the submission.

VI. I did the sample fabrication and process development. MT and I did the measurements. MT wrote the paper.

VII. YN, JY, and I did the sample fabrication. YN, TB, AY, and I performed the measurements. YN wrote the paper with input from the co-authors.

VIII. AS and I did the sample fabrication. AY and I did the electrical measurements. I wrote the paper.

Other scientific papers that are outside the scope of this thesis:

IX. J. Svensson, N. Lindahl, H. Yun, M. Seo, D. Midtvedt, Y. Tarakanov, N. Lindvall, O. Nerushev, J. Kinaret, S. Lee, and E. E. B. Campbell, "Carbon nanotube field effect transistors with suspended graphene gates", Nano Lett. vol. **11**, pp 3569-3575, 2011.

X. J. Sun, M. T. Cole, N. Lindvall, K. B. K. Teo, and A. Yurgens, "Noncatalytic chemical vapor deposition of graphene on high-temperature substrates for transparent electrodes", Appl. Phys. Lett. vol. **100**, p. 022102, 2012.

XI. J. Sun, N. Lindvall, M. T. Cole, T. Wang, T. J. Booth, P. Boggild, K. B. K. Teo, J. Liu, and A. Yurgens, "Controllable chemical vapor deposition of large area uniform nanocrystalline graphene directly on silicon dioxide", J. Appl. Phys. vol. **111**, p. 044103, 2012.

XII. J. Sun, M. T. Cole, S. A. Ahmad, O. Bäcke, T. Ive, M. Löffler, N. Lindvall, E. Olsson, K. B. K. Teo, J. Liu, A. Larsson, A. Yurgens, and Å. Haglund, "Direct chemical vapor deposition of large-area carbon thin films on gallium nitride for transparent electrodes: A first attempt", IEEE Trans. Semicond. Manuf. vol. **25**, pp 494-501, 2012.

XIII. Y. Fu, B. Carlberg, N. Lindahl, N. Lindvall, J. Bielecki, A. Matic, Y. Song, Z. Hu, Z. Lai, L. Ye, J. Sun, Y. Zhang, Y. Zhang, and J. Liu, "Templated Growth of Covalently Bonded Three-Dimensional Carbon Nanotube Networks Originated from Graphene", Adv. Mater. vol. **24**, pp 1576-1581, 2012.

XIV. N. Lindahl, D. Midtvedt, J. Svensson, O. A. Nerushev, N. Lindvall, A. Isacsson, and E. E. B. Campbell, "Determination of the bending rigidity of graphene via electrostatic actuation of buckled membranes", Nano Lett. vol. **12**, pp 3526-3531, 2012.

XV. Y. Nam, N. Lindvall, J. Sun, Y. W. Park, and A. Yurgens, "Graphene p–n–p junctions controlled by local gates made of naturally oxidized thin aluminium films", Carbon vol. **50**, pp 1987-1992, 2012.

XVI. Y. Nam, J. Sun, N. Lindvall, S. J. Yang, D. Kireev, C. R. Park, Y. W. Park, and A. Yurgens, "Quantum Hall effect in graphene decorated with disordered multilayer patches", Appl. Phys. Lett. vol. **103**, p. 233110, 2013.

XVII. A. Yurgens, N. Lindvall, J. Sun, Y. Nam, and Y. W. Park, "Control of graphene Dirac point by UV light", JETP Lett. vol. **98**, pp 704-708, 2013.

XVIII. R. Sellappan, J. Sun, A. Galeckas, N. Lindvall, A. Yurgens, A. Y. Kuznetsov, and D. Chakarov, "Influence of graphene synthesizing techniques on the photocatalytic performance of graphene-TiO_2 nanocomposites", Phys. Chem. Chem. Phys. vol. **15**, pp 15528-15537, 2013.

XIX. Y. Nam, J. Sun, N. Lindvall, S. J. Yang, C. R. Park, Y. W. Park, and A. Yurgens, "Unusual thermopower of inhomogeneous graphene grown by chemical vapor deposition", Appl. Phys. Lett. vol. **104**, p. 021902, 2014.

XX. J. Sun, Y. Nam, N. Lindvall, M. T. Cole, K. B. K. Teo, Y. W. Park, and A. Yurgens, “Growth mechanism of graphene on platinum: Surface catalysis and carbon segregation”, Appl. Phys. Lett. vol. **104**, p. 152107, 2014.

XXI. M. Wiesner, N. Lindvall, and A. Yurgens, “Detection of graphene microelectromechanical system resonance”, J. Appl. Phys. vol. **116**, p. 224510, 2014.

XXII. A. Cagliani, N. Lindvall, M. B. B. S. Larsen, D. M. A. Mackenzie, B. S. Jessen, T. J. Booth, and P. Boggild, “Defect/oxygen assisted direct write technique for nanopatterning graphene”, Nanoscale vol. **7**, pp 6271-6277, 2015.

XXIII. Z. Zhan, J. Sun, L. Liu, E. Wang, Y. Cao, N. Lindvall, G. Skoblin, and A. Yurgens, “Pore-free bubbling delamination of chemical vapor deposited graphene from copper foils”, J. Mater. Chem. C vol. **3**, pp 8634-8641, 2015.

List of symbols

a	loop area
A	overlapping area of graphene and gate electrode
$\mathbf{A}$	magnetic vector potential
b_0	magnetic field magnitude inside flux tube
B	scalar magnetic flux density
$\boldsymbol{B}$	magnetic field vector
B_φ	characteristic inelastic field
$B_{i,*}$	characteristic elastic fields
C	cantilever spring constant
C_g	specific gate capacitance
d	thickness of dielectric
e	elementary charge
E	energy of charge carriers
E_F	Fermi energy
g_s	degeneracy factor
H_c1	lower critical field
I	electric current
I_2D, I_D, I_G	Raman intensity of 2D peak, D peak, G peak
$\tilde{I}_\mathrm{op}$	reflected light intensity
k_x, k_y	wave vector components for charge carriers
l	integer index
L	sample length
L_φ	(inelastic) phase coherence length
$L_{i,*}$	elastic scattering lengths
n	charge carrier number concentration
n_0	residual charge carrier concentration
n_g	charge carrier concentration induced by gate
$\tilde{n}_\mathrm{i}$	refractive index of material layer i
N	index of Aharonov-Bohm oscillations
N_sq	number of geometrical squares
q	carrier charge (either $+e$ or $-e$)
r_0	radius of flux tube
r_1, r_2, r_3	relative indices of refraction
R	electrical resistance
R_0	constant in graphene resistance model
R_H	Hall coefficient
R_RMS	root mean square height
R_s	sheet resistance
R_{xx}	longitudinal resistance
R_{xy}	transversal resistance
T	temperature
T_c	critical temperature of a superconductor
V_D	Dirac voltage
V_g	gate voltage

V_{xx}	longitudinal voltage
V_{xy}	transversal voltage, Hall voltage
W	sample width
ε_r	relative permittivity
λ	optical wavelength
μ	charge carrier mobility
$\tilde{\mu}$	approximate charge carrier mobility
ρ_{xx}	longitudinal resistivity
ρ_{xy}	Hall resistivity
σ	electrical conductivity
v_F	Fermi velocity for graphene
φ	charge carrier phase
Φ_i	optical phase shift
Ψ	digamma function

List of abbreviations

0D, 1D, 2D, 3D	zero-, one-, two-, three-dimensional
2DEGs	two-dimensional electron gases
AFM	atomic force microscopy
ALD	atomic layer deposition
BOE	buffered oxide etch
BSTO	barium strontium titanate
CEB	cold-electron bolometer
CNT	carbon nanotube
CVD	chemical vapor deposition
DOS	density of states
EBL	electron beam lithography
ESD	electrostatic discharge
FFT	fast Fourier transform
FWHM	full width at half maximum
HOPG	highly ordered pyrolytic graphite
ICT	information and communications technology
IQHE	integer quantum Hall effect
LCD	liquid-crystal display
MLG	multilayer graphene
Nb-STO	Nb-doped strontium titanate
NEMS	nanoelectromechanical systems
PET	polyethylene terephthalate
PMMA	polymethyl-methacrylate
RMS	root mean square
SEM	scanning electron microscopy
SIN	superconductor-insulator-normal metal
SINIS	superconductor-insulator-normal metal-insulator-superconductor
TEM	transmission electron microscopy
UCFs	universal conductance fluctuations
WL	weak localization

Contents

1 Introduction

Few materials go from being thought not to be able to exist to Nobel Prize awarded. Graphene is such a material. In 2010, Andre Geim and Konstantin Novoselov from Manchester University were awarded the Nobel Prize in Physics for their groundbreaking experiments on graphene performed only five years earlier [1, 2]. Graphene made it to the headlines, not only in scientific journals but also in mass media. It is easy to understand the interest in this new material. It exhibits extraordinary properties and gives hope to a long list of potential applications. Even more interestingly it opens up a whole new world of two-dimensional (2D) materials.

New technology has historically been a major driving force for the development of our society. One key component in the development of new technology is the discovery of new materials. From the stone-, bronze-, and iron ages, where the material name even followed them into the history books, to modern times with polymers (plastics) and silicon (transistors, electronics), the civilization of that time has been significantly affected by a single technology. At present, in the information and communications technology (ICT) era, there is a seemingly never-ending need for faster computation, greater storage, and higher-bandwidth communication. Certainly, new materials are likely to play a major role in realizing those requirements. Graphene is one of the materials that could possibly play a role in this development.

It is inherently difficult, if not impossible, to predict future technological revolutions. Some key technological challenges can, however, be identified for the future. These include several energy-related problems such as the always increasing need for more of it while reducing the environmental impact, and new types of energy storage systems e.g. better batteries or supercapacitors. We crave for faster, more clever, and more power-efficient electronics, possibly making them flexible and transparent. For these challenges, new materials are needed.

While many materials may share one or maybe two of the properties needed for such future applications, for a material to be truly revolutionary it will need to incorporate many. The material this thesis focuses on, graphene, is hoped to play a

role in not one but several of the above mentioned applications, as well as in many others.

In this thesis, graphene is studied in combination with another class of exotic materials – superconductors. Their properties, such as a having a quantum phase at mesoscopic length scales and a unique magnetic susceptibility, are combined with the two-dimensionality of graphene to study quantum phenomena.

Graphene will be introduced with an overview of its properties and potential applications in Chapter 1.1. In Chapter 1.2, the aim and outline of this thesis are presented.

1.1 Carbon wonder material

Carbon is the building block for all known life on earth. It is the base for the field of organic chemistry. The different forms of carbon have provided great historic importance. All in all, carbon is one of the most versatile and important materials on earth. The versatility of carbon is explained by the many different ways its four valence electrons can form chemical bonds. In its ground state, two of the valence electrons are in s orbitals and two in p orbitals. When forming chemical bonds, the orbitals can hybridize, meaning that one s electron is promoted to a p orbital while one (sp^1-hybridization), two (sp^2-hybridization), or three (sp^3-hybridization) of the p orbitals mix with the other s orbital. In the case of sp^3-hybridization, all four valence electrons form σ bonds. These σ bonds are strong bonds with localized electrons. This is what gives the properties of for example diamond, which is among the hardest materials that exist and is electrically insulating.

For the case of sp^2-hybridized carbon, only three valence electrons form σ bonds while the fourth is in the π orbital. This π electron is not localized and contributes to the electrical conductivity of sp^2-hybridized carbon materials. Among them is graphene.

Graphene is a one atom thick hexagonal lattice of carbon atoms. It is a 2D allotrope of sp^2-hybridized carbon. It can be considered a single layer of graphite and can be viewed as the building block for the other sp^2-hybridized carbon allotropes. These other three allotropes, covering a range of dimensionality, are seen in Figure 1.1: the fullerene (zero-dimensional, 0D), the carbon nanotube (CNT, one-dimensional, 1D), and graphite (three-dimensional, 3D). Very thin pieces of graphite are denoted multilayer graphene (MLG). These have properties different from both single-layer graphene and graphite. In particular, bilayer graphene exhibits electronic properties distinctly different from those of monolayer graphene. To avoid confusion, the term *graphene* is used in the meaning of monolayer graphene in this thesis, unless stated otherwise.

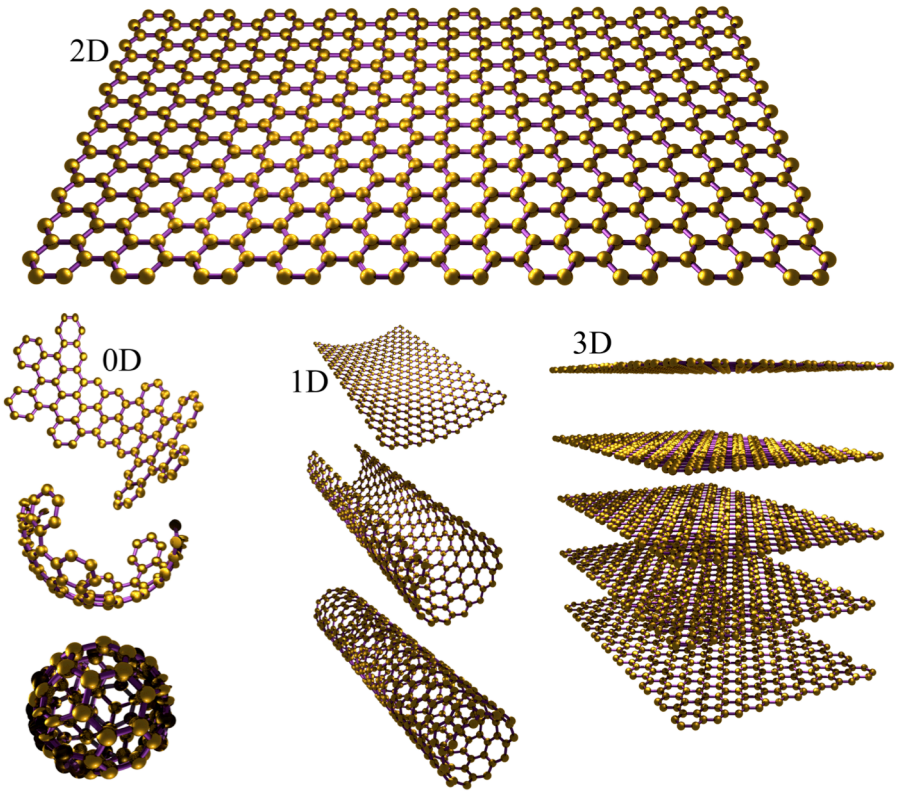

Figure 1.1: Carbon materials of different dimensionality. Graphene (2D, top) is a hexagonal honeycomb lattice of sp^2-hybridized carbon atoms. It can be viewed as a single layer of graphite and the 2D building block for the other sp^2-hybridized carbon allotropes. These are the fullerene (0D, bottom left), the carbon nanotube (1D, bottom center), and graphite (3D, bottom right).

Graphene shares many of its properties with the other allotropes, especially with CNTs. The strong σ bonds are primarily responsible for the mechanical properties, while the π electron can move freely what gives rise to the high electrical conductivity.

While several works from the 1950s and later have reported on the observation of atomically thin graphitic layers [3-5], the formation of atomically thin layers of graphite on silicon carbide [6] and metal substrates [7], it was not until 2004 and 2005 that such layers were isolated and revealed their distinct properties [1, 2, 8]. Geim and Novoselov used a rather primitive technique to produce graphene: exfoliating graphite using sticky tape. Already a few years later, a scalable fabrication technique was developed: chemical vapor deposition (CVD) on Cu [9]. With a seemingly industry-friendly production technique at hand, the interest in graphene increased even further.

It can be argued that a strictly 2D crystal could not exist at any finite temperature because thermal fluctuations would lead to unsustainable atomic displacements [10-12]. Monolayers should only be found as parts of 3D structures. However, with the experiments on the atomic monolayer graphene, it was shown that 2D crystals could indeed exist on non-crystalline substrates, clamped suspended

between support points, and in liquid suspension [1, 2]. As such, they are (almost) freestanding, while remaining thermodynamically stable. Graphene was the first 2D material experimentally realized, constituting an important milestone in Physics.

Graphene is extraordinary, justifying the amount of scientific resources spent on it [13], because it combines several superlative properties in one and the same material. It is atomically thin (the π orbitals span approximately 0.34 nm) with a specific surface area of ~2600 m^2/g [14]. Despite being so thin, it is still impermeable to all elements, even to helium [15]. It is the strongest material measured with Young's modulus of ~1 TPa while being stretchable up to 25 % [16]. Its charge carriers have zero effective mass (imitating the behavior of massless Dirac fermions) and show a charge carrier mobility μ exceeding 10^6 cm^2/Vs [17, 18]. Graphene shows the record thermal conductivity of ~5000 W/m·K [19]. It is also almost transparent (it absorbs ~2.3 % of any visible wavelength) [20] but is still an interesting material for photonic applications [21, 22].

Such exotic combination of properties paves grounds for fundamental studies in Chemistry and Physics but also for an increasing number of technical applications. The most interesting applications combine several of these properties. Figure 1.2 shows six different possible applications, each based on at least two distinct properties of graphene. Graphene exhibits a unique version of the integer quantum Hall effect (IQHE) that could be used as a new, more accurate, resistance standard [23]. The combination of high mechanical strength and impermeability suggests that graphene can be used as a gas barrier or as the suspended membrane in nanoelectromechanical systems (NEMS). Composite materials is another field where the mechanical strength of graphene can help improve performance while adding functionality by making the material both highly stretchable and electrically- and thermally conducting [24]. Probably the most promising electronic application in short term is the use of graphene as a transparent and flexible electrode [25, 26]. Also, its optical and electronic properties could lead to improved photovoltaics and new kinds of sensors [27-30].

Originally, great hope was put in using graphene in high frequency transistors, both in digital logic- and analog circuits. It is foreseen that silicon-based transistors in digital logic will eventually have to be replaced to enable the continuation of performance improvements following Moore's law [31, 32]. While high frequency operation up to 300 GHz has been shown for graphene transistors [33], and predictions estimate that it could be pushed to the THz range [34], the lack of a band gap (see Chapter 2.1) makes it difficult to achieve a low leakage current in digital logics and a large power gain in analog applications [35, 36]. Several ways to open a band gap in graphene exist, but so far it has not been possible to achieve a sizeable band gap while maintaining high charge carrier mobility. It is unclear if this is a fundamental limitation and whether we will ever see a carbon-based processor.

Interestingly, not all electronics require extremely high carrier mobilities. Ink-jet printed electronics are low-cost devices for a variety of applications where modest electronic performance is acceptable. Traditionally, the charge carrier mobility for this technology is less than 1 cm^2/Vs. Using graphene-based inks, the mobility can be as high as ~95 cm^2/Vs, an improvement of two orders of magnitude. Graphene-based inks are among the first commercially available products based on graphene [37]. Graphene may also find its place within several energy applications. It can be used as an electrode in batteries [38, 39], for fuel- and other electrochemical cells [40, 41],

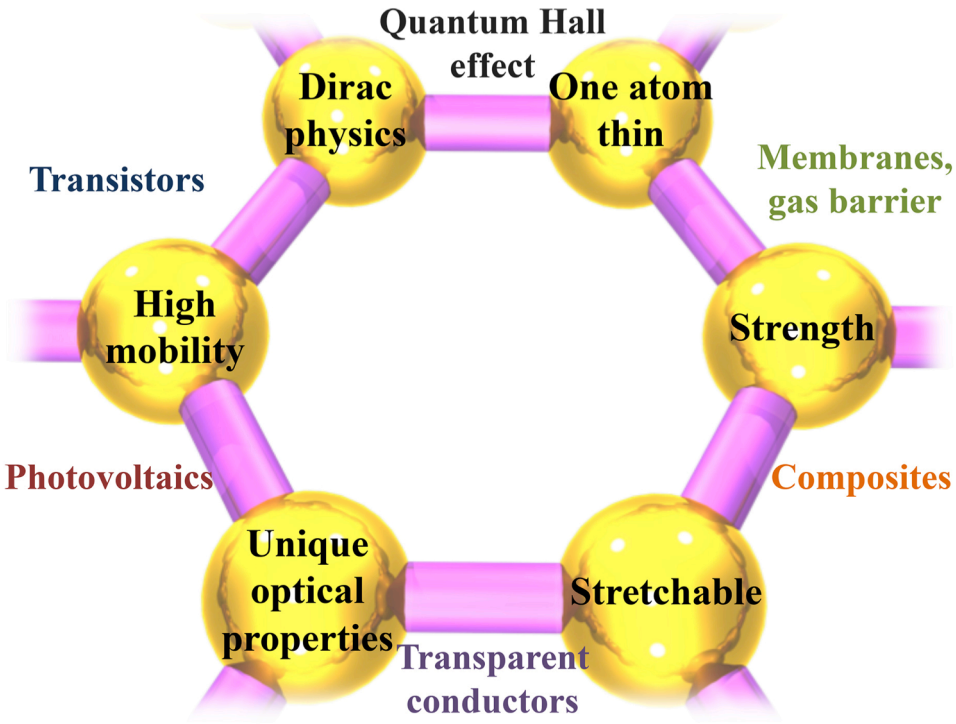

Figure 1.2: A hexagonal view of six of the most exciting properties of graphene and six promising applications. At least two of those properties are utilized in each application. Several applications incorporate more than two particular properties.

and in ultracapacitors [14].

Such a comprehensive list of potential applications has initiated a rush for immaterial property connected to graphene [42]. With fabrication methods rapidly improving, this might just be the beginning of the graphene gold rush. Three things are, however, worth noting.

First, the Kroemer's lemma states that "*the principal applications of any sufficiently new and innovative technology have always been applications that were created by that technology, rather than being pre-existing applications, where the new technology simply provided improvements.*" [43]. That is, if the technology is to succeed, it is likely to do so based on completely new applications.

Second, also in the case of CNTs a lot of hype was initiated, promising revolutionary applications [44]. More than twenty years after their discovery, almost no applications have been realized. There is, however, one distinct difference: graphene is a planar material, and planar technology is easier to use in most fabrication processes. In this case, it can be compared to diamond-like carbon, which is planar carbon (mostly sp^3-hybridized), and is used commercially in great volumes in many applications [45, 46].

Third, there exist many different types of graphene depending on the method of fabrication and how it is integrated. These different types are essentially different materials with different properties and applications. Hence, it is more correct to talk about a graphene material family, rather than the single material. They do not all share the same strengths and weaknesses, making it more likely that at least some could succeed. Graphene also opened up a new world of different 2D materials, whose possible applications so far remain unknown.

Finally, on several occasions throughout history, great technological breakthroughs have been accompanied by considerable health hazards. Since graphene is, as are many nanomaterials, a new material with hopes of use in many different applications, its potential health hazards are an important concern. While much focus is put on this issue, very little scientific work has been published and its environmental impact and potential health hazards remain largely unknown so far [47-49].

For more detailed introductions to graphene, the reviews of Geim *et al.* [50] and Novoselov *et al.* [51], as well as the technological roadmap by Ferrari *et al.* [52] are recommended.

1.2 Aim and outline

This thesis is focused around two main topics: fabrication of graphene, and combining graphene with superconductors. The former is key for the development of graphene

technology and its potential success in real life applications. The latter investigates how two different kinds of materials, with exotic properties in their own right, can be combined to look at old phenomena from a new angle.

Chapter 2 provides brief theoretical sections that will be useful when reading the later chapters of the thesis.

Chapter 3 focuses on methods used to produce and process graphene. These include: mechanical exfoliation, graphene grown catalytically on Cu (paper **I**), transfer of graphene from catalyst to target substrate (paper **II**), graphene grown non-catalytically on insulators (paper **III**), and making suspended graphene structures (paper **IV**).

In Chapter 4, electrical and optical properties of graphene produced by the different methods are assessed.

Chapter 5, presents a mechanical technique used for cleaning graphene (paper **V**).

Experiments on a graphene-based bolometer are presented in Chapter 6 (paper **VI**).

In Chapter 7, quantum transport measurements in graphene are shown. The Aharonov-Bohm effect is studied in a graphene nanostructure (paper **VII**).

Chapter 8 describes electrical measurements of graphene in small, inhomogeneous magnetic fields (paper **VIII**).

When pursuing the doctoral degree in Physics in Sweden, it is highly encouraged that the candidate writes and presents a Licentiate thesis, essentially a "half-PhD", before the full PhD thesis is presented. So has been the case also for this PhD candidate. The contents of Chapters 1, 2.1-2.5, 2.8, 3.1, 3.2, 3.4, 3.6, 4, 5, 6, and 7 have in part already been presented there. The licentiate thesis can be found in reference [53].

2 Theory

Some key theoretical concepts that are useful for understanding the properties of graphene are provided in this chapter. A brief description of the electronic structure of graphene is presented in Chapter 2.1. The electric field effect is introduced in Chapter 2.2 and it is explained how it can be used to assess certain electronic material properties. In Chapter 2.3, the Hall effect is described as yet another tool for characterizing graphene and in Chapter 2.4 the quantum Hall effect is introduced. The theory of the Aharonov-Bohm effect is presented in Chapter 2.5. In Chapter 2.6, the theory of weak localization of graphene in both homogeneous and inhomogeneous magnetic fields is presented. The concept of the bolometer, a radiation detector, is described in Chapter 2.7. How to engineer visibility of graphene on thin dielectrics is shown in Chapter 2.8. Raman spectroscopy, an optical method for material characterization, is presented in Chapter 2.9.

2.1 Electronic properties

Graphene shows remarkable electronic properties [54]. It is a zero band gap semimetal with a linear dispersion for low energy excitations. Figure 2.1 shows the dispersion relation for monolayer graphene. Close to the points where the valence- and conductance bands meet, the energy dispersion relation is linear in momentum. These, six per Brillouin zone, are denoted Dirac points. This is in contrast with free electrons and electrons in traditional semiconductor systems where the dispersion is quadratic. The dispersion relation for electrons in graphene close to the Dirac points is written as:

$$E = \hbar v_{\mathrm{F}} \sqrt{k_x^{\,2} + k_y^{\,2}}, \tag{2.1}$$

where E is the energy, $\hbar$ is the reduced Planck constant, $v_{\mathrm{F}} = 10^6$ m/s is the Fermi velocity of graphene, and $k_{x,y}$ are the x- and y-direction wave numbers, respectively. Being linear for low energies, the dispersion relation for electrons in graphene mimics that of relativistic Dirac particles with zero effective mass. The linear dispersion

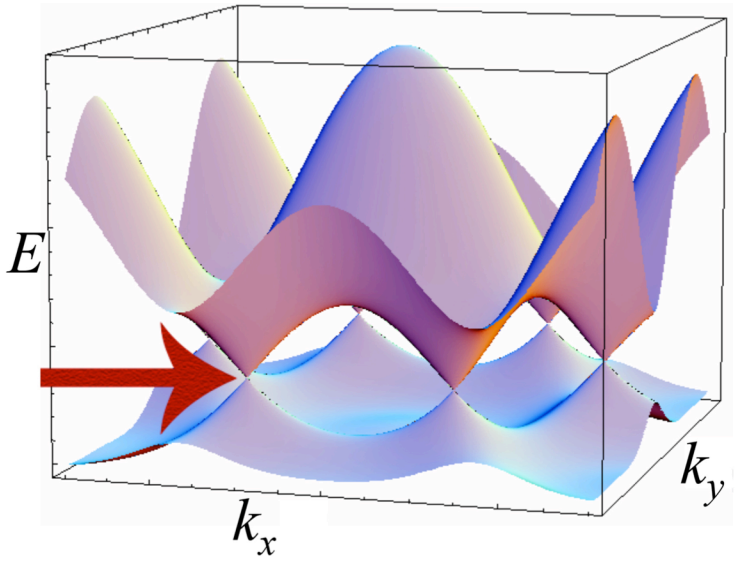

Figure 2.1: Dispersion relation for graphene. The valence- and conductance bands meet at six points in the Brillouin zone. Close to these Dirac points, the energy E is linear in momentum (k_x, k_y). The red arrow points at one of the Dirac points.

relation for graphene gives an opportunity for fundamental studies of Dirac physics [55]. The dispersion relation is also the reason for that, together with the possibility of obtaining high-quality graphene crystals, both electrons and holes can exhibit very large mobilities in graphene [18, 56, 57].

For a much more detailed review on graphene's electronic properties, please see Castro Neto *et al.* [54].

2.2 Field effect

Electronic properties of semiconductors can be externally tuned by an electric field. This property is extensively utilized in the field-effect transistor, the basic building block of modern electronics. In conventional metals, however, such an effect is not observed due to the high charge carrier density and screening of the electrical field at very short distance. For graphene, being one atom thin, capacitively induced surface charges in the order of 10^{13} cm^{-2} by a gate electrode are enough to drastically change the resistivity [2]. Depending on the sign of the applied gate voltage, the carrier concentration can be tuned from holes to electrons, manifesting the bipolar field effect. Due to thermal fluctuations, non-uniformities in graphene, electrical charges in the vicinity of graphene, impurities, etc., there is always a minimum residual charge carrier concentration n_0 in any graphene device, despite tuning by the gate. The doping mechanisms of graphene are further discussed in Chapter 5.1.

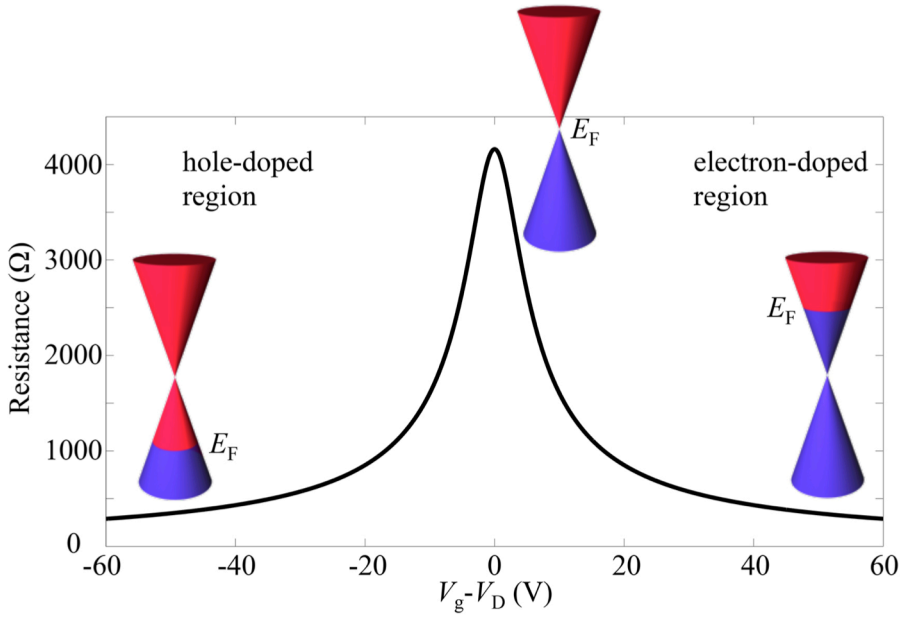

Figure 2.2: Calculated resistance as a function of gate voltage V_g for graphene on a standard 300 nm SiO_2 substrate using equation (2.2). The voltage where graphene resistance reaches its maximum is denoted the Dirac voltage V_D. The parameters used in the calculation are: $R_0 = 0\ \Omega$, $N_{sq} = 1$, $n_0 = 3.0 \cdot 10^{11}\ cm^{-2}$, and $\mu = 5000\ cm^2/Vs$. If the gate voltage is larger than V_D, the graphene is n-doped (electron doped) and if it is smaller, the graphene is p-doped (hole doped). The red and blue cones symbolize the Fermi level for different doping regimes. E_F marks the Fermi energy.

Charge carriers in graphene can have extremely large mobility μ in the order of $10^5\ cm^2/Vs$ [57] near room temperature and $10^6\ cm^2/Vs$ at cryogenic temperature [18]. Since graphene is essentially a surface with no bulk, surface contaminants easily affect its electronic properties. This leads to both μ and n_0 being highly dependent on the graphene fabrication and device processing.

Performing field-effect measurements where the carrier concentration is controlled by a gate in a transistor configuration is a common method to electrically characterize graphene (the device layout is shown in Chapter 3.6). Assuming that μ is independent of charge carrier concentration, a diffusive model of the resistance R of the device adapted from [58] can be used:

$$R = R_0 + \frac{N_{sq}}{\sqrt{n_0^2 + n_g^2}\, e\mu}, \tag{2.2}$$

where $N_{sq} = L/W$ is the geometrical number of squares of the device (length divided by width), $n_g = (V_g\text{-}V_D) \cdot C_g/e$ is the charge induced by the gate voltage V_g relative to the Dirac voltage V_D (in a parallel plate capacitor configuration with specific

capacitance C_g), and e is the elementary charge. R_0 is a constant in the model that in two-probe measurements corresponds to the contact resistance. As all resistance measurements in this work from which μ is estimated are made using a four-probe configuration, there is no contribution from the contact resistance. Hence, R_0 should be zero. However, in practice μ is not independent of carrier density and different areas of the sample have different resistance dependence on gate voltage, resulting in a non-zero R_0 even for four-probe measurements. For a fit of equation (2.2) to four-probe resistance data to be reliable, R_0 should be negligible compared to the overall resistance.

Experimental resistance as a function of gate voltage can be fitted to the above equation using R_0, n_0, V_D, and μ as fitting parameters. Figure 2.2 shows $R(V_g\text{-}V_D)$ for $R_0 = 0\ \Omega$, $N_{sq} = 1$, $n_0 = 3.0\cdot10^{11}$ cm^{-2}, and $\mu = 5000$ cm^2/Vs. The point at which the resistance reaches the maximum, the Dirac point, corresponds to the minimum carrier density. In an ideal device this corresponds to zero gate voltage. In practical devices, the Dirac point is often shifted from zero voltage due to charged impurities in the vicinity of graphene.

The Drude model of conductivity provides another way to directly obtain a rough estimate of the mobility:

$$\sigma = n_g e\mu \Rightarrow \mu = \frac{\sigma}{n_g e}, \tag{2.3}$$

where $\sigma = 1/R_s$ is the conductivity and $R_s = R/N_{sq}$ is the sheet resistance. This can be differentiated to give an estimate of the mobility $\tilde{\mu}$, assuming a parallel plate capacitor configuration, to:

$$\tilde{\mu} \approx \frac{1}{e}\frac{\partial\sigma}{\partial n_g} = \frac{1}{e}\frac{\partial\sigma}{\partial V_g}\frac{\partial V_g}{\partial n_g} = \frac{1}{e}\frac{\partial\sigma}{\partial V_g}\frac{1}{C_g} = \frac{1}{e}\frac{\partial\sigma}{\partial V_g}\frac{d}{\epsilon_r A}, \tag{2.4}$$

where d is the distance between gate electrode and graphene, ε_r is the relative permittivity, and A is the overlapping area of gate electrode and graphene. This model is useful when the electronic quality of graphene is poor. In this case, resistance is typically not a symmetric function of gate voltage and equation (2.2) does not provide a good description.

2.3 Hall effect

The magnetic field is a powerful tool for characterizing the electronic properties of a material. When a magnetic field is applied perpendicularly to a current flowing in the

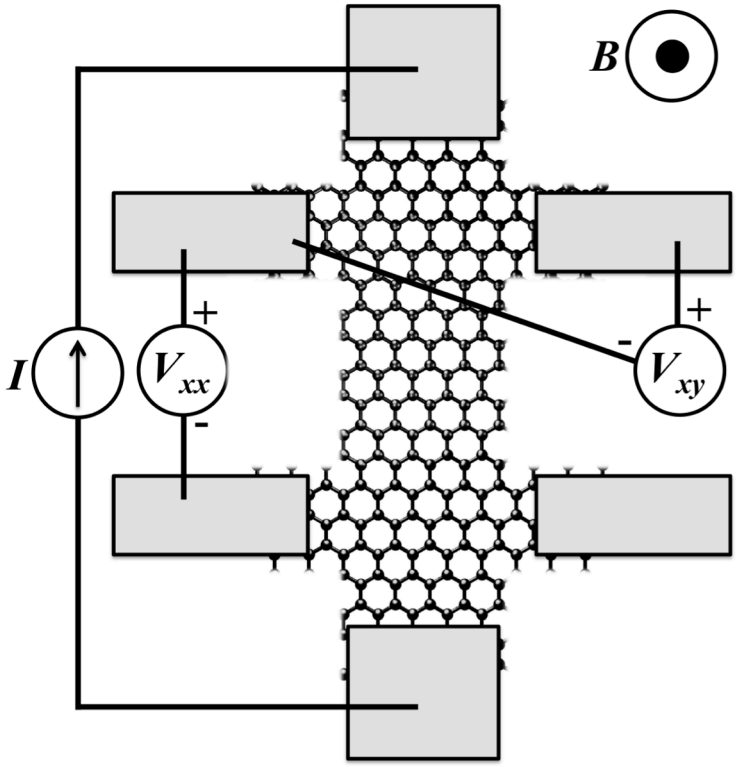

Figure 2.3: An illustration of a graphene Hall bar structure. A current I is applied and the longitudinal- and transverse (Hall) voltages V_{xx} and V_{xy} are measured in a four-probe configuration. The magnetic field B is applied out of plane, perpendicularly to the current path.

conductor, charge carrier trajectories "bend" due the laterally oriented Lorentz force. This leads to a change in the resistance along the net current path (magnetoresistance) and a voltage buildup in the transverse direction (Hall voltage). Hall measurements provide a direct way to measure the charge carrier concentration in any conductor. Knowing the carrier concentration, the mobility can be calculated from the conductivity at zero magnetic field. Well-defined sample geometry is needed for accurate measurements.

Figure 2.3 shows the Hall effect measurement setup. A current I is applied through a graphene strip while voltages along (V_{xx}) and transverse (V_{xy}) the current path are measured. The longitudinal resistivity is calculated as:

$$\rho_{xx} = \frac{R_{xx}}{N_{\mathrm{sq}}} = \frac{1}{N_{\mathrm{sq}}}\frac{V_{xx}}{I}, \tag{2.5}$$

where R_{xx} is the longitudinal resistance. The Hall resistivity is given by:

$$\rho_{xy} = R_{xy} = \frac{V_{xy}}{I}, \tag{2.6}$$

where R_{xy} is the transversal resistance (which is equal to the Hall resistivity, since no net current flows in that direction). The theoretical expression for the Hall voltage is derived from the Lorentz force:

$$V_{xy} = -\frac{IB}{nq}, \tag{2.7}$$

where B is the applied magnetic field, n is the charge carrier number density, and q is the carrier charge, which can be either $-e$ or $+e$ for electrons and holes, respectively. These expressions are combined to obtain:

$$\rho_{xy} = -\frac{1}{nq}B = -R_{\mathrm{H}}B, \tag{2.8}$$

where R_{H} is the Hall coefficient. R_{H} is obtained by a linear fit at low magnetic fields, typically less than one tesla. According to the above conventions, positive (negative) ρ_{xy} corresponds to n-type (p-type) doping, respectively. Via the Drude model in equation (2.3) we obtain an expression for the mobility, using the conductivity at zero magnetic field:

$$\mu = \frac{\sigma}{|q|n} = \frac{\sigma}{e}\left|\frac{V_{xy}}{IB}\right| e = \left|R_{\mathrm{H}}\right|\sigma. \tag{2.9}$$

Hence it is possible to obtain the mobility independently from the field-effect measurements.

2.4 Quantum Hall effect

Several interesting phenomena in 2D systems occur at high magnetic fields [59]. One example is that at sufficiently high fields and low temperature, the longitudinal resistance vanishes and the Hall resistivity becomes quantized at discrete levels [60]. These Hall plateaus occur at integer values of the conductance quantum e^2/h. This is the IQHE. It is a robust effect that can be visible also in rather dirty samples with significant degree of disorder. Since the Hall plateaus are given by the fundamental constants, the IQHE can be used as a resistance standard.

When a high magnetic field is applied to a 2D system, the continuous density of states (DOS) is split into discrete Landau levels. Ideally, this splitting of energy levels results in δ-peaks in the DOS, but due to scattering and thermal broadening, the peaks have a finite width. The energy spacing between those levels can be larger than the thermal energy at sufficiently low temperature. When the magnetic field is increased, the spacing changes and the peaks in the DOS change their position relative to the Fermi level. This leads to oscillations of many of the system properties. Resistivity

oscillations are called Shubnikov-de Haas oscillations. In the case of graphene, it is also possible to fix the magnetic field and instead vary the Fermi energy using a gate electrode.

One way to describe the IQHE is to consider two types of electronic states when the Fermi level lies between two Landau levels. First, there are localized states in the interior that undergo cyclotron motion that do not carry current. Second, there are extended states along the sample edges representing two separated edge channels that carry current in opposite directions. These lead to suppressed backscattering and vanishing longitudinal resistivity ρ_{xx}. The Hall resistivity ρ_{xy} is finite and quantized in this case. In graphene, quantized ρ_{xy} plateaus are given by [8, 23]:

$$\rho_{xy} = \frac{1}{g_s\left(l+1/2\right)}\frac{h}{e^2},\ l = 0,1,2,..., \tag{2.10}$$

where h is the Planck constant, and $g_s = 4$ is the degeneracy factor, including spin and valley degeneracies. This gives the following sequence:

$$\rho_{xy} = 12.9,\ 4.30,\ 2.58\ \text{k}\Omega,\ \ldots\ , \tag{2.11}$$

which is different from the ordinary IQHE (12.9, 6.45, 4.30 kΩ, ..., if the system has degeneracy $g_s = 2$) and the effect is named half-integer quantum Hall effect. The different sequence comes from the unique band structure of graphene. Since this Hall plateau series is unique to Dirac materials with four-fold degeneracy, it can be taken as a signature of monolayer graphene. Bilayer graphene also shows an unusual, but different from that of monolayer graphene, series of plateaus (6.45, 3.23, 2.15 kΩ, ...,) [61].

2.5 Aharonov-Bohm effect

When charge carriers travel along different trajectories in a conductor, they interfere due to their quantum mechanical nature. Applying magnetic fields modifies this interference, giving a characteristic $R(B)$ dependence [62]. This dependence is irregular but reproducible, reflecting a characteristic distribution of scattering centers in a sample. Such irregular $R(B)$ is called universal conductance fluctuations (UCFs). Importantly, this is not noise. UCFs are typically seen only at low temperature. Because of the large amount of different electron paths, the interference is complex and no periodicity is seen.

Better-defined electron paths can be engineered by shaping the sample into a ring. Periodic interference from electron paths that encircle the ring occurs similar to the optical double-slit experiment. By applying a uniform, perpendicular magnetic

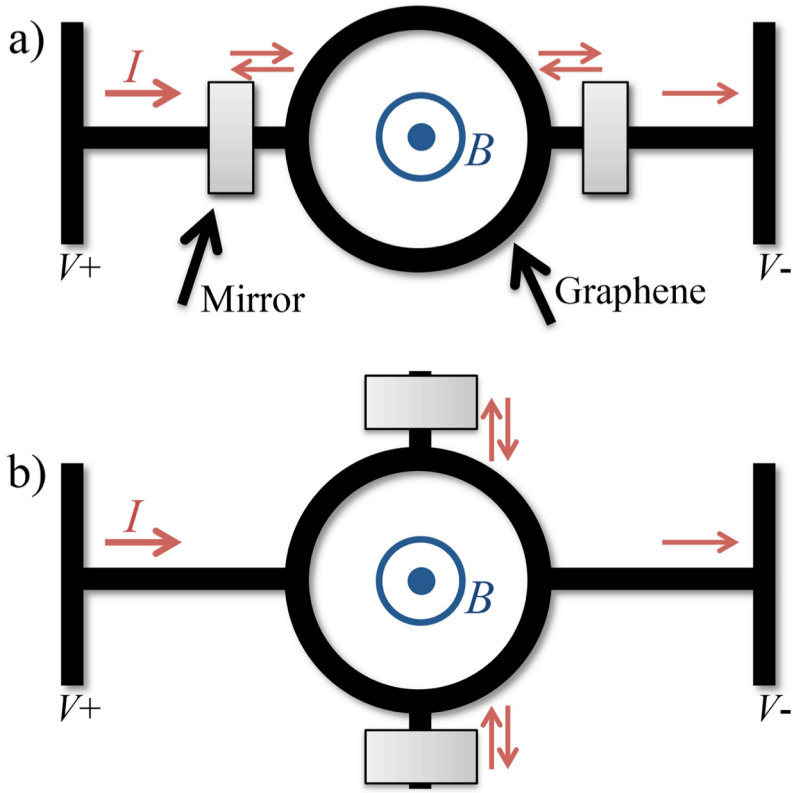

Figure 2.4: (a) An illustration of an Aharonov-Bohm device. A current I is applied through a ring structure in a perpendicular magnetic field B while monitoring the resistance. Metal mirrors are deposited on the ring perimeter along the current path (L-mirrors) to confine charge carriers to the ring. The red arrows indicate the current path and the reflections at the mirrors. (b) Similar device layout, but with mirrors placed perpendicularly to the current path (T-mirrors).

field, $\boldsymbol{B}$ with magnetic vector potential $\boldsymbol{A}$, a phase shift $\delta\varphi$ between electron paths travelling on different sides of the ring is induced [63]:

$$\delta\varphi = \frac{e}{\hbar}\int_{\text{loop}} \mathbf{A}\cdot d\mathbf{l} = \frac{e}{\hbar}\int_{\text{area}} \nabla\times\mathbf{A}\, d\mathbf{a} = \frac{e}{\hbar}\int_{\text{area}} \mathbf{B}\cdot d\mathbf{a} = \frac{e}{\hbar}aB, \tag{2.12}$$

where a is the area of the loop and B is the magnitude of the magnetic field. Thus, the fundamental oscillation frequency is $e/h{\cdot}a$. If the coherence of the system is large enough, higher order oscillations, $N{\cdot}e/h{\cdot}a$, where N is an integer, also become visible. These correspond to charge carriers coherently making more than one half-revolution around the ring.

To improve the quantum coherence of the system, "mirrors" are put in the vicinity of the graphene ring. Figure 2.4 shows the experiment layout. Previously, superconducting Al mirrors were put on Ag rings and the improved coherence was attributed to the superconducting nature of the mirrors and a phase memory effect was

observed [64]. But also with normal metal mirrors an improved visibility of Aharonov-Bohm oscillations can be seen [62, 65].

In this work, samples with both superconducting Al mirrors and normal metal Au mirrors were produced to distinguish the effect of superconductivity. Whether superconducting or not, the mirrors serve the purpose of confining charge carriers to the ring by increasing scattering at its entry and exit points because of a Fermi velocity mismatch between the graphene and the deposited metal. In principle any material that increases the scattering of charge carriers traveling through the ring could improve the visibility of Aharonov-Bohm oscillations. Three types of mirror geometries were tried: mirrors at the current leads (L-mirrors), mirrors placed perpendicularly to the current path (T-mirrors), and samples with no mirrors.

Strong UCFs can mask the Aharonov-Bohm oscillations. In order to distinguish between aperiodic UCFs and the periodic oscillations originating from the Aharonov-Bohm effect, fast Fourier transform (FFT) analysis is utilized.

2.6 Weak localization

Weak localization (WL) is a quantum mechanical correction to the low-field magnetoresistance of a 2D system. It has been studied for ordinary 2DEGs [66, 67], and is observed also in graphene [68, 69]. For high-quality samples made by mechanical exfoliation it can however be difficult to measure [70]. WL is seen as a dip in conductivity (peak in resistivity) at zero magnetic field. It can be explained by considering closed electron propagation trajectories in graphene. For each such trajectory one can also consider its self-crossing counter-part related by the time-reversal symmetry. The interference between such paths leads to enhanced backscattering and, consequently, resistance. If the symmetry is broken, by for example applying a magnetic field, the enhanced backscattering vanishes. This leads to the peak in resistivity at zero magnetic field.

For graphene, the WL correction to the conductivity can be described by [71, 72]:

$$\sigma(B) = \sigma(0) + \Delta\sigma(B) = \sigma(0) + \frac{e^2}{\pi h}\left(F\left(\frac{B}{B_\varphi}\right) - F\left(\frac{B}{B_\varphi + 2B_i}\right) - 2F\left(\frac{B}{B_\varphi + B_*}\right)\right), \tag{2.13}$$

where $F(z) = \ln(z) + \psi(0.5+z^{-1})$, and ψ is the digamma function. $B_{\varphi,i,*} = h/(8\pi e L_{\varphi,i,*}^2)$ are the characteristic fields from which $L_{\varphi,i,*}$, the characteristic lengths, can be derived. L_φ is the phase coherence length corresponding to inelastic scattering and $L_{i,*}$ are the elastic scattering lengths.

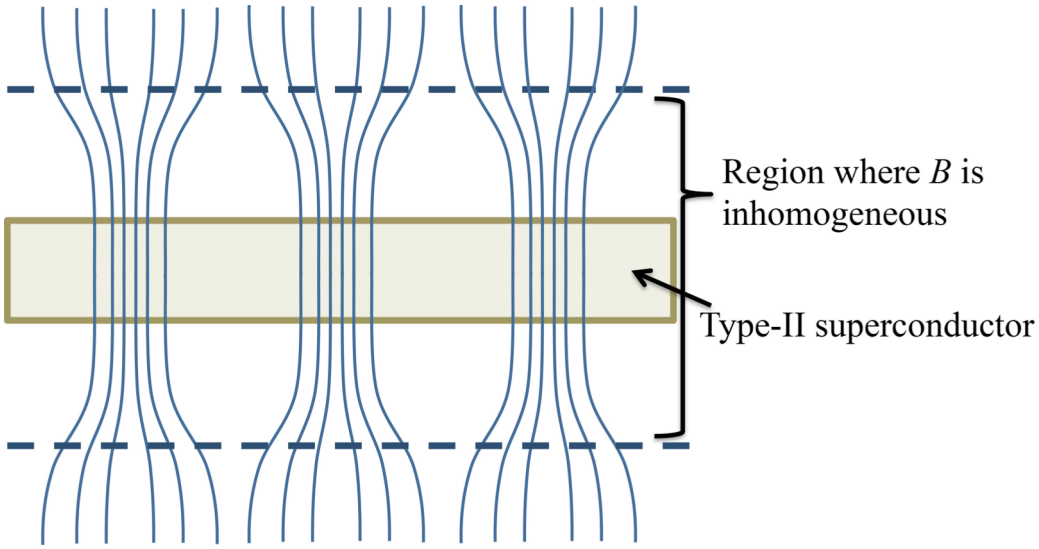

Figure 2.5: Side view of vortices in a type-II superconductor thin film. The magnetic field, perpendicular to the thin film, penetrates at discrete locations when the magnetic field exceeds the lower critical field, H_{c1}. In an ideal case, it would form a triangular lattice. In the case of a deposited thin film, however, flux will be pinned to defects and form a less periodic structure.

The previous discussion regards WL in homogeneous magnetic fields. When instead an inhomogeneous magnetic field is applied, a different WL correction is obtained if L_φ exceeds the length scale over which the magnetic field is uniform [73]. For several non-uniform field geometries, measurable corrections to the macroscopic magnetoresistance are theoretically excepted [73] and experimentally studied in 2DEGs [74-77].

Only a few studies have been conducted on graphene WL in inhomogeneous magnetic fields [78-80]. For conventional two-dimensional electron gases (2DEGs) WL was studied for the case of cylindrical flux tubes with radius r_0 smaller than L_φ. In that case of inhomogeneous magnetic fields, the conductivity correction can be written [73]:

$$\Delta\sigma = \frac{e^2}{\pi h}\frac{1}{\ln(b_0 / B_\varphi)}\left(\frac{|B|}{B_\varphi}\right), \tag{2.14}$$

where b_0 is the magnitude of the magnetic field inside the tubes. This expression holds for B smaller than the characteristic magnetic field B_φ, where the normal homogeneous WL result is recovered.

A straightforward way to create such an inhomogeneous magnetic field is to place a type-II superconductor in close proximity to, but electrically separated from, the material studied. When the magnetic field penetrates the superconductor, it does so in the form of flux tubes with a single flux quanta, so called Abrikosov vortices [81]. The material in study, in this case graphene, placed close by will experience the

inhomogeneous magnetic field. Figure 2.5 shows a graphical representation of such arrangement.

2.7 Bolometer

A bolometer is an electromagnetic radiation sensor, which uses the temperature-dependent electrical resistance of an absorber for detection. In this work a specific type of bolometer, the cold-electron bolometer (CEB), is considered. The CEB is a sensitive superconductor-based detector consisting of a normal metal absorber connected to two superconducting leads through tunnel barriers, the double-barrier superconductor-insulator-normal metal-insulator-superconductor (SINIS) device structure. A common device layout would consist of two superconducting Al electrodes connected to the normal metal absorber through Al_2O_3 tunnel contacts. The absorber can be made from a non-superconducting metal, for example Cu, or from Al deposited on chromium oxide that suppresses the superconductivity in Al.

The CEB acts as a sensitive thermometer. It detects the temperature changes in the absorber metal upon exposure of (typically) GHz or THz radiation. Hence it can be used both as a pure thermometer and as a radiation sensor. The sensitivity of such a device depends, in part, on the volume of the metal absorber. Graphene, being ultimately thin, is thus an interesting candidate to be used as absorber material.

Chapter 6 demonstrates the use of graphene as CEB detector material. It is however, just a first demonstration and it is neither optimized, nor is its noise performance characterized. Hence the detailed theoretical description of the CEB is omitted in this work and the reader is instead recommended the work of Kuzmin [82], Lee *et al.* [83], and Richards [84].

2.8 Optical visibility

Graphene is almost fully transparent, absorbing only 2.3 % of visible light [20]. While this is a large number for an atomically thin material, it makes graphene very difficult to see when deposited on common substrates. It was essential for the isolation of graphene that the researchers happened to use silicon wafers with a thin layer of silicon dioxide, which had just about the right thickness for enhancing the visibility of graphene. While it first happened by a fortunate coincidence, it is possible to engineer the sample layout to maximize the graphene visibility. Identifying graphene and determining the number of layers from the contrast in optical microscopy is a quick and powerful method.

The contrast of graphene deposited on opaque substrates with a thin transparent film on top (typically an oxide) can be calculated using a simple optical model [85]. Interference between incident and reflected light beams in the substrate-oxide-

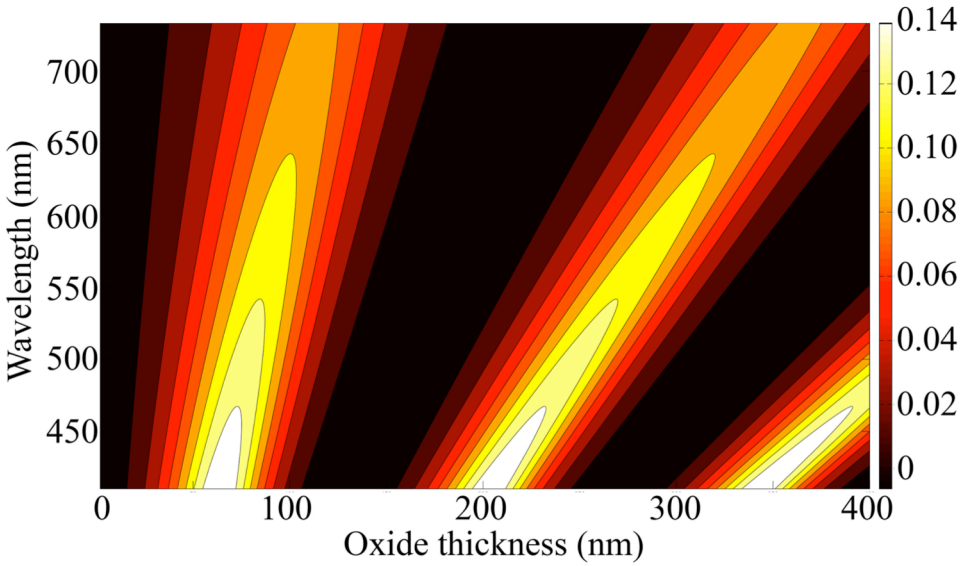

Figure 2.6: Contour plot of the calculated optical contrast of graphene on SiO_2/Si substrates as a function of wavelength and oxide thickness. The color scale shows the theoretical contrast, which reaches ~0.14 as highest.

graphene structure gives rise to a contrast between graphene and the bare substrate, depending on wavelength λ and the oxide thickness d. The same effect gives oxides like SiO_2 their familiar colors on top of silicon. SiO_2 on Si substrates is the most common setup used for graphene experiments.

An opaque substrate with refractive index $\tilde{n}_3$ is covered with an oxide layer with refractive index $\tilde{n}_2$ and thickness d_2. Graphene is assumed to have the same refractive index as graphite $\tilde{n}_1 = 2.6 - 1.3\cdot i$ and a thickness of $d_1 = 0.34$ nm (the distance between graphene layers in graphite). The refractive index of air is $\tilde{n}_0 = 1.0$. The relative indices of refraction are denoted as:

$$r_1 = \frac{\tilde{n}_0 - \tilde{n}_1}{\tilde{n}_0 + \tilde{n}_1},\ r_2 = \frac{\tilde{n}_1 - \tilde{n}_2}{\tilde{n}_1 + \tilde{n}_2},\ r_3 = \frac{\tilde{n}_2 - \tilde{n}_3}{\tilde{n}_2 + \tilde{n}_3}, \tag{2.15}$$

and the phase shifts due to the optical path as:

$$\Phi_1 = 2\pi\tilde{n}_1 d_1 / \lambda,\ \Phi_2 = 2\pi\tilde{n}_2 d_2 / \lambda. \tag{2.16}$$

The reflected light intensity $\tilde{I}_{\mathrm{op}}$ can be calculated as:

$$\tilde{I}_{\mathrm{op}}(\tilde{n}_1) = \left| \frac{\left(r_1 e^{i(\Phi_1+\Phi_2)} + r_2 e^{-i(\Phi_1-\Phi_2)} + r_3 e^{-i(\Phi_1+\Phi_2)} + r_1 r_2 r_3 e^{i(\Phi_1-\Phi_2)} \right)}{\left(e^{i(\Phi_1+\Phi_2)} + r_1 r_2 e^{-i(\Phi_1-\Phi_2)} + r_1 r_3 e^{-i(\Phi_1+\Phi_2)} + r_2 r_3 e^{i(\Phi_1-\Phi_2)} \right)} \right|^2 . \tag{2.17}$$

The contrast is defined as the relative difference in reflected light of areas with and without graphene, respectively. The intensity from areas without graphene are calculated using the refractive index of air $\tilde{n}_1 = 1.0$:

$$\text{contrast} = \frac{\tilde{I}_{\text{op}}\left(\tilde{n}_1 = 1.0\right) - \tilde{I}_{\text{op}}\left(\tilde{n}_1 = 2.6 - 1.3 \cdot i\right)}{\tilde{I}_{\text{op}}\left(\tilde{n}_1 = 1.0\right)}. \tag{2.18}$$

By varying both the wavelength of light and the thickness of the oxide, the contrast of graphene can be optimized. The result for graphene on top of SiO_2 is shown in Figure 2.6. The best contrast (for green light) is achieved for either ~90 nm or ~290 nm of SiO_2 thickness. Using green light of ~550 nm wavelength, a contrast around 10 % can be achieved. This is more than twice than what is expected from the pure absorption of graphene.

While optical microscopy provides a fast technique to identify graphene, it has to be calibrated against other methods, which provide a direct signature of having a certain number of layers. In this work this is done using quantum Hall effect measurements as described in Chapter 2.4, as well as using Raman spectroscopy that is described next in Chapter 2.9. This allows us to distinguish between one-, two-, and multilayer graphene.

2.9 Raman spectroscopy

Raman spectroscopy is an optical spectroscopic method used to study various types of materials. A laser spot is focused with beam diameter ~1 μm on a sample and the inelastically (Raman) scattered photons are collected in a detector. The laser beam can be scanned over the sample, generating a 2D map. Raman scattered photons are generated through inelastic interaction between the incoming photon and phonons in the material and, hence, carry information about the phonon spectrum of the material. The distribution of the inelastic scattered light is a direct probe of the low-frequency phonon modes of the system. In contrast, the dominant elastically (Rayleigh) scattered photons provide no such information about the material, and are filtered out.

Various types of carbon materials have been studied using Raman spectroscopy [86] and it can be considered a standard tool for analyzing graphene samples [87-89]. For the case of graphene, the number of atomic layers and the amount of disorder are typical examples of information that can be obtained using this technology.

Typical Raman spectra obtained for exfoliated graphene and graphene grown on Cu by CVD are shown in Figure 2.7. The three main features are the G peak (~1580 cm^{-1}), the 2D (or G') peak (~2700 cm^{-1}), and the D peak (~1350 cm^{-1}). While the Raman spectrum of graphene can be significantly richer, much information can be obtained from just these three features alone. The G peak originates from the stretching of the carbon-carbon bond in sp^2 materials. It is sensitive to the hexagonal symmetry of the lattice and is thus sensitive to material strain. The 2D peak is also a signature of sp^2 carbons, originating from a second-order two-phonon process. For single-layer graphene the 2D peak is symmetric, typically with a full width at half maximum (FWHM) of ~30 cm^{-1} and an intensity I_{2D} significantly greater than that of the G peak, I_G. For bilayer- and trilayer graphene it is not symmetric and also wider, making analysis of the 2D peak the most straightforward method for determining the number of layers of a graphene sample using Raman spectroscopy. The 2D peak is dispersive, and both its position and amplitude relative to the G peak depend on the laser excitation energy. Finally, the D peak arises from disorder in the lattice. The ratio between D- and G peak intensities I_D/I_G is a powerful tool for quantifying the defect density in graphene [90, 91]. A defect-free graphene flake would only show a

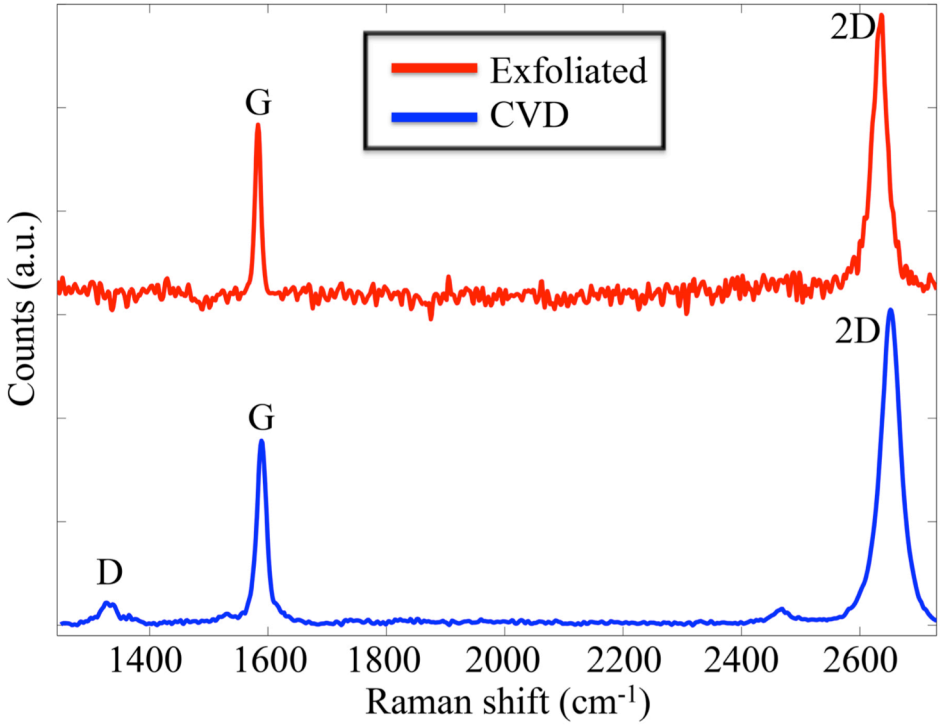

Figure 2.7: Typical Raman spectra for exfoliated graphene (top spectrum) and graphene grown on Cu by CVD (bottom spectrum). The three most important peaks, the D-, G-, and 2D peaks, are indicated in the plot. The lack of a D peak suggests a low defect density in the exfoliated graphene sample.

D peak when the laser spot is positioned at its edge. It can be seen in Figure 2.7 that the D peak is missing for the exfoliated sample, indicating a low amount of disorder.

3 Graphene fabrication

There exist a range of techniques for fabricating graphene, all with their own strengths and limitations. Different techniques give materials with widespread properties.

The original and still very common fabrication method is mechanical exfoliation, which is described in Chapter 3.1. While it is versatile and gives the highest quality graphene to date, the technique is not scalable and can only be used for research and development. The seemingly most promising scalable method is producing graphene by CVD on metal catalysts. CVD of graphene on copper, the most common catalyst, is described in Chapter 3.2 (paper **I**). It also describes an etching method used during transfer of graphene to a desired target substrate. In Chapter 3.3, an alternative transfer method, in which the metal catalyst is not consumed, is described (paper **II**).

While it is possible to obtain large-area high-quality graphene using this technique, the transfer of graphene from metal catalyst to the target substrate introduces problems. For this reason a catalyst- and transfer-free graphene CVD technique is developed, which is described in Chapter 3.4 (paper **III**).

In Chapter 3.5, a technique to produce suspended graphene structures without the need for any transfer is presented (paper **IV**).

Other techniques used to produce large-area graphene include the sublimation of Si from SiC [92], liquid phase exfoliation of graphite [93], reducing graphene oxide [94], and the chemical bottom-up approach [95]. These are, however, beyond the scope of this thesis.

The most commonly used nanofabrication procedures and the typical sample layout are presented in Chapter 3.6.

3.1 Mechanical exfoliation

Geim and Novoselov originally produced graphene by exfoliating graphite with sticky tape and depositing it on a substrate [1]. A large variety of graphite sources can be

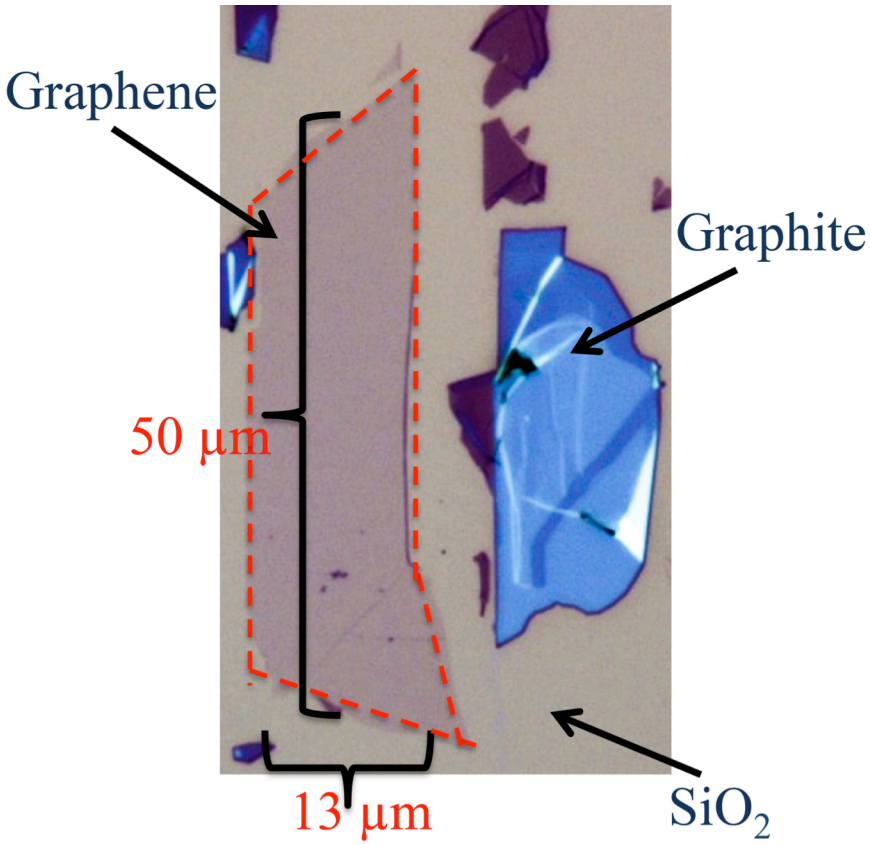

Figure 3.1: An optical image of a monolayer graphene flake on SiO_2 (outlined in dotted red) produced by mechanical exfoliation. Despite being atomically thin it is visible in the microscope. Thicker pieces of graphite with varying thickness are seen around it.

used. The exfoliated graphene samples described in this thesis were produced from large crystals of high-purity natural graphite. Such crystals typically give large flakes with little contamination. While many graphite crystals can produce large graphene flakes, few give graphene with as little contamination. To produce graphene, the graphite crystal is cleaved several times using a sticky tape. Large, uniform areas of thin graphite flakes on the tape are chosen by optical inspection and are then pressed firmly against the desired substrate. Finally, the tape is carefully removed. More details regarding the exfoliation procedure can be found in Appendix A.

Sadly, the mechanical exfoliation procedure is not selective. Instead it produces a myriad of graphite flakes with varying thickness and lateral dimensions. Only a small minority of those flakes is monolayer. Despite that, at least one or a few graphene flakes are found in most cases. Figure 3.1 shows an optical image of a ~50 µm long monolayer graphene flake put on top of a SiO_2 (300 nm)/Si substrate. Thicker pieces of graphite in the order of tens of layers are also seen. If the optical microscope is calibrated using flakes with known thickness, monolayer flakes can be identified directly from their optical contrast.

Attempts have been made to increase the throughput of mechanical exfoliation [96]. Despite that the size of flakes and the production throughput are limited, mechanical exfoliation remains the dominant technique for scientific purposes and for making proof-of-principle devices. Also, it produces the highest quality graphene with single crystals exceeding 100 μm.

3.2 Chemical vapor deposition on copper

Catalytic CVD of hydrocarbons on metallic substrates is the most promising technology for scalable production of high-quality graphene. The size of graphene is essentially limited by the size of the growth furnace and the size of the metal catalyst. 30-inch graphene fabrication capabilities have already been realized on the most common catalyst, Cu [25]. Normally such graphene films are polycrystalline with grain sizes in the order of a few μm. Under optimized conditions, however, the quality of CVD graphene can be very high, with single crystal sizes in the order of centimeters [97] and carrier mobility exceeding 10^4 cm^2/Vs [98].

CVD works by exposing a substrate to one or more precursor gases containing reactive elements. These elements are made to react by heating the chamber to high temperature (thermal CVD). In graphene CVD, typically three gases are introduced into the reaction chamber. The primary atmosphere consists of inert Ar mixed with a small amount of H_2. The growth is initiated by introducing a carbon-containing gas that provides the material needed for the film growth during the deposition phase. Ar serves as a carrier gas to help control the partial pressures of hydrogen and the carbon-containing gas. While the exact role of hydrogen in graphene CVD is not perfectly understood, it was suggested in reference [99] that H_2 serves at least three purposes. First, it helps the formation of sp^2 bonds. Second, it etches the weaker carbon-carbon bonds, assisting the formation of high-quality bonds. Finally, it reduces any oxide that may remain on the metal catalyst.

The carbon-containing gas is almost completely decomposed at the high temperature used in graphene CVD (>1000 °C) [100]. Free carbon atoms attach to- and diffuse at the surface and form chemical bonds to each other. The sp^2 bonds are the most stable and thermodynamically favorable for carbon but the temperature, while high, is still too low for the efficient creation of a large-scale sp^2-hybridized carbon lattice. However, with the use of a metal catalyst as substrate, the energy barrier for creating such bonds is lowered and the film grows efficiently. The metal catalyst is thus essential for forming high-quality bonds between the carbon atoms. As in many thin film deposition techniques, a high temperature and a low deposition rate favor high-quality crystal growth. Therefore, the deposition temperature is kept close

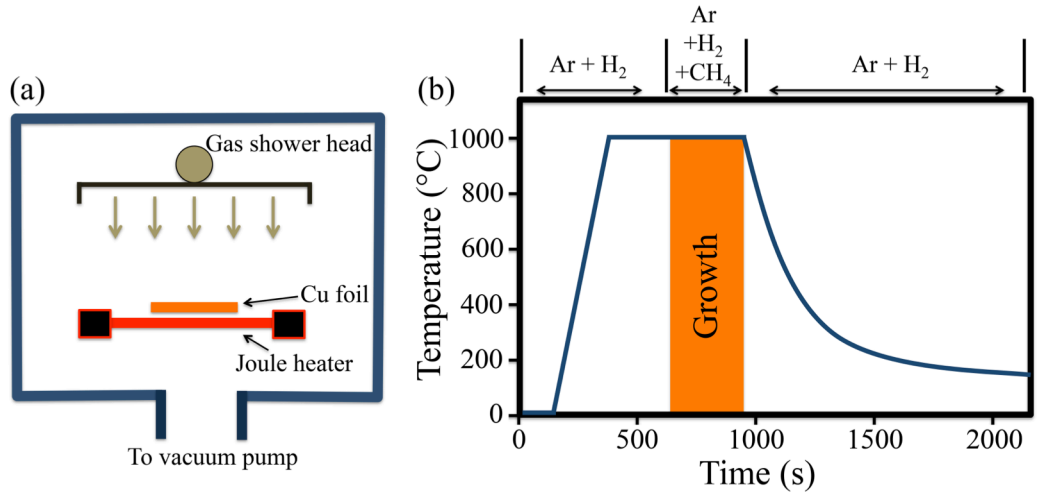

Figure 3.2: (a) A schematic overview of the cold-wall low-pressure CVD chamber. The gases are pre-mixed in the shower head and evenly introduced across the copper foil. The copper foil sits just above a graphite Joule heater (to avoid current flowing through Cu). A thermocouple connected directly to the heater measures the temperature. (b) Temperature profile of a typical graphene deposition cycle on copper. The system is stabilized at high temperature for 5 min prior to growth. Rapid ramping of temperature is used for both heating and cooling. Adapted from paper **I**.

to the melting point of copper and the partial pressure of the carbon-containing gas is kept low.

Graphene was early grown on nickel substrates [101, 102], possibly inspired by the CVD fabrication procedure for CNTs [103]. At high temperature, hydrocarbons decompose and carbon dissolves in the Ni substrate. Carbon segregates at the surface upon cool down thereby forming graphene. This results in a film with a varying number of graphene layers. Achieving a predominantly monolayer film is challenging. Also, it is very sensitive to catalyst preparation and process timing.

In contrast, due to the negligible carbon solubility, the growth process of graphene on copper is dominated by surface chemical reactions [9, 25, 104]. The copper surface catalyzes both the decomposition of carbon precursor and the graphene formation. After the growth of one graphene layer, the surface-catalyzed reactions are screened off by graphene, suppressing further growth. This results in large-area coverage of predominately monolayer graphene, with a few percent coverage of bi- and multilayers [105, 106]. Since the process is largely self-limiting it is less sensitive to the process parameters. The highest quality CVD-grown graphene is produced on copper catalysts [98].

In this work, high-quality graphene is grown on Cu foils. It is also possible to use evaporated Cu thin films as catalysts but they produce graphene of worse quality and are beyond the scope of this thesis [107-109]. An overview of the CVD chamber and a temperature profile for a typical growth process is shown in Figure 3.2(a) and

(b), respectively. The high purity Cu foil (50 μm thick, 99.995 % or 99.9999 % purity) is cleaned using acetone and isopropanol to remove organic contaminants and treated using acetic acid to remove the native copper oxide, prior to growth. The Cu foil is loaded into a cold-wall low-pressure CVD system equipped with a graphite Joule heater. The temperature is measured by a thermocouple in contact with the heater. Gases are premixed in a quartz shower head to produce a uniform vertical gas flow.

The system is first evacuated to <0.1 mbar. Then, gases are let in to reach the working pressure of 6.4 mbar. Heating is performed in a flow of 20 sccm H_2 and 1000 sccm Ar. The temperature is ramped to 1000 °C at a rate of 300 °C/min. The catalyst is preannealed for 5 min to increase the domain sizes in Cu and to stabilize the system parameters. The growth is conducted using CH_4 (methane) as carbon precursor gas at a flow of 30 sccm for 5 min. CH_4 is preferred because it has high decomposition temperature and only one C atom per molecule [110]. The CH_4 is pre-diluted in Ar with 5 % of CH_4 (99.9995 % pure). Hence, the partial pressure of carbon precursor gas is only $9 \cdot 10^{-3}$ mbar at a total pressure of 6.4 mbar, which was significantly lower than what was previously reported for graphene growth on Cu [111, 112]. The motivation is to achieve a lower deposition rate, a decreased density of nuclei, and to suppress the formation of multilayer graphene. It has been suggested that such conditions are too extreme [113]. However, assuming complete decomposition of CH_4 and 100 % sticking of carbon atoms to the Cu, there is enough carbon to grow more than 150 layers/s. While these assumptions are not always valid, it suggests that the partial pressure of carbon is indeed high enough to grow a continuous graphene layer.

For graphene to be characterized and used for electronic devices, it is necessary to transfer it from copper to a dielectric substrate. Transferring large-area graphene while maintaining high uniformity and good electrical properties is a non-trivial task. Wet transfer methods are the most common while dry transfer in principle is also possible [114]. A thin layer of MMA(8.5)MAA (EL10) copolymer is spin-coated on the top side of the Cu foil after growth and heated to 160 °C for 5 min to remove solvents. The copolymer acts as a mechanical support for graphene after the copper is removed. It is possible to transfer graphene without a polymer support, relying instead on the surface tension to stabilize the graphene, but it makes cleaning more difficult and the process is less reproducible. Graphene grows on both sides of the foil since the gases can penetrate the gap between the foil and the heater, but the quality of the bottom-side graphene is not very reproducible. The polymer protects the top graphene layer while oxygen plasma etching is used to remove graphene from the bottom side

of the Cu foil. If the bottom-side graphene is not removed, it can obstruct the transfer process.

There exist many different chemicals that can be used to etch copper. The etching time strongly depends on the choice of etching agent and its concentration. Some strong acids like HNO_3 quickly remove Cu, but can damage the copolymer and induce unintentional doping in graphene if not sufficiently diluted. $FeCl_3$ and other ionic salts can also be used avoiding acids completely. $FeCl_3$ gives quite reproducible results but is inefficient in removing common copper contaminants, like iron, and may result in residues after transfer. Another possibility is to use HCl, adding a very small amount of oxidizing hydrogen peroxide (H_2O_2). While HCl cannot etch copper, the small amount of H_2O_2 promotes slow oxidation of Cu. HCl then removes the copper oxide. For CVD graphene transferred using etching in this thesis, either diluted HNO_3 or diluted HCl with a small amount of added H_2O_2 are used.

When the Cu etching is complete, the etchant is gradually exchanged for water. This is achieved by removing most of the etchant-water solution and refilling with clean water several times, to remove as much of the etching residues as possible. At this point the graphene is attached to the copolymer support and is in water. The desired target substrate is submerged into the water and the graphene/copolymer sandwich is placed on top. A piece of tape is attached to the copolymer prior to etching to facilitate handling in liquid. Water is slowly removed from the beaker, leaving the graphene/copolymer lying on the target substrate. It is left drying in air for half an hour and then heated to 160 °C for 5 min to improve adhesion. Finally, the

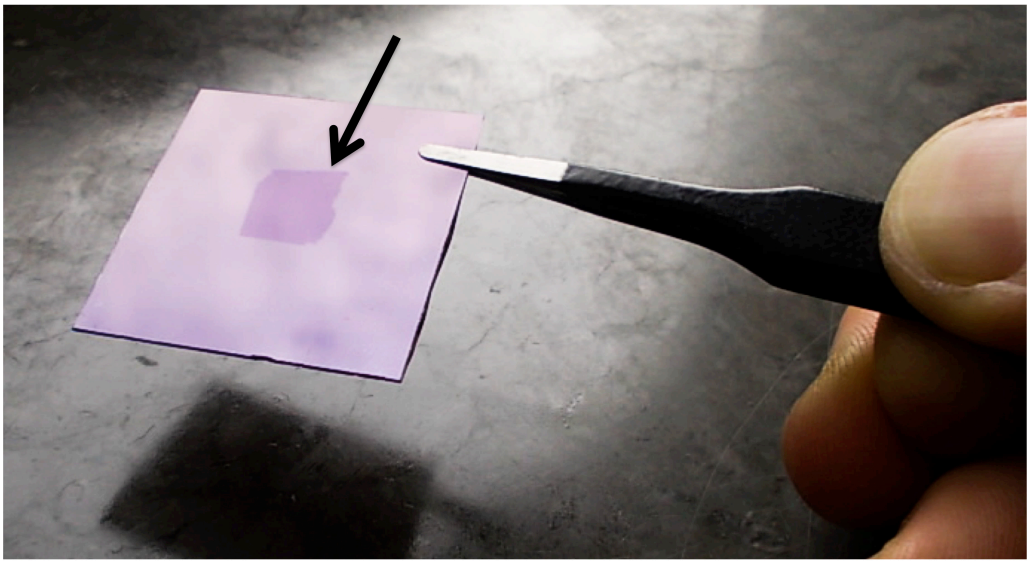

Figure 3.3: Photograph of Cu-grown graphene transferred to 300 nm SiO_2. The arrow points at the cm-sized graphene, which is easily visible by the naked eye. Photo courtesy of Jie Sun [115].

copolymer is removed in acetone leaving graphene at the target substrate. A photograph of cm-sized transferred graphene on SiO_2 is shown in Figure 3.3 [115].

3.3 Hydrogen bubbling graphene transfer

Wet chemical etching of the metal catalyst is a straightforward and successful method to transfer graphene. It suffers, however, from two main disadvantages. First, copper is consumed which adds cost as well as negative environmental impact. Also, while Cu is not scarce, it could still in the long run constitute a problem [116]. Second, this technique does not work for all metals. Noble metals such as platinum cannot be easily chemically etched.

An alternative to chemical etching is to delaminate graphene from catalyst using hydrogen bubbling [117]. With slight modifications this technique can be used both for graphene on Pt and on Cu [118]. First, the top-side graphene is covered by a polymer, typically polymethyl-methacrylate (PMMA), which acts as a mechanical support during subsequent processing. The back-side graphene is removed using oxygen plasma. To simplify handling of the PMMA/graphene stack, a polyethylene terephthalate (PET) frame is glued around the edges. Several different glues were tried. One simple and well-working solution is to use drop casted and cured PMMA as glue.

The device is then connected to an electrode and submerged in an electrochemical cell with NaOH-in-water solution. A current is applied between a reference Pt electrode and the graphene/Cu stack, which is connected to the cathode. At the cathode and anode, hydrogen- and oxygen gas bubbles are produced, respectively. This can be described by:

$$4H_2O_{(l)} + 4e^- \rightarrow 2H_{2_{(g)}} + 4OH^-_{(aq)}, \tag{2.19}$$

$$2H_2O_{(l)} - 4e^- \rightarrow O_{2_{(g)}} + 4H^+_{(aq)}, \tag{2.20}$$

respectively. The moderate currents applied (approximately 1 A) during delamination keep NaOH, used to increase the conductivity of the solution, from producing Na^+. After approximately 30-60 s, the PET/PMMA/graphene heterostructure delaminates from the metal. The time needed for delamination depends both on the applied current and the sample geometry. A schematic overview of the process is shown in Figure 3.4.

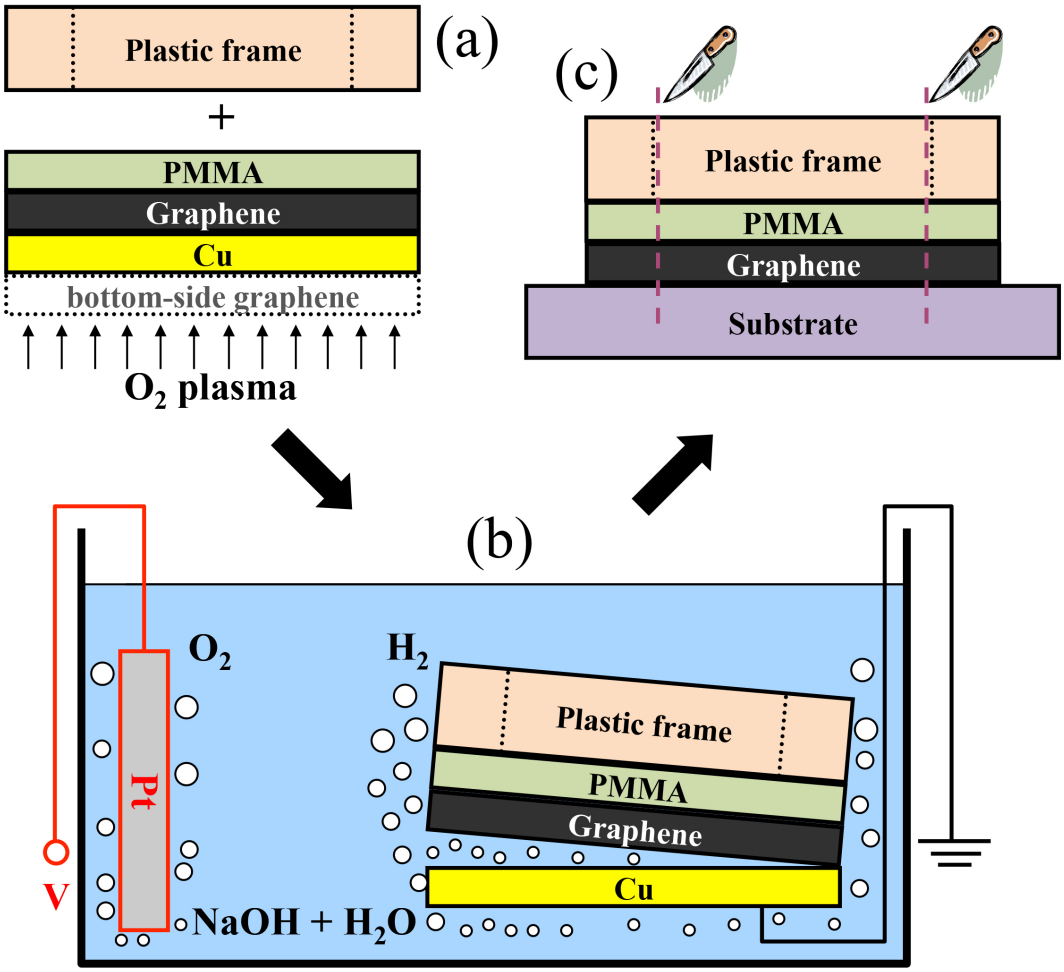

Figure 3.4: (a) The top-side graphene is covered with PMMA and a plastic frame is glued on. The back-side graphene is removed using oxygen plasma. (b) The Cu is connected to the cathode of an electrolytic cell and submerged into $NaOH + H_2O$ solution. A current is applied and hydrogen bubbles delaminate graphene from Cu. (c) Finally, the graphene is applied to the target substrate. Adapted from original in paper **II** with permission from Jie Sun [119].

The delaminated PMMA stack is cleaned thoroughly in water to remove contaminants from the electrolyte solution. It is placed on the desired target substrate and left to dry in ambient atmosphere for at least an hour. Then, it is baked at 160 °C for 10 min to improve adhesion and to remove any residual water. Finally, the frame is cut out using a scalpel and PMMA removed by hot acetone. Only a very small part of the Cu catalyst is consumed in the process. In fact, it is electrochemically polished by the hydrogen bubbling procedure, which can be beneficial for the next growth cycle using the same metal piece. Images from the bubbling transfer are shown in Figure 3.5.

CVD graphene transferred using both wet chemical etching and hydrogen bubbling are used for the different works in this thesis.

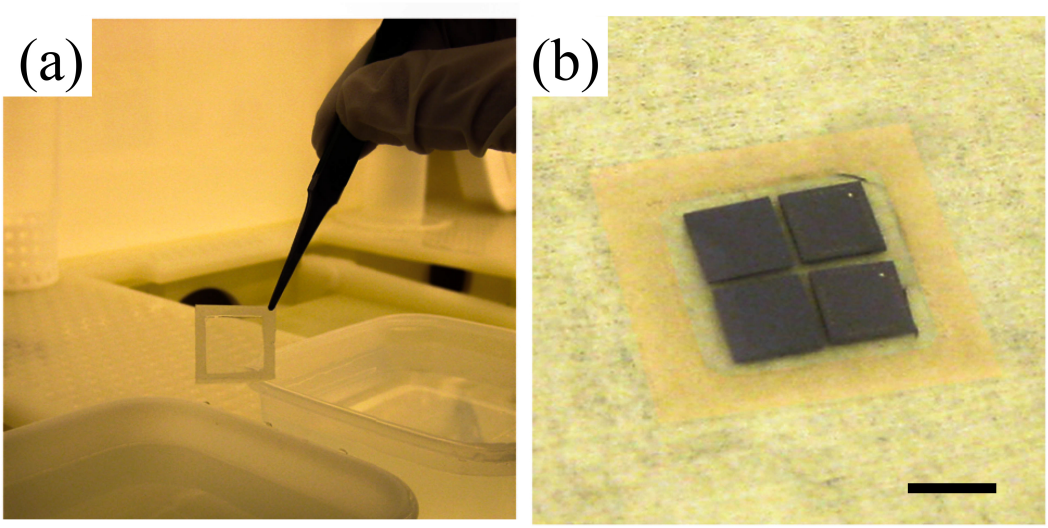

Figure 3.5: (a) The PET frame facilitates sample handling during the transfer process. The PMMA/graphene structure is quite durable and almost fully transparent. (b). After thorough rinsing in water, the frame is put with graphene-side down on the target substrates and left to dry before removal of PMMA. The scale-bar is 6 mm. Adapted from original in paper **II** with permission from Jie Sun [119].

3.4 Chemical vapor deposition on insulators

Graphene CVD on copper foils can produce large-area high-quality graphene of reasonably good uniformity. However, the necessary transfer from metal catalyst to dielectric substrate, which is needed for almost any application, introduces several issues. These include wrinkle formation, holes and cracks in graphene, added doping from chemicals and polymers used, and etching residues. While it is possible to optimize the transfer process to limit these effects, they cannot be completely avoided. This is true both for wet etching- and hydrogen bubbling transfer. Also, the wet transfer method is not easily integrated in semiconductor device fabrication. Hence, a transfer-free CVD method is desired.

We found that it is possible to grow nanocrystalline graphene directly on insulating substrates including SiO_2 [120, 121], HfO_2 [122], Al_2O_3 [121, 123, 124], Si_3N_4 [122], and practically any other high temperature compatible planar material by CVD [121]. Other groups also found similar results for ZnS [125], MgO [126], and BN [127]. Previously, attempts have been made to grow graphene directly on insulators but they yielded discontinuous graphene or graphene with unknown electrical properties [109, 128]. It has also been shown that graphene can be grown on insulators by passing the carbon-containing gas over a catalyst before it arrives at the target substrate, so called remote catalyzation [129].

We believe that contrary to the growth process of graphene on metals, this is a non-catalytic reaction where the hot and flat substrate merely serves as a template for

graphene formation. The formation mechanism is further discussed in Chapter 4.3 in light of the experimental results. Synthetic graphite is normally produced at >3000 °C and catalysts are needed to lower the growth temperature as described earlier [130]. However, nanocrystalline graphite can be grown at much lower temperature. While graphene grown non-catalytically share some of the properties of large-crystal graphene, its electrical properties are worse. For some applications, however, it may still prove useful. Since the graphene grows directly on insulating substrates, there is no need for transfer and hence any transfer-related issues are avoided. Also, it makes the integration into semiconductor processing easier.

A typical process for the direct growth of graphene on SiO_2/Si substrates is as follows. The growth chamber is the same as is described in Figure 3.2(a). Instead of the copper foil, SiO_2/Si chips are put on the graphite heater. After evacuating the growth chamber, a flow of 20 sccm H_2 and 1000 sccm Ar is introduced. The system is heated to 1000 °C at a rate of 300 °C/min. A C_2H_2 (acetylene) flow of 20 sccm is introduced during carbon deposition. The ambient pressure in the chamber is around 8 mbar with a 0.15 mbar partial pressure of acetylene. The main practical difference compared to catalytic graphene growth is the use of significantly higher partial pressure of the carbon precursor. Also, using acetylene instead of methane as carbon

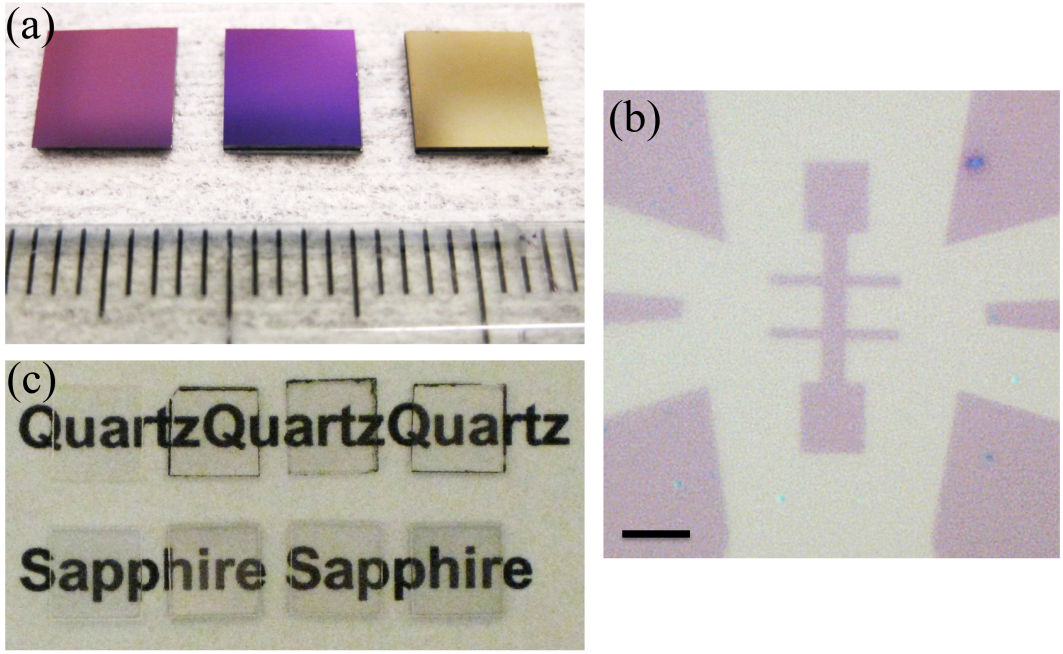

Figure 3.6: (a) Optical photograph of the 300 nm SiO_2 substrate (left), nominally monolayer graphene (middle), and ~70 nm thick shiny graphite (right). The substrates are 6 × 6 mm^2 (b) Optical micrograph of non-catalytically grown graphene patterned into a Hall-bar structure. The scale-bar is 5 µm. (c) Optical photograph of graphene grown directly on transparent quartz (top row) and sapphire (bottom row). The substrates are 5 × 5 mm^2. The images in (a) and (c) are adapted from originals in [121] with permission from Jie Sun [119].

precursor gives more carbon atoms.

Since this type of graphene growth is not a surface catalytic process, it is not self-limiting but instead controlled by temperature, gas concentration, choice of carbon precursor gas, and the deposition time. The process is quite slow but reproducible. For the growth on SiO_2, a deposition time of 15-20 min yields a continuous film with optical properties similar to those of high-quality monolayer graphene. If the growth is continued for a longer time, more layers form and the optical transparency gradually decreases. Finally, the samples are cooled to room temperature in H_2 + Ar atmosphere.

The films are optically uniform independent of the growth time. Eventually tens of nanometer thick graphitic films are obtained having shiny color. This in contrast to growing graphene on insulating substrates in other groups, where the films turn black after certain thickness, similar to carbon black [131]. Optical images of non-catalytically grown graphene on both opaque- and transparent substrates and using different deposition times are shown in Figure 3.6.

3.5 Suspended graphene

The high mechanical strength and flexibility of graphene combined with its electrical properties make it interesting for use in NEMS [132]. Graphene resonators made from exfoliated graphene have been studied using both optical- [133] and electrical readouts [134, 135]. For realistic use in applications, the use of graphene grown by a scalable method, e.g. CVD, is necessary. Indeed, CVD-grown graphene was used to make both single devices and arrays of graphene resonators [136, 137]. The performance of such resonators is promising. However, the fabrication procedure requires the transfer of graphene from the catalytic growth template to the desired target substrate, a process that reduces the reproducibility. To overcome this, we use graphene grown directly on SiO_2 as described in Chapter 3.4.

Suspended graphene structures on SiO_2/Si can be realized by chemically removing part of the SiO_2 using a HF-based, buffered oxide etch (BOE) [138]. First, graphene is patterned using electron beam lithography (EBL) and oxygen plasma etching. In a second EBL step, Au (150 nm)/Cr (3 nm) electrodes are patterned. These electrodes also serve as etching mask in the following BOE oxide wet etch step, where approximately 250 nm SiO_2 of a total of 300 nm is removed. SiO_2 is readily removed from non-masked areas, including under graphene. It is also removed under the part of graphene covered by electrodes [138].

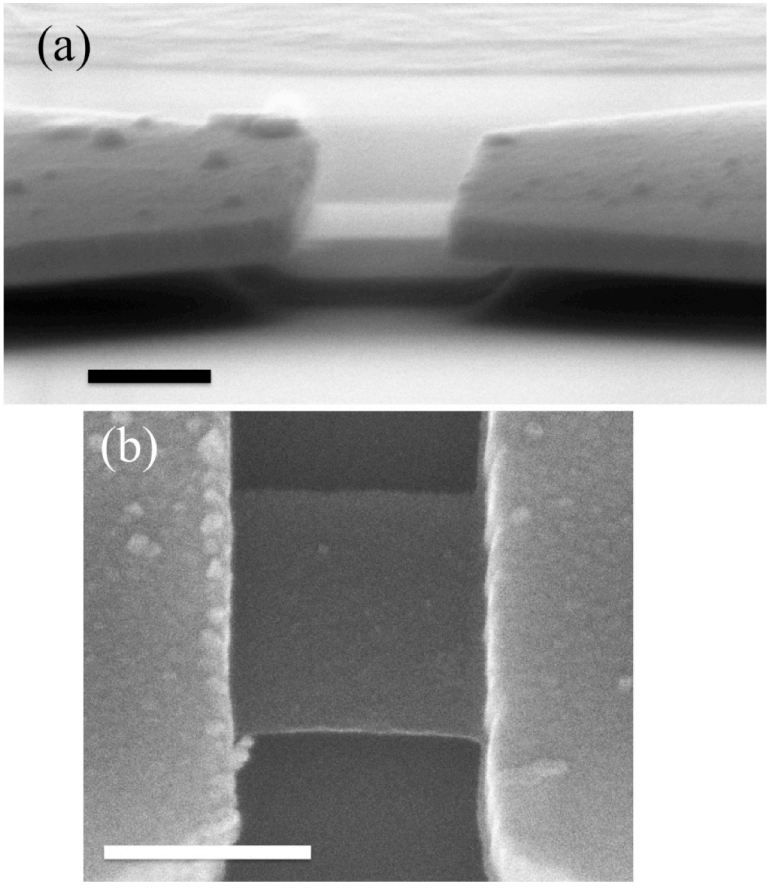

Figure 3.7: (a) SEM micrograph of a suspended graphene device (the bright middle part) made from non-catalytically grown CVD graphene. The micrograph is taken at high angle to visualize that SiO_2 is removed under graphene and somewhat also under the electrodes. The scale-bar is 500 nm. (b) Top-view SEM micrograph of a similar device showing apparently uniform and flat graphene. The scale-bar is 500 nm. Adapted from paper **IV.**

To stop the etching process, the sample is cleaned in water and subsequently transferred to either ethanol or isopropanol solution. The sample is kept in liquid at all times. Finally, critical point drying is used to remove liquid from the suspended graphene and substrate while avoiding capillary forces that are strong enough to damage graphene. Scanning electron microscopy (SEM) micrographs of the final device are shown in Figure 3.7.

3.6 Substrate layout and nanofabrication

This chapter briefly describes a typical experimental platform for graphene experiments. Also, some key nanofabrication techniques used to fabricate graphene devices are explained.

In this thesis, Si substrates (n++) with ~300 nm dry thermal SiO_2 are used if not stated otherwise. Such substrates give high graphene visibility as explained in Chapter 2.8. Due to the high doping of the Si substrate, it has metallic resistivity

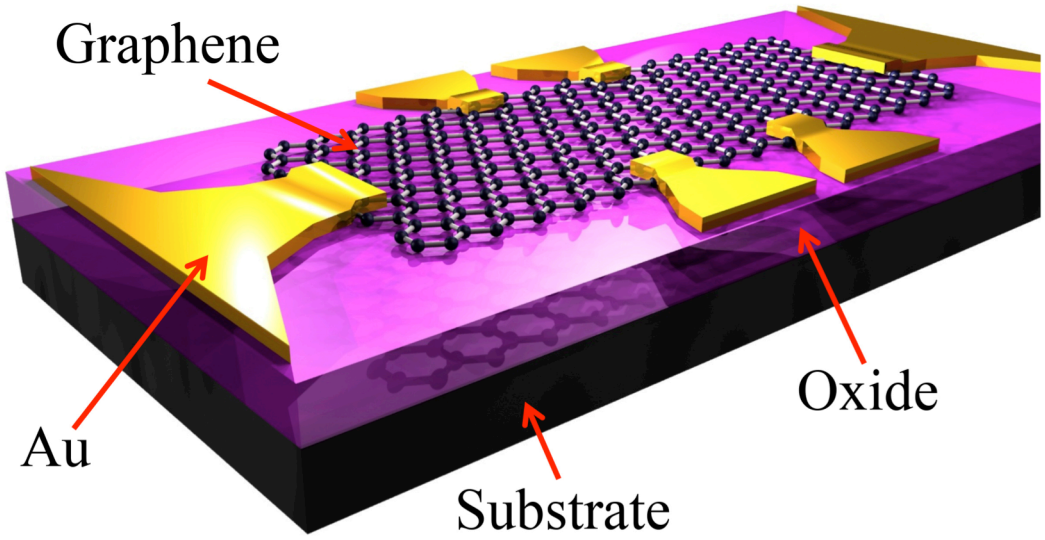

Figure 3.8: Typical graphene sample layout. Graphene is deposited on an oxide, typically SiO_2, lying on an opaque, conducting substrate. Au electrodes with either Ti or Cr adhesion layer are deposited on top. Graphene is patterned using oxygen plasma etching.

<0.005 Ωcm. Hence the substrate can be used as a back gate electrode with the SiO_2 layer acting as the gate dielectric. While SiO_2/Si substrates are not ideal for graphene due to trapped charges, it is a convenient choice in terms of device fabrication. Figure 3.8 shows the typical sample layout. To be able to determine the position of a suitable graphene area and to find it in coming lithography steps, a grid of gold alignment marks is pre-patterned on the substrates. Graphene is put on top of the SiO_2. It is then patterned and electrodes are deposited.

Two commonly used fabrication procedures will be presented in the following paragraphs. While a larger set of different techniques are used for the graphene processing, a majority of those are just varieties of the two described here.

Patterning graphene

Samples are first thoroughly cleaned in organic solvents. A thin (100 nm) layer of high-resolution positive EBL resist (ZEP520A) is deposited using spin coating and cured on hot plate. The resist is patterned using EBL where a high-energy electron beam is scanned over parts of the sample. After exposure to the beam, the resist changes its chemical configuration making it solvable in certain liquids. O-xylene, an organic solvent, is used to remove exposed parts of the resist in our case. In this way, a desired pattern is transferred to resist. Areas of graphene unprotected by resist are then removed using a mild oxygen plasma etching (10 s at 50 W). Finally, all the resist is removed using organic solvents. Figure 3.9(a-b) shows a graphene flake before and after patterning, respectively.

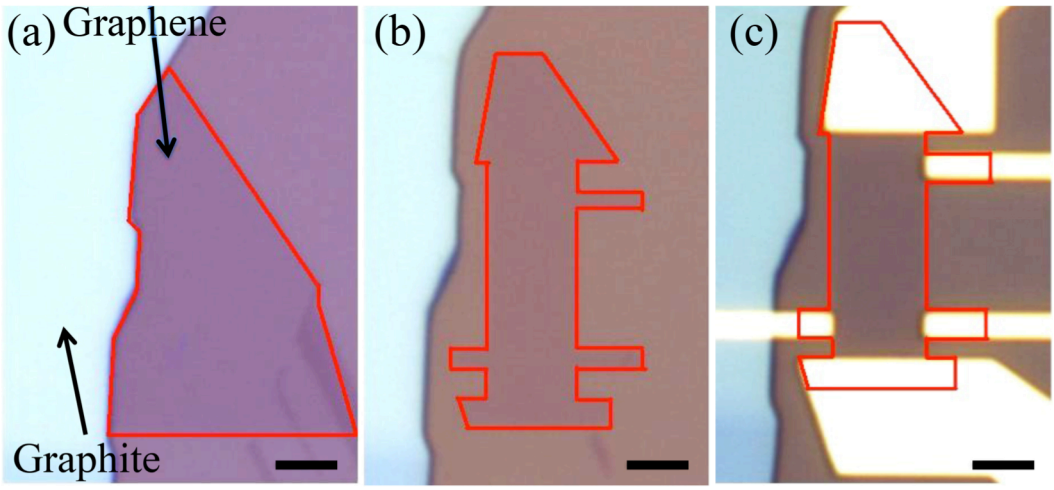

Figure 3.9: Typical graphene fabrication procedure. (a) A graphene flake, attached to a thicker piece of graphite, is located in optical microscope. The graphene is outlined in red. (b) EBL and oxygen plasma etching are used to pattern the graphene. The mild oxygen plasma etching of 10 s at 50 W is sufficient to etch monolayer graphene but only a few layers of the thick graphite piece are removed. (c) Au/Ti electrodes are patterned and deposited in a second EBL step followed by electron beam evaporation. All scale-bars are 2 μm.

Depositing electrodes

After cleaning with organic solvents, a double-layer resist stack consisting of copolymer underlayer (MMA(8.5)MAA (EL10), 350 nm) and PMMA (60 nm) top layer are deposited by spin coating and cured on hot plate. The double-layer structure is utilized to create a certain profile in the resist where the top part is hanging out from the resist stack at the edges.

Resists are patterned by EBL and developed in a mixture of methyl isobutyl ketone and isopropanol. The top layer resist is sensitive to the electron beam as described above and selectively removed when developed. The bottom layer, however, does not require exposure but is solvable already. By controlling the development time, a certain amount of the bottom layer is removed, creating the desired profile of the resist stack.

Metal electrodes, typically Au with either a Cr or Ti thin underlayer to improve adhesion, are deposited by electron beam evaporation. Finally, the remaining resist stack is removed in a lift-off step. Figure 3.9(c) shows the final device with Au electrodes after lift-off.

More detailed recipes for two common lithography procedures are available in Appendix A.

4 Material characterization

In this chapter, field-effect- and high magnetic field measurements are used to investigate the electronic properties of the different graphene materials described in Chapter 3. In Chapter 4.1, graphene produced by mechanical exfoliation is characterized showing excellent electronic properties and the IQHE. The properties of CVD-grown graphene on copper catalysts are shown in Chapter 4.2 and for non-catalytically grown graphene in Chapter 4.3. Raman characterization and electron microscopy images for CVD-grown graphene are also presented.

4.1 Graphene produced by mechanical exfoliation

Much of the interest in graphene is related to its electronic properties. By using the conducting Si substrate as a back gate, a simple graphene field-effect transistor is realized. The electronic properties of the graphene device are extracted from measurements of graphene resistance while varying the voltage of the gate. Figure 4.1(a) shows a room-temperature four-probe measurement of the resistance of an exfoliated graphene device as a function of the gate voltage V_g minus the Dirac voltage, V_D. $V_D = -2$ V, indicating little n-type doping. An optical image of the measured device is shown in Figure 4.1(b).

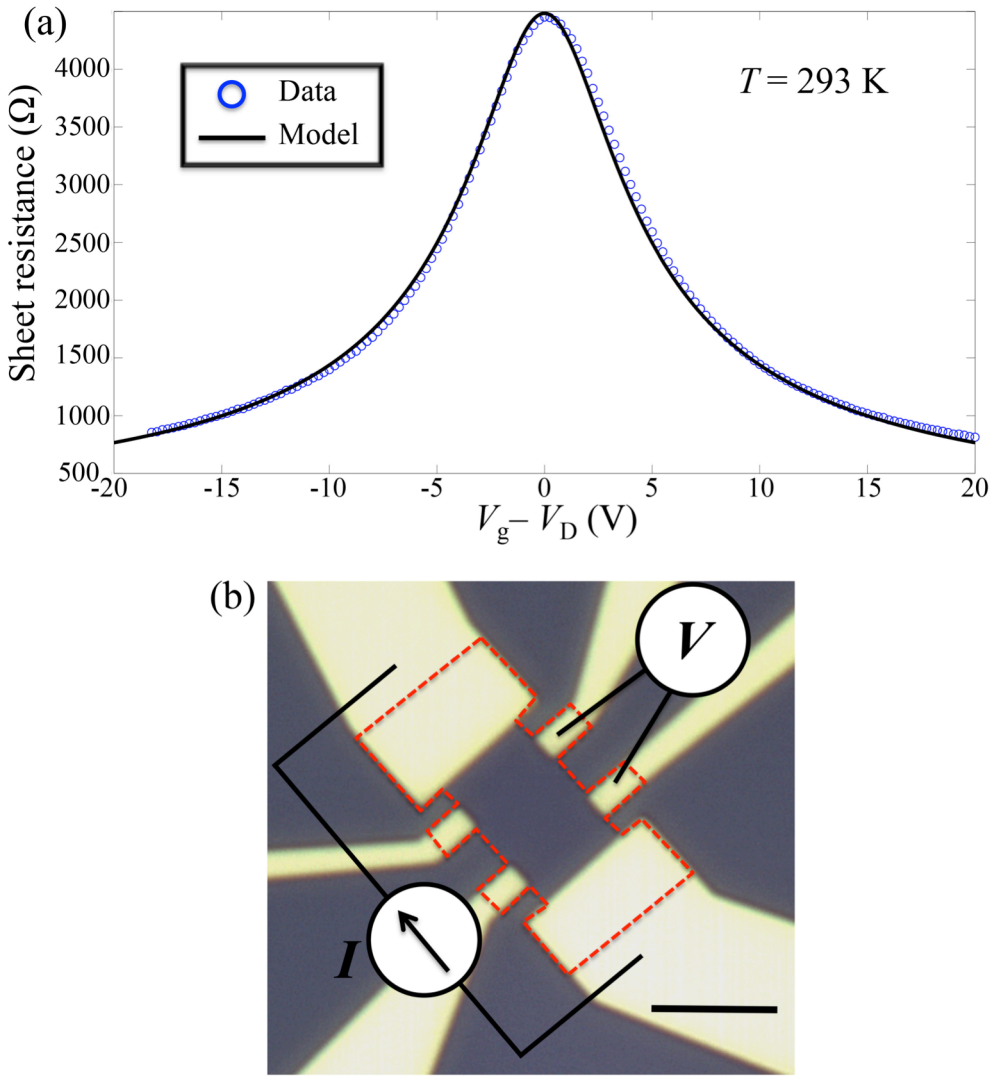

Figure 4.1: (a) Sheet resistance as a function of V_g-V_D at room temperature (blue circles) and the theoretical model (solid black line). From the model in equation (2.2), we extract the values for $\mu = 5900$ cm^2/Vs and $n_0 = 2.4 \cdot 10^{11}$ cm^{-2}. (b) Optical micrograph of the device in (a). The graphene is outlined with the red dotted line. The scale-bar is 5 µm.

The blue circles represent the measured data and the solid black line the numerical model described by equation (2.2). Extracted values for the mobility μ and the residual charge carrier concentration n_0 are 5900 cm^2/Vs and $2.4 \cdot 10^{11}$ cm^{-2}, respectively. From the model we obtain $R_0 = 40$ Ω, which is negligible compared to the overall resistance (~kΩ) as expected from four-probe measurements and explained in Chapter 2.2.

To further characterize the exfoliated graphene devices, they are cooled to cryogenic temperatures (2-20 K) and measured in high magnetic fields (≲14 T). The mobility typically increases at low temperature. In Figure 4.2, ρ_{xx} and ρ_{xy} are shown as a function of magnetic field at 20 K for another sample. At high magnetic fields we first observe Shubnikov-de Haas oscillations and eventually the IQHE where the

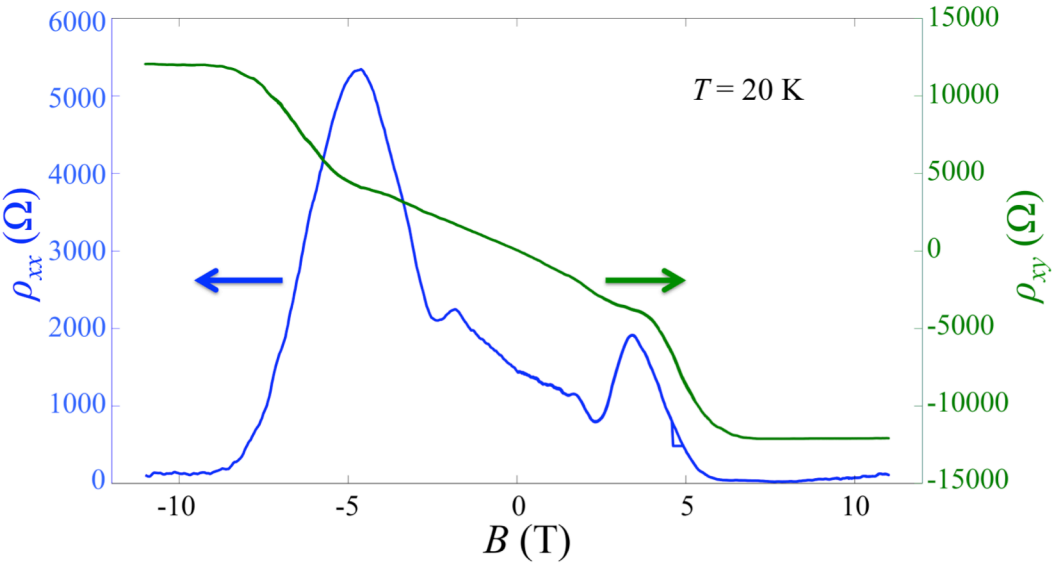

Figure 4.2: The half-integer quantum Hall effect in exfoliated graphene at 20 K. At ~6 T, a Hall plateau becomes visible accompanied by vanishing longitudinal resistivity. This is the quantum Hall effect. For negative field similar behavior is seen. At lower magnetic fields, Shubnikov-de Haas oscillations are observed. The values at which ρ_{xy} are quantized is a signature of monolayer graphene.

longitudinal resistivity ρ_{xx} vanishes. From the low-field behavior of the Hall resistivity ρ_{xy} we extract a carrier mobility of ~7000 cm^2/Vs. At higher fields, ρ_{xy} accompanies the vanishing ρ_{xx} by saturating at a plateau of the theoretical value 12.9 kΩ given by equation (2.10). The second plateau at 4.30 kΩ, is less visible. The observation of these features show that the sample is indeed monolayer graphene.

As described in Chapter 2.4, it is also possible to keep the magnetic field constant and instead vary the Fermi level by applying a gate voltage. This is shown for another sample in Figure 4.3. The magnetic field is kept constant at 14 T while varying the gate voltage between -60 V and +60 V. The 12.9 kΩ, 4.30 kΩ, and 2.6 kΩ plateaus are clearly seen in ρ_{xy}. For negative gate voltages, additional plateaus are visible.

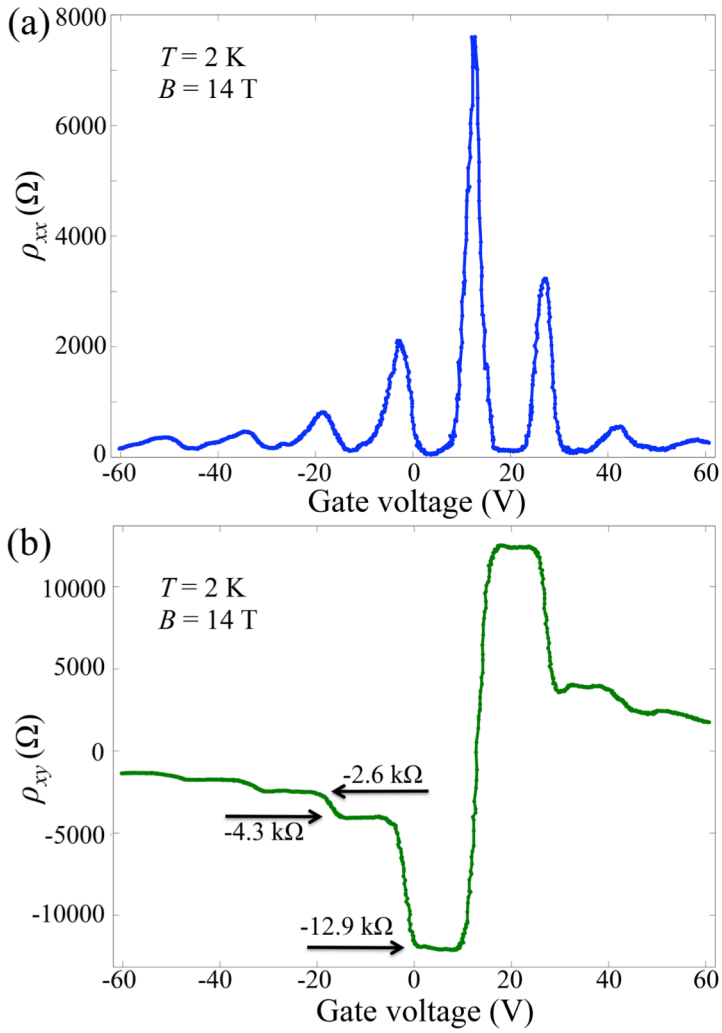

Figure 4.3: (a) Longitudinal resistivity of exfoliated graphene as a function of gate voltage at 2 K and 14 T. The data is recorded for a different sample than that of Figure 4.2. (b) Corresponding Hall resistivity. Quantum Hall plateaus at 12.9 kΩ, 4.3 kΩ, and 2.6 kΩ are clearly seen. Additional plateaus are visible for negative gate voltages.

4.2 Graphene produced by catalytic chemical vapor deposition

The graphene grown on Cu by CVD is transferred to standard SiO_2/Si substrates for electrical characterization. Achieving a high uniformity and reproducibility is equally important as achieving a high mobility. Hence, several (~20) devices are fabricated on each chip to probe the reproducibility. Some devices are intentionally made at places where graphene looks optically uniform. High reproducibility is achieved in this case. When devices are made at random, the performance is sometimes poor, showing that there are areas in the material with inferior properties. This could be related to catalyst preparation procedures and the transfer process.

Room temperature field-effect measurements of three different devices on the same chip are shown in Figure 4.4(a). Four-probe resistance is shown as a function of V_g together with the model fit of equation (2.2). The Dirac voltage was situated at

~15 V for all three devices having the same dimensions. Figure 4.4(b) shows an optical image of one of the devices. The mobility varies slightly between devices between 2600 and 3400 cm^2/Vs. The residual charge carrier concentration is in the range 4.4-4.9 $\cdot 10^{11}$ cm^{-2}.

There were a few measurements performed at low temperature and in high magnetic fields for devices made from Cu-grown graphene (data not shown in this thesis). They show carrier mobility similar to the values obtained from room-temperature gate-dependence measurements (as in Figure 4.4(a)), but no IQHE.

Raman spectroscopy also provides information about the quality of graphene, including the chemical configuration, the defect density, and the number of layers. In

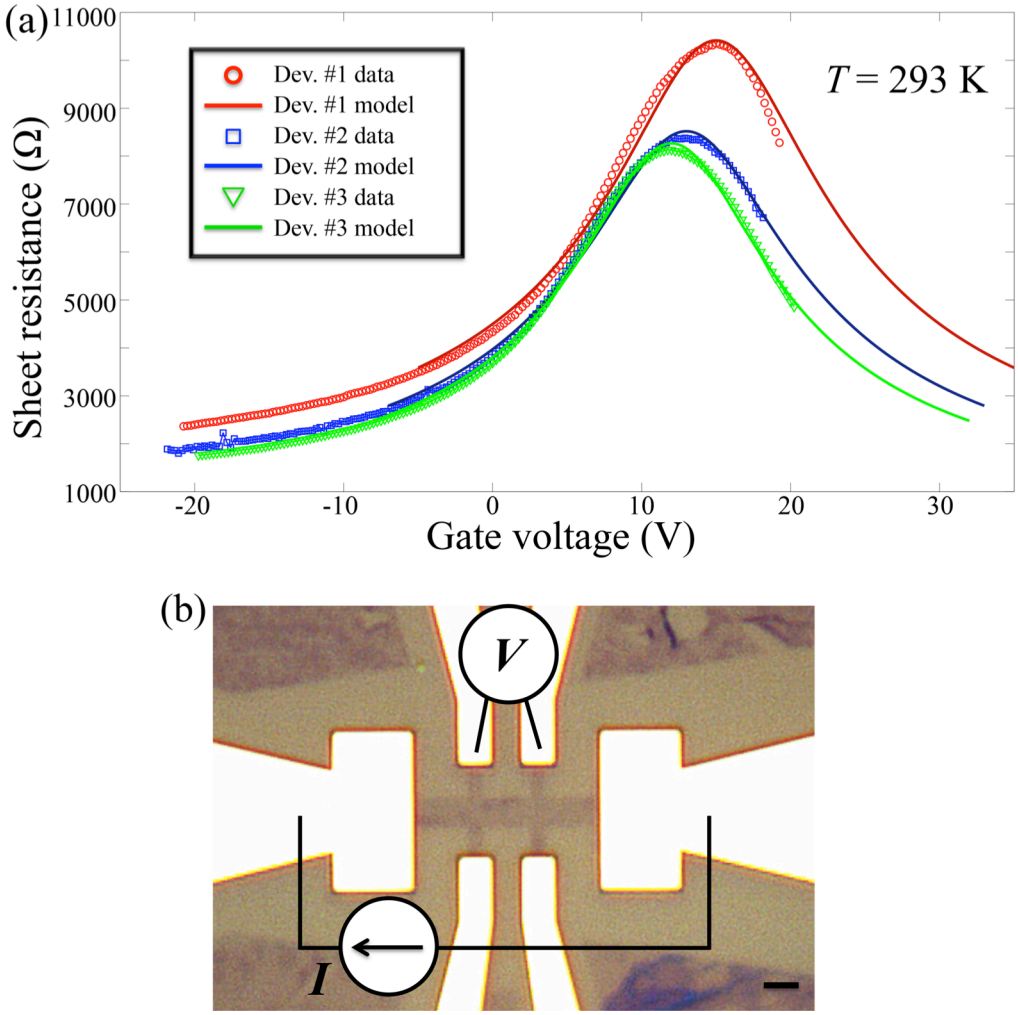

Figure 4.4: (a) Sheet resistance as a function of gate voltage for three similar devices on the same chip at room temperature. The graphene is grown on copper foil and transferred to SiO_2/Si substrates. The devices have similar doping with mobilities between 2600 and 3400 cm^2/Vs at room temperature. (b) Optical image of one of the devices. Holes and other non-uniformities are observed in the graphene surrounding the device. The scale-bar is 2 μm.

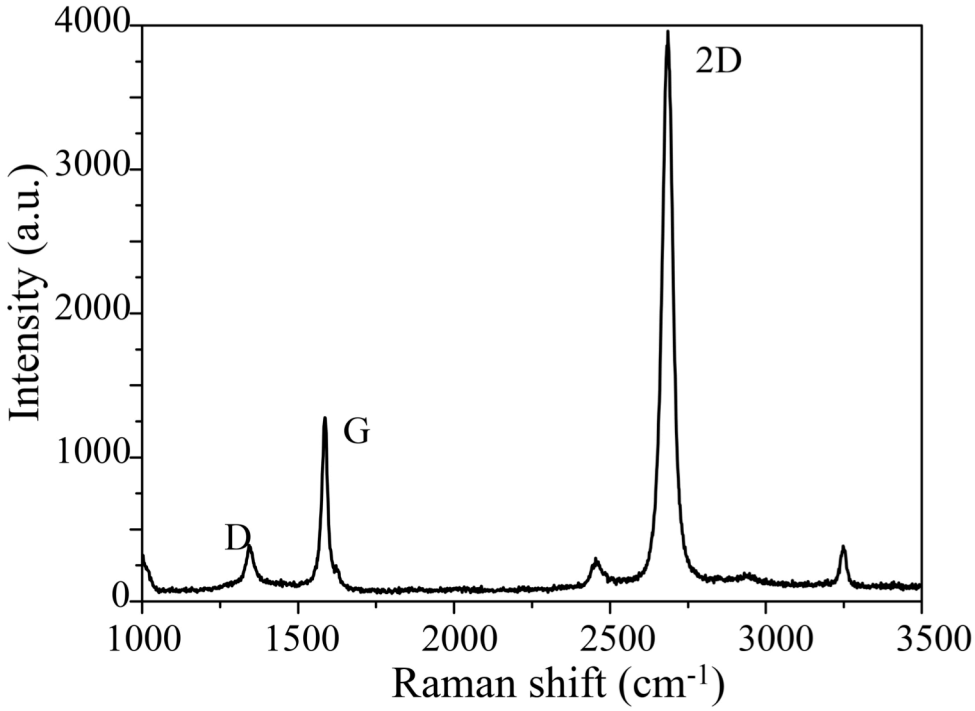

Figure 4.5: Raman spectrum of Cu-grown graphene transferred to SiO_2/Si substrate. The 2D peak can be fitted with a single Lorentzian and its intensity is more than twice than that of the G peak, which is characteristic for monolayer graphene. There is also a small D peak indicating some disorder in the film. Peaks at 2450 cm^{-1} and 3250 cm^{-1} are attributed to higher-order Raman signals. Adapted from original in paper **I**.

this work it is used a probe of both the quality and uniformity of a graphene device. A typical Raman spectrum for graphene grown on copper and transferred to SiO_2/Si substrate is shown in Figure 4.5. The strong 2D peak (~2683 cm^{-1}) with intensity larger than twice that of the G peak (~1591 cm^{-1}) can be fitted with a single Lorentzian, indicating that the sample is monolayer graphene. There is also a small D peak (~1350 cm^{-1}) indicating some disorder in the film. The combination of a large $I_{2D}/I_G = 3$- and a small $I_D/I_G = 0.2$ intensity ratio shows that the graphene is of reasonably high quality.

Transmission electron microscopy (TEM) imaging of the Cu-grown graphene was also performed and is presented in Chapter 4.3.

4.3 Graphene produced by non-catalytic chemical vapor deposition

The most significant difference between non-catalytically grown graphene on insulators and graphene grown on Cu is the order of magnitude smaller grain size. Indirect measurements of the grain size obtained by different methods are provided in this chapter. The smaller grain size leads to worse electronic properties compared to catalytically grown graphene. Field-effect measurements of graphene grown on Si_3N_4 are shown in Figure 4.6(a). The graphene used in this particular device shows optical

properties similar to those of exfoliated high-quality graphene as measured by spectroscopic ellipsometry (as seen in the supplementary information of [121]). Upon applying gate voltage in the range -20 V to +40 V, there is only about 25 % modulation of resistance, showing that the mobility is very low. The model described by equation (2.2) is not suitable with such poor electronic behavior but instead the mobility can be estimated directly from the simpler Drude model described by equation (2.4). It is in the order of tens of cm^2/Vs, varying only slightly with the growth substrate. The samples are also measured in magnetic fields at both room- and low temperature. The extracted mobilities from these measurements are in the same range as the ones estimated from equation (2.4), and do not vary significantly with temperature. A strong negative magnetoresistance is observed, even at room temperature, characteristic of disordered carbon materials [69, 139-143]. We fit such data by the theory of weak localization to extract the phase dephasing lengths of the system. These increase from 6-7 nm at room temperature to 10-11 nm at 4 K (for data and a full description, see reference [120]), giving an indication of the typical scattering lengths in the system.

Raman measurements of graphene grown on SiO_2 are shown in Figure 4.6(b). G and 2D peaks are observed at ~1591 cm^{-1} and ~2683 cm^{-1}, respectively, but the features are less sharp than in the case of catalytically grown graphene (shown in Figure 4.5). The distinct peaks differentiate this material from amorphous carbon (α-C), where very wide D and G bands merge together and there is no 2D peak [87, 145-

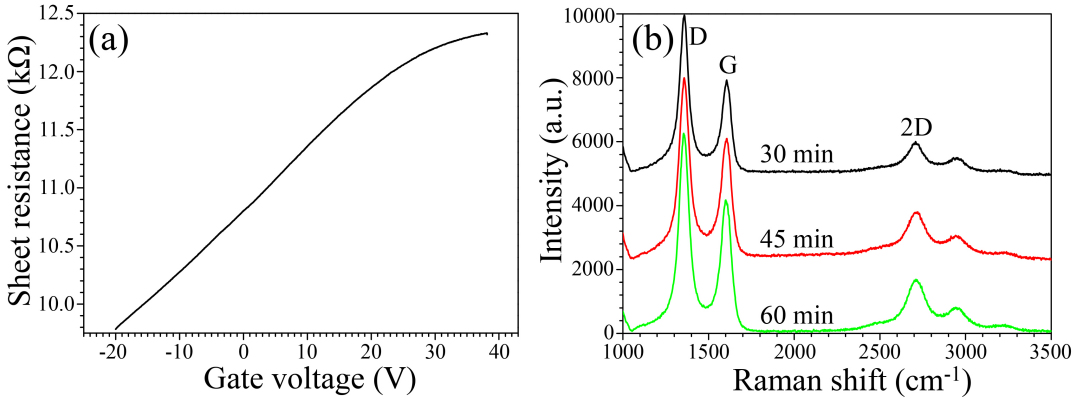

Figure 4.6: (a) Sheet resistance as a function of gate voltage for graphene grown directly on 100 nm thick Si_3N_4. The resistivity is modulated ~25 % for gate voltages between -20 V and +40 V. The Dirac point is not visible, which is typical for this kind of graphene. Adapted from original in paper **III**. (b) Raman spectrum for graphene grown on SiO_2 for 30 min (top), 45 min (middle), and 60 min (bottom). These films show distinct 2D and G peaks, which is characteristic for graphitic carbon. There is also a strong D peak, indicating significant disorder in the films. Curves are shifted along the ordinate for clarity. The figure is adapted from the original in [120] and the measurement was performed by Matthew Cole [144].

147]. The D peak at 1350 cm^{-1} is very pronounced in non-catalytically grown graphene, indicating high disorder. We attribute this to the small grain domain size of this type of graphene compared to the laser spot in the Raman system, which is either ~1 μm or ~10 μm for the systems used in this work. Hence the spot covers numerous domain boundaries leading to the large D peak. The length scale of disorder is roughly estimated by analyzing the intensity ratio I_D/I_G, to be ~7-8 nm [91].

To further analyze the grain structure of the material and directly observe the microscopic structure, TEM analysis is performed. Graphene is transferred to TEM grids consisting of an irregular holey carbon network supported by a copper matrix structure using techniques similar to those described in Chapter 3.2. These are loaded into a TEM operating at a low acceleration voltage (≲80 kV) so as to minimize the induced structural damage to the graphene while imaging [150-153]. Both graphene

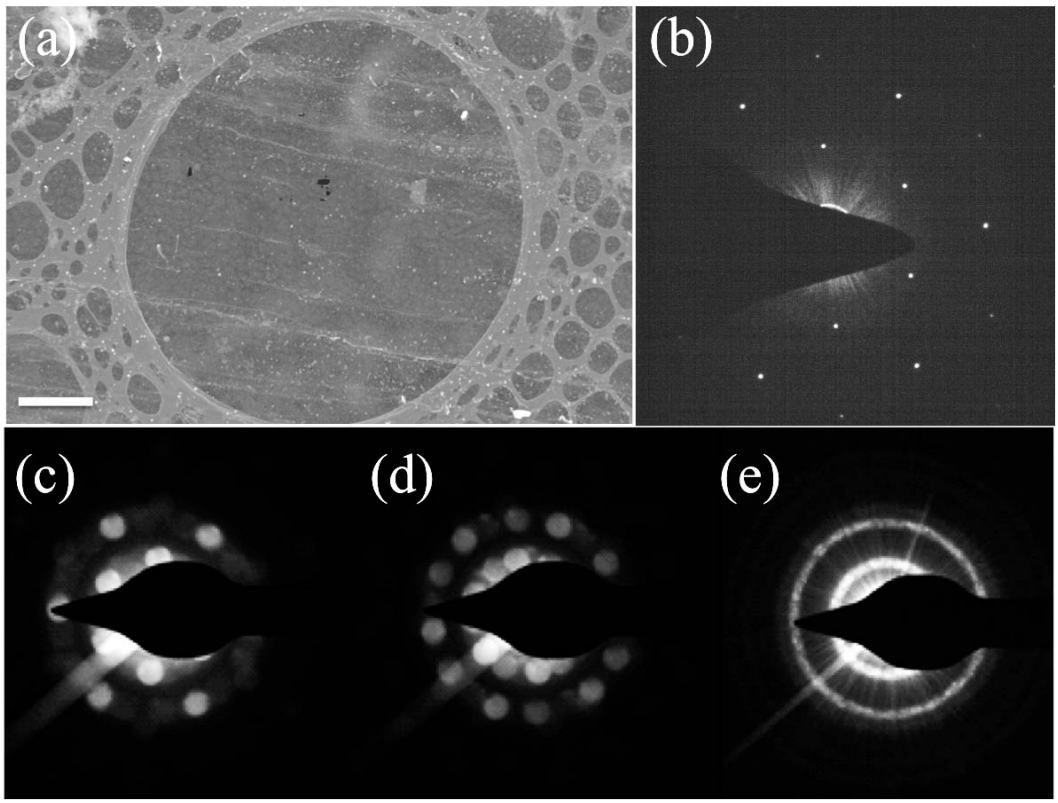

Figure 4.7: (a) SEM micrograph of Cu-grown graphene transferred to a holey carbon TEM grid. The graphene spans over holes up to ~10 μm wide. The scale-bar is 2 μm. (b) TEM diffraction pattern for graphene similar to that in (a). It clearly shows the hexagonal signature of monolayer graphene. Image obtained by Olof Bäcke [148]. (c) TEM diffraction pattern for non-catalytically grown graphene for a focused beam of diameter ~10 nm. For larger beams, hexagonal patterns from two or more domains are observed as seen in (d) and (e), respectively. This shows that the domain size is in the order of ~10 nm. Images in (c-e) are obtained by Tim Booth [149].

grown on copper and on insulators are analyzed in TEM for comparison. In Figure 4.7(a), a SEM micrograph of Cu-grown graphene transferred to a TEM grid is shown. The graphene can span freely over holes up to ~10 μm wide. Diffraction patterns in TEM are presented in Figure 4.7(b) [148] and (c-e) [149] for Cu-grown and non-catalytically grown graphene, respectively. Graphene grown on copper shows the characteristic hexagonal diffraction pattern of monolayer graphene, as expected. The grain size is in the order of μm. For non-catalytically grown graphene, it is also possible to see the diffraction pattern if the beam spot is focused to only ~10 nm. For larger beam sizes, hexagonal patterns from many different graphene domains are obtained. This indicates that the domain size of this material is in the order of ten nanometers, which is consistent with the results obtained from both Raman characterization and magnetotransport measurements.

The properties of non-catalytic graphene are quite different from those of large-crystal graphene obtained from mechanical exfoliation and catalytic CVD on copper. The fundamental difference is the crystal domain size, resulting from different growth mechanisms. Non-catalytic graphene is named such since there is no evidence of catalytic activity of the substrate during film formation. On the contrary, the process is not self-limiting and only weakly dependent on the substrate material. Instead it is believed that graphene flakes form already in the gas phase. At 1000 °C, most of the methane or acetylene has already decomposed. The carbon atoms interact and form chains and small sp^2-hybridized crystallites. Some of these will adhere to the hot and flat target substrate. Larger flakes have a higher probability of staying on the substrate. Light flakes will not sustain the high-energy thermal vibrations of the substrate but will detach. The temperature in our case is still too low to promote realignment and orientation of such larger flakes on the hot substrate [154]. Instead, a patchwork of tiny randomly oriented grains is formed. At yet lower temperature, carbon black will be formed [155-157]. Carbon black is essentially a 3D material consisting of chaotically oriented graphitic flakes. In our case the growth process can be engineered to produce textured graphene films using a hot and flat substrate, high carbon gas concentration, and high temperature.

We made an attempt to make micro-electromechanical resonators from such graphene by suspending it between electrodes. The suspended graphene devices described in Chapter 3.5 were electrically characterized. Before suspension they show similar behavior as shown in Figure 4.6(a). After suspension the resistance is still in the order of ~kΩ. Due to the low mobility of this form of graphene and limited range of gate voltages that can be applied without destroying the suspended structure, no field effect was observed. Hence, electrical readout of mechanical resonances using e.g. mixing was not possible. The main conclusion from these experiments is that even this graphene is mechanically sufficiently strong.

The main advantage of non-catalytic graphene CVD is avoiding the transfer from catalytic growth material to the desired target substrate. The low mobility (tens of cm^2/Vs) so far limits its practical use as, for example, transparent conductives, possibly with the exceptions of touch screens and electrostatic discharge (ESD) applications [52]. Possible ways to improve the conductivity include higher temperature growth on sapphire [123], the use of strong dopants [25], using catalysis elsewhere upstream [129], or making intercalated few-layer graphene [158].

5 Cleaning using atomic force microscope

Being essentially a surface-only material, graphene is easily affected by surface contaminants. In this chapter, a straightforward mechanical technique to obtain atomically smooth graphene with improved electronic properties is presented (paper **V**). Chapter 5.1 discusses doping sources and cleaning techniques for graphene. Then in Chapter 5.2, the mechanical cleaning technique is described as well as the experimental results. Chapter 5.3 provides conclusions.

5.1 Introduction

Charged impurities, surface contaminants, and structural deformation all contribute to local doping of graphene. This leads to an inhomogeneous charge density, the so-called electron-hole puddles, and a shift in Dirac voltage V_D [159-163]. Both the choice of substrate and the microfabrication processing play important roles for the resulting doping. While clever choices of materials and chemicals are needed to limit contamination, residues from fabrication are inherent in any graphene processing. These act as external scattering centers and affect the device properties [138, 164-169].

A variety of techniques exist for cleaning graphene. Standard cleaning using solvents such as acetone is not sufficient to remove all the fabrication residues. The most commonly used cleaning technique is annealing at high temperature, typically ~400 °C in Ar/H_2 environment [98, 164, 165, 167, 170]. While this technique is able to remove most of resist residues through desorption, it may cause increased coupling between the substrate and graphene. This leads to mechanical deformation of the graphene [169]. Also, temperature cycling of only 100–200 K causes rippling of suspended graphene [171]. Both these effects can cause degradation in device performance. Additionally, many substrates cannot sustain high temperature treatment. Some other can, but not without oxygen atmosphere, which is incompatible with graphene. One such example is ferroelectric barium strontium titanate (BSTO) thin films on Nb-doped strontium titanate (Nb-STO) substrates. Due to the polarized

surface, charged contaminants adhere very strongly to these substrates. This renders graphene on BSTO heavily contaminated and difficult to clean.

Another cleaning method is annealing by Joule heating [138, 172]. This technically simple procedure can be done in many setups, including in situ in a cryostat. It is often used for cleaning suspended graphene devices. However, as graphene is heated locally to high temperature it leads to rippling or even breakage if too much current is applied [171, 173].

Recently, mechanical cleaning of graphene was suggested as an alternative [174-177]. It is possible to use the mechanical cleaning method to obtain clean, atomically smooth graphene. The tip of an atomic force microscope (AFM) is scanned in direct mechanical contact with graphene, removing contaminants in broom-like movements. Resist residues are efficiently brushed away, piling up outside the graphene flake. This technique produces atomically smooth graphene with improved electronic properties. Graphene on BSTO/Nb-STO is used in this work as benchmark for the efficiency of the mechanical cleaning method.

5.2 Experiment and results

AFM is used in tapping mode to observe the devices before and after cleaning. In this mode, the interaction between graphene and the AFM is weak and does not influence the graphene. Cleaning is then done in contact mode using several different AFM probes and different forces. This technique can be used on both mechanically exfoliated graphene and CVD-grown graphene. For CVD-grown graphene, care must be taken not to apply too large mechanical force that can damage the graphene. In this thesis, however, all results presented are from exfoliated graphene.

Typical height and phase images of graphene devices on SiO_2 after fabrication are shown in Figure 5.1(a) and (b), respectively. The device is contaminated with resist residues and shows a height root mean square (RMS) roughness R_{RMS} of 0.77 nm and 0.47 nm for a 0.5 x 0.5 μm^2 measurement area of graphene and bare SiO_2 substrate, respectively. For comparison, pristine SiO_2 has a typical R_{RMS} of ~0.2-0.3 nm before processing.

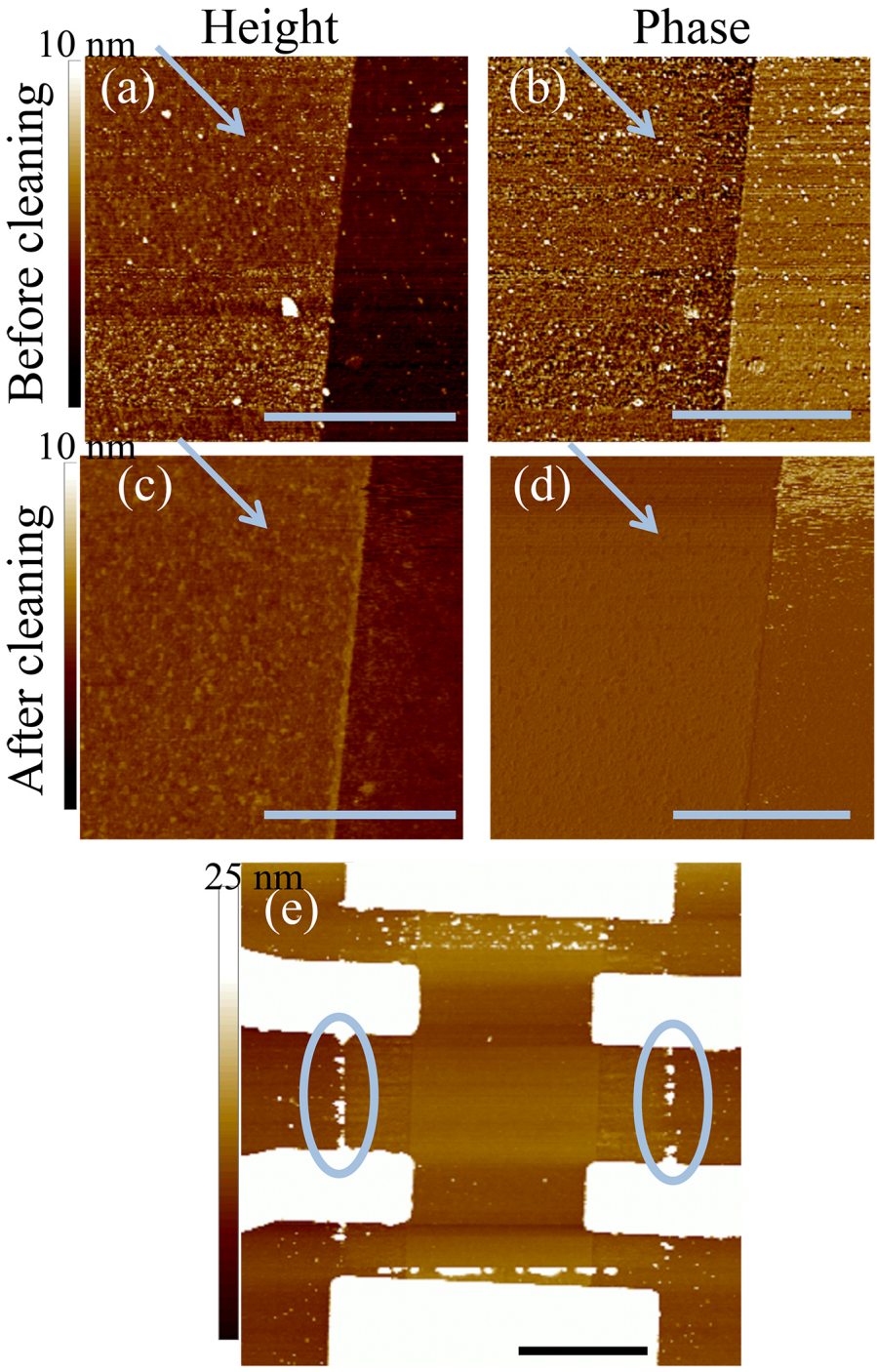

Figure 5.1: Tapping mode height (a) and phase (b) AFM images before cleaning. The device is contaminated and the graphene height RMS roughness is 0.77 nm. (c) and (d) Corresponding height and phase images after four scans in contact mode. The graphene height RMS roughness is reduced to 0.28 nm. The scale-bars in (a-d) are all 1 µm. The z-scales in (a) and (c) are both 10 nm. (e) Overview AFM height image for a graphene Hall-bar device after cleaning. Only the central part was cleaned. The two ellipses mark beads with pushed-away contaminants. The scale-bar is 2 µm and the z-scale is 25 nm. Adapted from paper **V**.

To start the mechanical cleaning, the AFM is then set to contact mode, pushing the TiN-coated Si tip in direct contact with the sample. Contaminants are mechanically pushed to the sides in a broom-like way by scanning the tip back and forth over the sample. Typically three to five such scans are performed. The graphene is generally clean after only two scans and only minor improvement is seen with subsequent cleaning. In Figure 5.1(c) and (d) tapping mode images of the same area as in Figure 5.1(a) and (b) are shown after four scans in contact mode. R_{RMS} is now reduced to 0.28 nm and 0.29 nm for graphene and bare SiO_2 substrate, respectively, similar to the roughness of SiO_2 before processing. The entire cleaning procedure takes about 30 min and depends on the area to be cleaned and the force used.

To further clarify the effect of the cleaning, an overview AFM image obtained in tapping mode is shown in Figure 5.1(e). Only the central area of the device is cleaned in contact mode (both graphene and the surrounding substrate are cleaned). Beads of pushed-away contaminants have formed around the cleaned area, as indicated by the two ellipses. R_{RMS} is significantly larger outside the cleaned area.

A variety of graphene samples were cleaned using this method. R_{RMS} of SiO_2 is in the wide range 0.35–1.40 nm after lithographic processing. For graphene, the corresponding values after device fabrication are $R_{RMS} \sim 0.30$–0.65 nm. The cleaning procedure significantly reduces the roughness. $R_{RMS} \sim 0.18$–0.23 nm and $R_{RMS} \sim 0.12$–0.25 nm are obtained after cleaning for the uncovered SiO_2 substrate and graphene, respectively. Devices on both dry- and wet thermal oxide are studied. Wet oxide is rougher than dry oxide. However, the roughness of graphene depends more on the force applied during AFM cleaning than the type of oxide substrate. When using a stiff cantilever (NSG10/TiN, spring constant $C \sim 15$ N/m) and a large contact force (180 nN), the graphene is pushed down in closer contact with the substrate. This leads to similar roughness for both bare SiO_2 and graphene ($R_{RMS} \sim 0.2$ nm, similar to that of SiO_2 prior to any processing). In contrast, when a softer cantilever (PPP-CONPt-20, $C \sim 0.17$ N/m) and smaller contact force (30 nN) are used, the graphene shows a much lower R_{RMS} than the substrate. For graphene a typical value of $R_{RMS} = 0.13$ nm is obtained. This shows that the graphene conforms significantly less to the substrate when using a moderate contact force during cleaning.

Measuring the step height of graphene flakes on SiO_2 using AFM is not a reliable method for determining the number of layers. It can, however, give indications of the cleanliness of the graphene. After device processing, the measured step height of monolayer graphene (as determined by other techniques) increases to 1.5–2.0 nm. After cleaning it is reduced to 0.6–0.7 nm, which is typical for as-deposited graphene on SiO_2 [178].

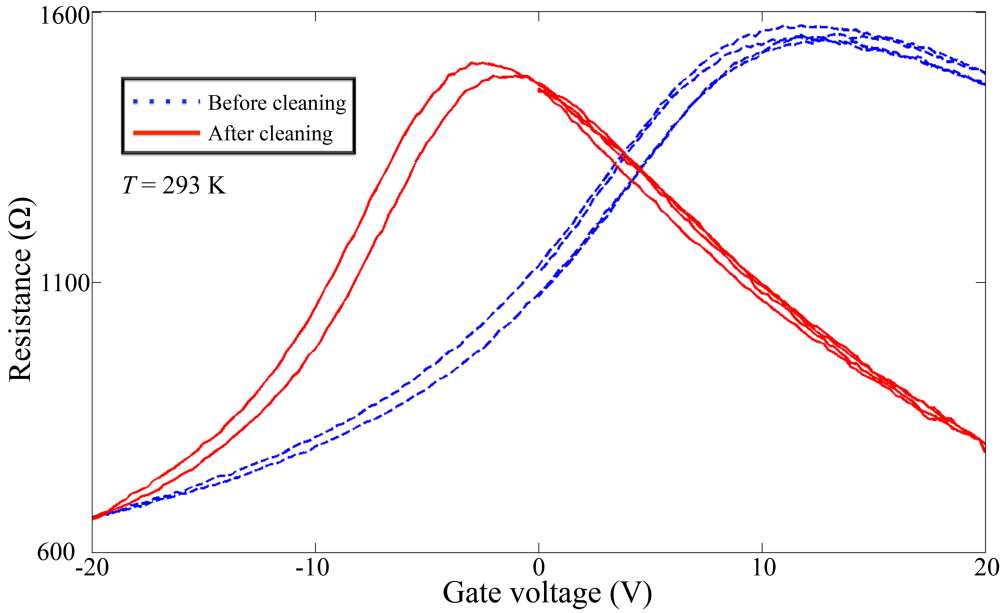

Figure 5.2: Resistance as a function of gate voltage (trace and retrace) before (blue, dashed line) and after (red, solid line) cleaning for a graphene device on SiO_2/Si. The Dirac point moves closer to zero after cleaning and the mobility increases from ~4300 cm^2/Vs to ~7700 cm^2/Vs. Adapted from paper **V**.

To study the effect of the cleaning process on the electronic properties of graphene, samples are measured electrically before and after cleaning. Field-effect measurements are performed at room temperature. The Dirac point V_D consistently shifts closer to zero after cleaning. After fabrication, devices are typically p-doped, showing a positive V_D in the range 12–24 V. After cleaning, V_D is shifts to slightly negative voltages. This observed weak electron doping is probably induced by charges trapped in the oxide. Sometimes the sample is still p-doped after cleaning, but the doping is significantly reduced.

For almost all samples, we also see an increased mobility after cleaning. However, the use of a small contact force is needed for the improvement to be significant. Figure 5.2 shows typical resistance measurements of a graphene device on SiO_2/Si cleaned using a small contact force. The sample changes from p-type doping to slightly n-type doping, as seen by the shift of Dirac voltage (from $V_D = 12$ V to $V_D = -3$ V). The mobility, estimated from the hole-branch of the curve, is increased from ~4300 cm^2/Vs to ~7700 cm^2/Vs.

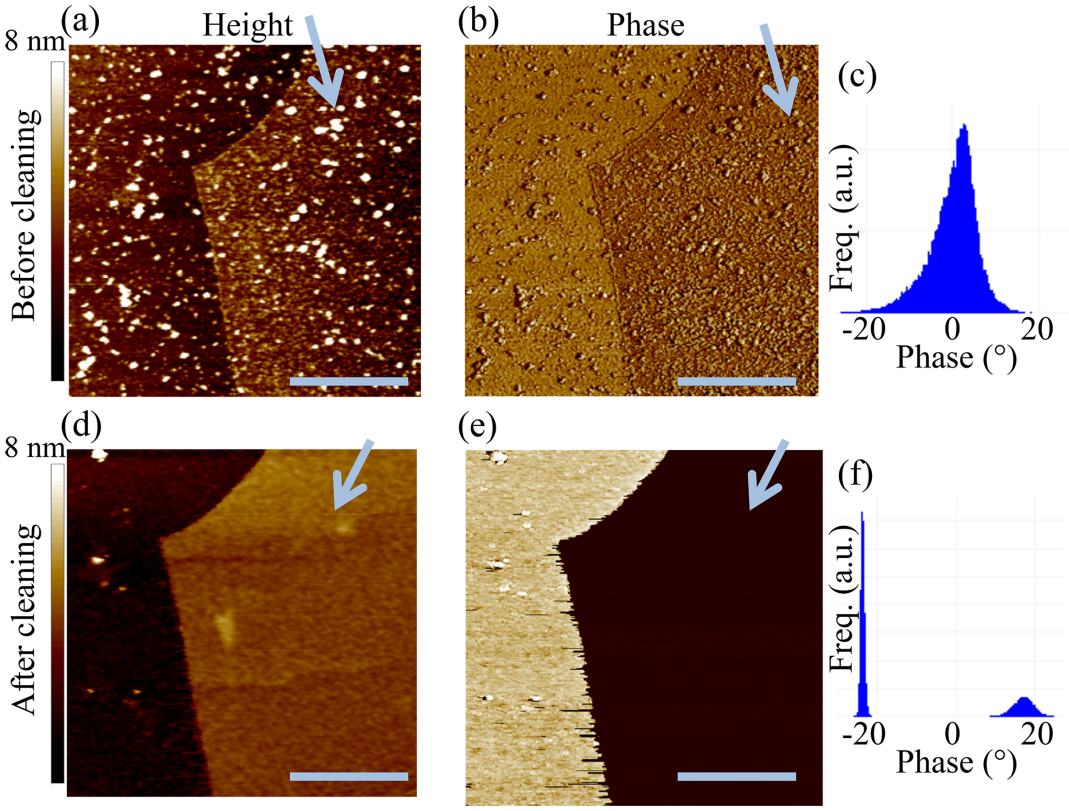

Figure 5.3: (a) AFM height and (b) phase images of graphene on BSTO. (c) Histogram of the phase measurement data. Graphene on BSTO is heavily contaminated after fabrication with a graphene height RMS roughness of 1.82 nm. (d-f) Corresponding images after cleaning in contact mode. The graphene RMS roughness decreases to 0.17 nm and atomic steps become clearly visible in the BSTO film. The phase response changes from a broad distribution to two distinct peaks corresponding to graphene and the BSTO substrate, respectively. The arrows point at the graphene. All scale-bars are 500 nm. The Z-scales in (a) and (d) are both 8 nm. Adapted from paper **V**.

To illustrate the effectiveness of the cleaning method, it is also employed to graphene devices on ferroelectric BSTO/Nb-STO. Contaminants adhere strongly to the surface and are inherently difficult to remove due to the polarization of the ferroelectric film. Figure 5.3 shows height (a), phase (b), and histogram of the phase (c) measurements of graphene on BSTO after processing. It is heavily contaminated with R_{RMS} = 1.82 nm for graphene and R_{RMS} = 1.66 nm for bare BSTO substrate. Mechanical cleaning is able to remove these strongly adhered contaminants and recover atomically smooth graphene. In Figure 5.3(d-f), corresponding images for the same area of graphene on BSTO are shown after cleaning. The graphene becomes atomically flat after cleaning, with clearly visible atomic steps in the BSTO. R_{RMS} reduces to 0.17 nm for graphene and 0.41 nm for BSTO. The phase response transforms from a broad distribution to two distinct peaks. The peaks at roughly -25 ° and +20 °, correspond to graphene and BSTO, respectively.

5.3 Conclusions

Graphene is easily contaminated after nanofabrication processing, which affects its electronic properties. Mechanical cleaning of graphene using AFM is an easy way to obtain clean and atomically flat graphene. It improves the charge neutrality of graphene and, using moderate contact force, increases the mobility. Especially for samples that are incompatible with standard high temperature annealing cleaning processes, this technique appears to be indispensible, as in the case of graphene on BSTO/Nb-STO.

6 Graphene bolometer

Owing to its exotic electronic properties and atomic thickness, graphene has been suggested as sensing material in a large number of applications. One such sensor device is proposed in this chapter: the graphene-based cold-electron bolometer. It is a detector for microwave radiation (paper **VI**). Chapter 6.1 introduces different radiation detectors. Chapter 6.2 describes the device layout and the measurement results. Finally, Chapter 6.3 contains conclusions and outlook.

6.1 Introduction

There exists a range of detectors for high-frequency radiation: Schottky diodes, kinetic inductance detectors [179], transition edge detectors [180], hot-electron bolometers [181], and CEB detectors [82, 182]. The ultimate low volume and hence low electron heat capacity combined with a weak electron-phonon coupling make graphene an interesting material to be used in cryogenic bolometer detectors [183]. In this work, a proof-of-principle graphene-based CEB is demonstrated. The standard Al-based CEB technology is adapted to the use of graphene as detector material and the device is characterized as both temperature sensor and as radiation detector.

6.2 Experiment and results

Fabrication of the graphene-based CEB starts with graphene exfoliated on standard SiO_2/Si chips and identified using optical microscopy. The Si chips used in this project are not highly doped, as is the case for most chips used with graphene. Because of the low doping, they become insulating at cryogenic temperatures. This makes them transparent to microwaves and allows for illumination of the device. Because the Si is insulating, no gate voltage can be applied.

Graphene is patterned into rectangles of $5.5 \times 2.0\ \mu m^2$ using EBL and oxygen plasma. A second lithography step defines two pillars, one on each end of the graphene rectangle. The two pillars consist of Al-based SIN tunnel junctions deposited by thermal evaporation. The schematic of the device is shown in

Figure 6.1(a). First a thin (1.5 nm) layer of Cr is deposited which (partially) oxidizes to form magnetic chromium oxide. This leads to suppression of superconductivity for the first Al layer, which is deposited on top (10 nm). Oxygen is let into the chamber to form a thin insulating layer of Al_2O_3. Finally, a superconducting Al layer (70 nm) is deposited and encapsulated by Pd (5 nm). The graphene bridges the two SIN junctions. In a third lithography step, 80 nm thick Al antenna leads connect to the junctions. An AFM phase image of the final devices is shown in Figure 6.1(b).

Two different cryostats are used for electrical measurements. One is equipped with an optical window to enable optical response measurements at temperatures down to 270 mK. The other is a cryogen-free dilution refrigerator with a base temperature of 50 mK. First, the graphene-based CEB is characterized at the lowest temperatures. Current is measured as a function of voltage for temperatures ranging from 50 mK to 350 mK as shown in Figure 6.2(a). Corresponding dynamical resistance $\partial V / \partial I$ is shown in Figure 6.2(b). For temperatures up to ~300 mK, the I-V

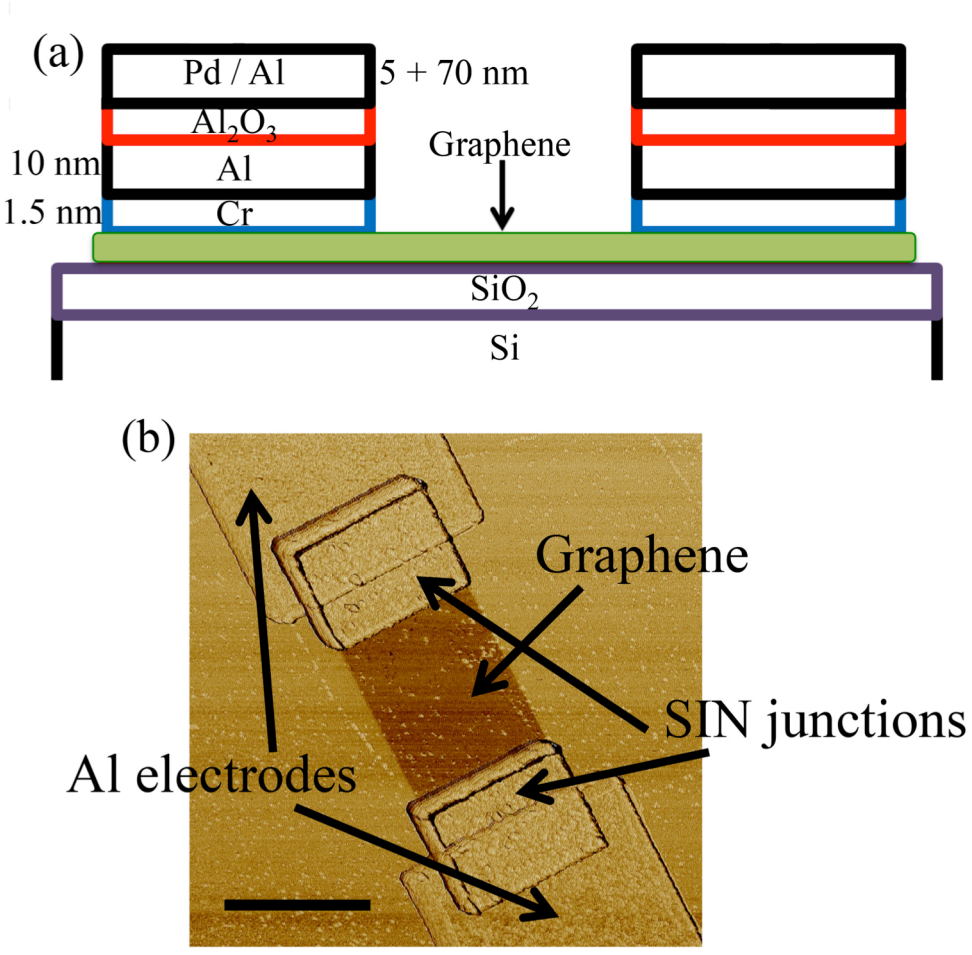

Figure 6.1: (a) Schematic side view of the graphene-based CEB. Graphene is deposited on SiO_2/Si substrates. A heterostructure of Al/Cr, Al_2O_3, and Pd/Al is deposited using thermal evaporation. (b) AFM phase image of the device. The graphene bridges two SIN junctions connected by antenna electrodes. The scale-bar is 2 µm. Adapted from paper **VI**.

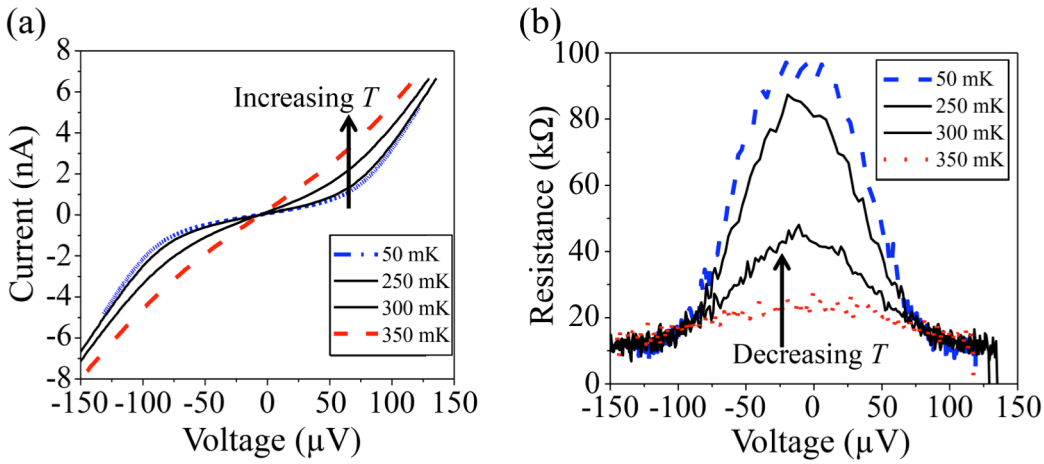

Figure 6.2: (a) Current as a function of voltage for a graphene-based bolometer in the temperature range from 50 mK to 350 mK and corresponding dynamical resistance (b). For temperatures lower than ~250 mK, the non-linear behavior saturates. The ratio between high- and low resistance regimes is ~10. Adapted from paper **VI**.

is non-linear for voltages <150 μV, showing the expected SINIS barrier-like behavior. This is less than double the superconducting gap of Al (~400 μV). The apparent gap is suppressed and smeared possibly due to electrical noise in the measurement setup.

Next, the device is moved to the cryostat equipped with an optical window. Optical response is measured using a 110 GHz source. Figure 6.3(a) shows such measurements performed at 277 mK. The response is clearly visible but it is not normalized to responsivity due to lack of calibration of the microwave intensity. As mentioned previously, it is also possible to use the CEB as a pure thermometer. By measuring current-voltage characteristics for small temperature intervals (temperature as measured by the cryostat thermometer) the temperature responsivity of the device is obtained. This is shown in Figure 6.3(b). The maximum temperature responsivity of ~0.4 μV/mK is found around 300 mK.

6.3 Conclusions

A graphene-based CEB with Al SIN tunnel junctions is realized and characterized in two different cryostats. At 277 mK it shows optical response when illuminated with 110 GHz radiation. This demonstrates a first proof-of-principle experiment to investigate the feasibility of using graphene as absorber material in a CEB. Several issues must be addressed in order to optimize the performance. The ratio between low- and high resistive states in the current-voltage characteristics is roughly two orders of magnitude lower than in state of the art devices with other normal metal absorbers. The resistivity of graphene is higher than for most metals. This could be improved by intentional doping of the graphene and by fitting a gate electrode, which is sufficiently transparent to microwaves.

By utilizing a normal metal (Al/Cr) as part of SIN junction, the effective volume of the absorber (graphene plus the bottom layer of the SIN junctions) is greater than the volume of the graphene itself. While it is difficult to quantitatively estimate the effective volume, a CEB without any other normal metal is preferable. Al tunnel junctions can be made directly to graphene, opening up new possibilities of making the ultimate low volume CEB [184].

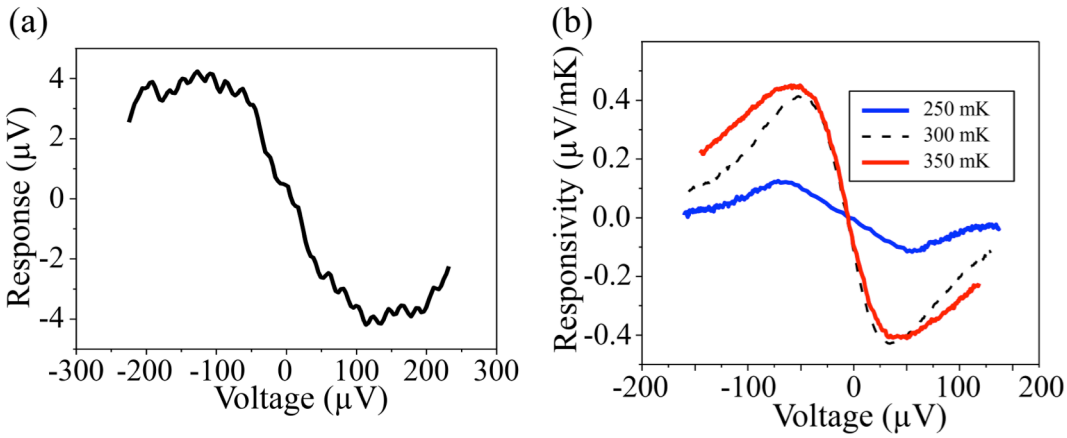

Figure 6.3: (a) Optical response for microwave radiation of frequency 110 GHz obtained at 277 mK. The response is not converted to radiation responsivity due to lack of calibration of the microwave intensity. (b) Temperature responsivity at 250 mK, 300 mK, and 350 mK. The maximum responsivity of ~0.4 μV/mK is obtained at approximately 300 mK. Adapted from paper **VI**.

7 Aharonov-Bohm effect in graphene

The quantum mechanical Aharonov-Bohm effect is studied in exfoliated graphene in this chapter (paper **VII**). In Chapter 7.1, a background to the experiment and the idea of using "mirrors" to enhance the coherence of the system are given. Chapter 7.2 presents the experimental results where indeed the mirrors improve the visibility of Aharonov-Bohm oscillations. Finally, Chapter 7.3 provides conclusions.

7.1 Introduction

Electrons behave according to the laws of quantum mechanics. If they can retain quantum mechanical phase on the length scale of a measured device, they behave coherently and interfere and demonstrate interference effects. One example of such a quantum-mechanical interference phenomena in graphene is the Aharonov-Bohm effect, which was studied previously [185-190]. In these experiments, typically only the first order oscillations are seen. At high magnetic fields, also second order oscillations can be seen but with low visibility.

As described in Chapter 2.5, the visibility of the Aharonov-Bohm effect can be improved by depositing metal mirrors to confine charge carriers to the ring. These mirrors can be made from either normal metals or a superconducting material. In this work, samples with both normal metal (Au, with Ti adhesion layer) and superconducting (Al) mirrors are studied to investigate the effect of superconductivity [191]. Samples are also fabricated without mirrors for comparison. Some of these devices are even fit to the same graphene flake to make all the other parameters as similar as possible.

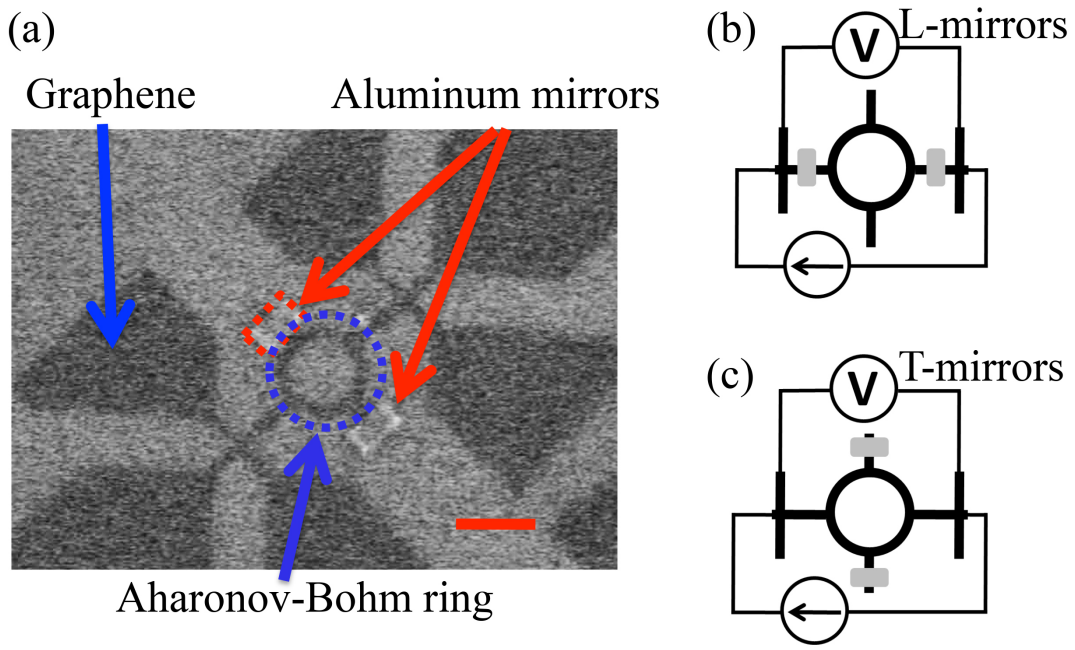

Figure 7.1: (a) SEM image of a graphene Aharonov-Bohm device. The blue, dotted circle outlines the graphene ring. The width of the graphene current path is 150 nm and the ring diameter is 1 µm. Aluminum mirrors are deposited on the perimeter of the ring as indicated by the red arrows. The scale-bar is 1 µm. (b) and (c) Illustrations of longitudinal- (L) and transverse (T) mirror configurations, respectively. Adapted from original in paper **VII.**

7.2 Experiment and results

Not only the mirror material is considered, but also their placement plays an important role. Hence, devices are prepared with no mirrors, mirrors in the transverse direction- (T-mirrors), or mirrors in the longitudinal direction (L-mirrors) of the current path. Figure 7.1(a) shows a SEM micrograph of a device with Al mirrors in the T-mirror configuration. The darker areas pointed out by blue arrows are graphene. The width of the current path is 150 nm and the ring diameter is 1.0 µm. In Figure 7.1(b) and (c), L- and T-mirror configurations are shown, respectively.

Since the width of the current path is not negligible compared to the ring diameter, both the inner- and outer ring diameter must be considered when estimating the excepted periodicity of Aharonov-Bohm oscillations from equation (2.12). A thinner current path would give a better-defined periodicity, but also stronger contributions from UCFs. For the geometry given, first order Aharonov-Bohm oscillations have the theoretical range of 140-250 1/T.

Samples are placed in a dilution refrigerator with a base temperature of 20 mK. Resistance is measured as a function of the magnetic field for a set of temperatures ranging from 20 mK to 1590 mK. It was measured using a low-frequency lock-in technique with three different currents: 0.5, 5, and 50 nA for optimizing the current-

to-noise ratio. Magnetic fields up to a few tesla are applied. For such a narrow graphene channel at low temperature, UCFs are dominant and no IQHE is seen in this regime.

The Dirac voltage of these devices is typically at plus few tens of volts, indicating strong p-type doping. Hence, the graphene charge carrier concentration is high at $V_g = 0$.

Figure 7.2(a) shows a typical measurement of resistance as a function of magnetic field for a sample with L-mirrors made of Al at 17 mK. On top of large UCFs, a small periodic signal is seen. To distinguish between the aperiodic UCFs and the periodic Aharonov-Bohm oscillations, FFT is performed. A running average filter is utilized and the slowly varying part of the magnetoresistance is removed prior to FFT to enhance visibility of oscillations. The averaging window is chosen to be 5 mT giving the best result. To make sure this filtering induced no artifacts, different values for the averaging window were tried, yielding a similar result.

Figure 7.2(b) and (c) show FFT data for samples with Al T-mirrors and L-mirrors, respectively. The dashed lines indicate expected theoretical values for the periodicity. For both types of samples, first order oscillations (h/e) are clearly visible. For T-mirror samples, only a weak second order signal ($h/2e$) is observed, indicating limited coherence of the system. For L-mirror samples on the other hand, both first- and second order signals are clearly visible. Even third order oscillations ($h/3e$) can be seen, proving significantly improved coherence.

The phase coherence length L_φ of the system is estimated independently from both weak localization and the Einstein relation to be ~1-2 μm, which is comparable to the diameter of the ring.

The third order oscillations were not seen in previous graphene Aharonov-Bohm experiments. Also, even second order oscillations were only seen at high magnetic fields (≈ 4 T). In our experiments we observe higher order peaks at both low and high magnetic fields. To explain this we consider two important differences in our experiment compared to previous graphene Aharonov-Bohm measurements. First, we deposit metal mirrors that are expected to improve coherence by confining charge carriers to the ring. We can see a clear difference in the visibility of Aharonov-Bohm oscillations between the two mirror configurations, indicating that they play a major role.

Second, the temperature in our experiment is significantly lower than in others previous. Indeed, by increasing the temperature moderately to 78 mK, the peak corresponding to third order oscillations disappears while the second order signal turns weak, even for a sample with L-mirrors. FFT data for a L-mirror sample at temperatures from 17 mK to 1590 mK are shown in Figure 7.3. At the lowest temperature, up to third order signals are visible. At elevated temperature, the peak

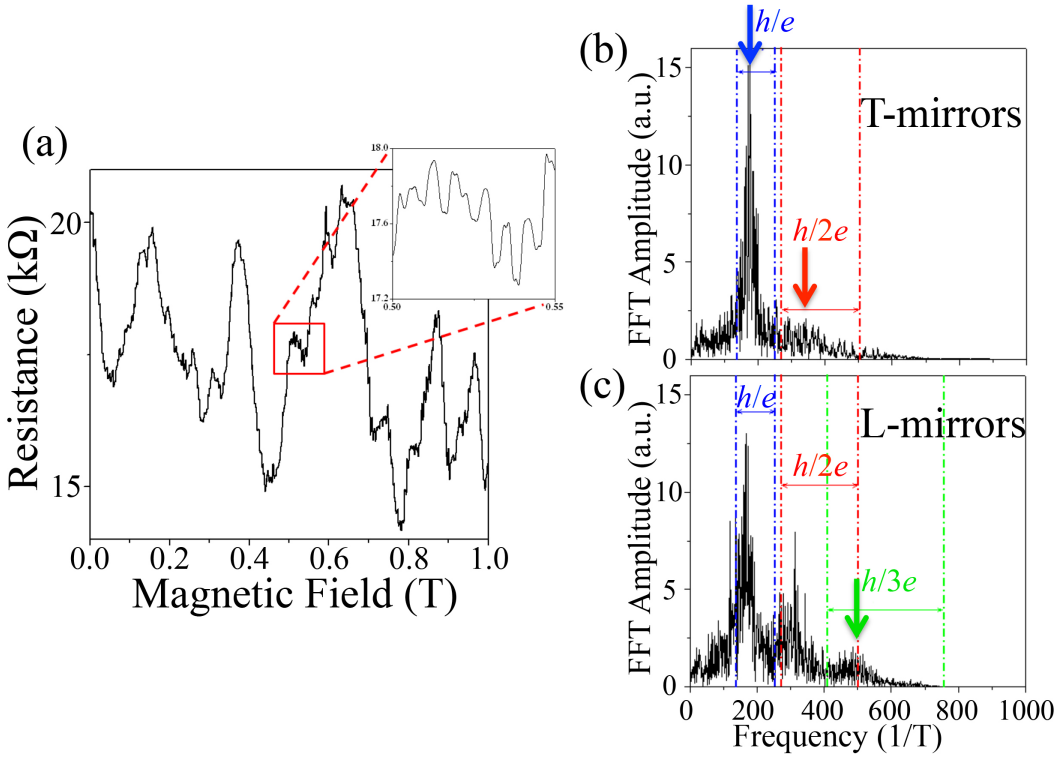

Figure 7.2: (a) Resistance as a function of magnetic field for a sample with L-mirrors measured at 17 mK. Small, periodic oscillations are seen on top of the larger aperiodic UCFs. The inset shows a zoom-in to further visualize the periodic oscillations. (b) and (c) FFT spectra after filtering for T- and L-mirror samples, respectively. The dashed lines correspond to theoretical values for the first (blue), second (red), and third (green) order oscillations determined from the inner- and outer diameters of the ring. The arrows point at the peak positions. Adapted from original in paper **VII.**

corresponding to third order oscillations vanishes and at the highest measured temperature only a weak first order signal is observed.

It should be noted that samples have so far been fabricated using different graphene flakes for each sample. Also, the mirrors have all been made from Al. To study the effects of the mirrors more accurately, samples with and without mirrors fabricated on the same graphene flake are studied. Some samples still have Al mirrors and some instead have Au/Ti mirrors. Sadly, these samples turned out to be of lower graphene quality than the previous ones (in terms of mobility, phase coherence, and charge neutrality) and the third order oscillations were not observed. However, a significant improvement of the first order signal is observed when L-mirrors were present. This is true for samples with both Al and Au/Ti mirrors. For samples with T-mirrors, however, no improvement is seen independent of mirror material.

The enhanced visibility of Aharonov-Bohm oscillations for samples with Al L-mirrors is observed also at magnetic fields exceeding 1 T (not shown in this thesis), where the mirrors are surely non-superconducting. Combined with the fact that Al- and Au/Ti mirrors give similar improvement of oscillation visibility it can be concluded that superconductivity does not play an important role in improving

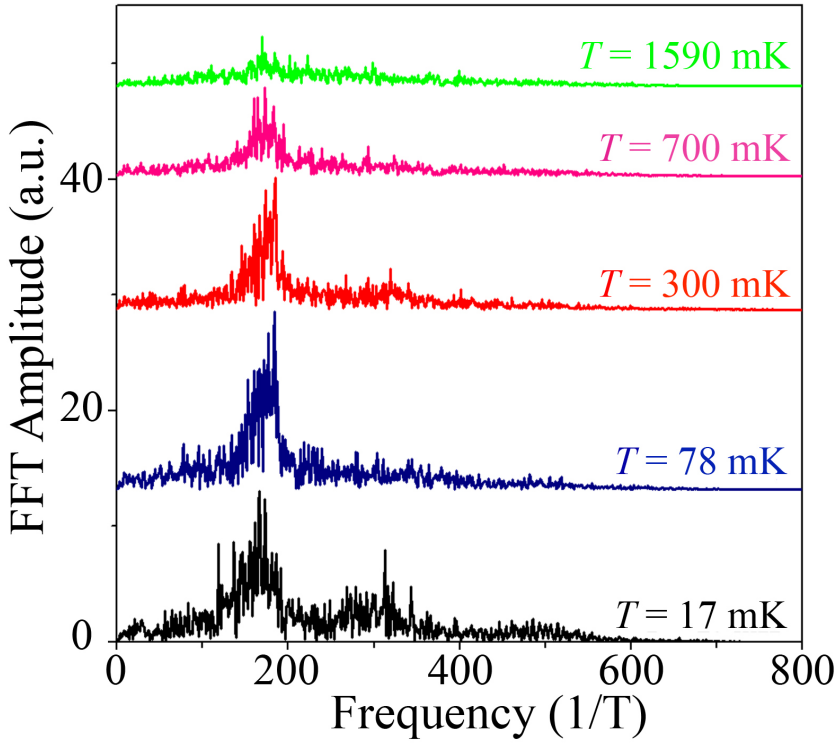

Figure 7.3: Temperature dependence of FFT spectrum for a graphene Aharonov-Bohm device with L-mirror configuration. At the base temperature of 17 mK, first-, second-, and third order Aharonov-Bohm oscillations are observed. Already at 78 mK, the second order oscillations are difficult to see. At the highest measured temperature of 1590 mK, only a weak first order signal is observed. Curves are shifted along the ordinate for clarity. Adapted from original in paper **VII**.

visibility of Aharonov-Bohm oscillations in these graphene samples.

7.3 Conclusions

It is possible to increase the visibility of Aharonov-Bohm oscillations in graphene nanorings by depositing metal mirrors in the current path. These can be either metallic or superconducting and serve the purpose of confining charge carriers to the ring. A strong increase in the visibility of higher order signals is observed in samples with mirrors in the current path. For samples with mirrors in the transverse direction no improvement is observed. For L-mirror samples, up to third order oscillations are observed at the base temperature of 17 mK.

The mirrors were all placed symmetrically either along or transverse the current path. It could be interesting to see what difference it would make to place only one mirror instead. In this case, it would be possible to investigate the importance of each (either entry or exit) mirror by comparing results for different signs of the current bias.

There was no way in this measurement setup to directly probe the superconductivity of the Al mirrors. There are, however, signs of SINIS behavior looking at the I-Vs of graphene devices with Al mirrors (data is available in paper **VII**). Close to the Dirac point the samples show Coulomb blockade. Graphene hence can be considered the insulating part of the SINIS structure. It is an indication of superconductivity in the system.

8 Weak localization in inhomogeneous magnetic fields

In this chapter, WL in inhomogeneous magnetic fields is studied for graphene (paper **VIII**). Chapter 8.1 gives an introduction to WL in graphene and the idea behind the experiment. In Chapter 8.2, the experiment is described in detail and the results are presented. Chapter 8.3 provides conclusions.

8.1 Introduction

WL is another quantum mechanical effect that can be used to study the electronic properties of graphene [68, 69, 71]. Particularly, the inelastic and elastic scattering lengths can be assessed as described in Chapter 2.6. The effect is visible at low temperature and for low magnetic fields (typically less than 1 T). The previous WL experiments on graphene consider homogeneous magnetic fields. In this work instead, graphene WL in inhomogeneous magnetic fields is studied. The effect of inhomogeneous magnetic fields on WL has been studied for other 2DEGs [74-77]. The ultimate two-dimensionality of graphene and the possibility to tune L_φ makes graphene an interesting candidate for similar studies.

The inhomogeneous magnetic field is generated by placing a type-II superconductor, in this case Nb, in proximity to graphene. To directly compare inhomogeneous and homogeneous WL in graphene, regions of graphene both with- and without proximity Nb are fabricated on the same chip.

8.2 Experiments and results

Graphene grown on Cu using CVD was chosen for studying WL, mainly for two reasons. First, it provides large enough area of material so that both Nb-covered- and free regions in the same, continuous piece of graphene can be studied. Hence, the current path can be made wide enough to minimize the effects of UCFs and significantly wider than the average spacing between vortices. Second, CVD-grown

graphene has phase coherence lengths in the order of a few hundred nm, with corresponding characteristic magnetic fields of a few mT. In contrast, exfoliated graphene of high quality can have $L_\varphi > 1$ µm corresponding to $B_\varphi < 1$ mT, which makes magnetotransport measurements challenging.

The graphene is transferred to SiO_2/Si substrates and patterned with EBL and oxygen plasma. Au (80 nm)/Ti (3 nm) metal electrodes are deposited using EBL and electron beam evaporation. The entire sample is coated with 30 nm thick Al_2O_3 using atomic layer deposition (ALD) following a nucleation step where 2 nm Al is evaporated and subsequently oxidized for 5 min at 200 °C in air. Nb is deposited using sputtering followed by the evaporation of Au (50 nm)/Ti (3 nm) to facilitate wire bonding. In a final EBL step, argon ion- and NF_3 reactive-ion are used to remove selective areas of the Au/Nb layer. A schematic of the sample design, with one Nb-covered and two free areas of graphene, is shown in Figure 8.1(a). A magnetic field is applied perpendicular to the sample. The magnetic field penetrates the type-II superconducting Nb film in the form of Abrikosov vortices [81]. This leads to an inhomogeneous magnetic field also penetrating the Nb-covered graphene, which is separated from Nb by only 30 nm. An optical micrograph of the final structure is shown in Figure 8.1(b). The effective area of graphene probed in electrical measurements is $W \times L = 8 \times 32$ µm^2.

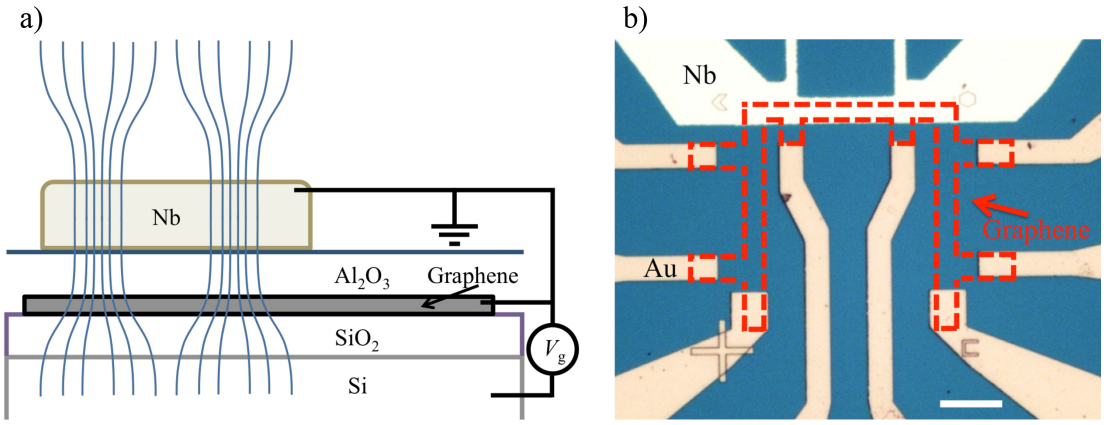

Figure 8.1: (a) Schematic side view of the sample layout. CVD-grown graphene on SiO_2/Si substrates is patterned using oxygen plasma and metal electrodes are deposited. The entire structure is covered with Al_2O_3. Selected areas are covered with Nb using sputtering and reactive ion etching. (b) Top view optical micrograph. Graphene is outlined by dashed red lines. Current is injected using the two bottom corner electrodes. Separate voltage probes are used to independently measure the resistance of both Nb-covered- and free graphene regions (one to the left- and one to the right of the Nb-covered area). The scale-bar is 20 µm. The graphene channel width is 8 µm and the distance between voltage probes is 32 µm. Adapted from original in paper **VIII**.

The resistance of Nb-covered- and free graphene is recorded independently using four-probe lock-in measurements at 4 K. A certain increase of magnetic field is needed for the vortices to move. This is due to strong vortex pinning due to defects in the Nb film. The vortices move in the form of vortex avalanches, which have been studied using various methods [192, 193]. Such collective motion leads to a step-wise change in the effective magnetic field in close proximity to the superconductor. The magnetoresistance of graphene can be used to study such vortex motion, and measurements of this phenomenon are presented in the end of this chapter [76]. However, for studying weak localization, vortex avalanches must be avoided. Both the effect of vortex avalanches and the screening of the magnetic field due to the Meissner effect can be avoided by using a field-cool measurement technique previously described in literature [75, 76]. The sample is first heated to >10 K, which is higher than T_c, the critical temperature of Nb thin films used in this experiment, $8\ \mathrm{K} < T_c < 9\ \mathrm{K}$. The magnetic field is set at this elevated temperature. Then, the sample is cooled to base temperature (field-cooled) and the resistance is recorded. Both Nb-covered- and free graphene are measured using field cooling for comparison, even though it is only necessary for the former. A heater situated close to the sample, in addition to the small thermal mass of the sample holder, makes it possible to relatively fast cycle temperature between 4 K and 10 K. Despite this, such a measurement is still very time consuming and is typically performed over night.

A field-cool measurement for Nb-covered graphene with an applied back-gate voltage of $V_g = -20$ V averaged over four magnetic field sweeps is shown in Figure 8.2(a). The graphene is intrinsically n-doped after fabrication and remains n-doped for the full range of gate voltages applied. For $|B| > 3$ mT it can be well described using the ordinary graphene WL model and equation (2.13). The extracted fitting parameters are $B_\varphi = 2.6$ mT ($L_\varphi = 250$ nm) for inelastic scattering, and the two elastic scattering terms $B_i = 200$ mT ($L_i = 29$ nm) and $B_* = 500$ mT ($L_* = 18$ nm). It is difficult to obtain accurate values for B_i and B_* due to the degree the two are mathematically convoluted in equation (2.13) [71]. However, it is clear for all samples measured that elastic scattering dominates (shorter scattering length) over inelastic scattering.

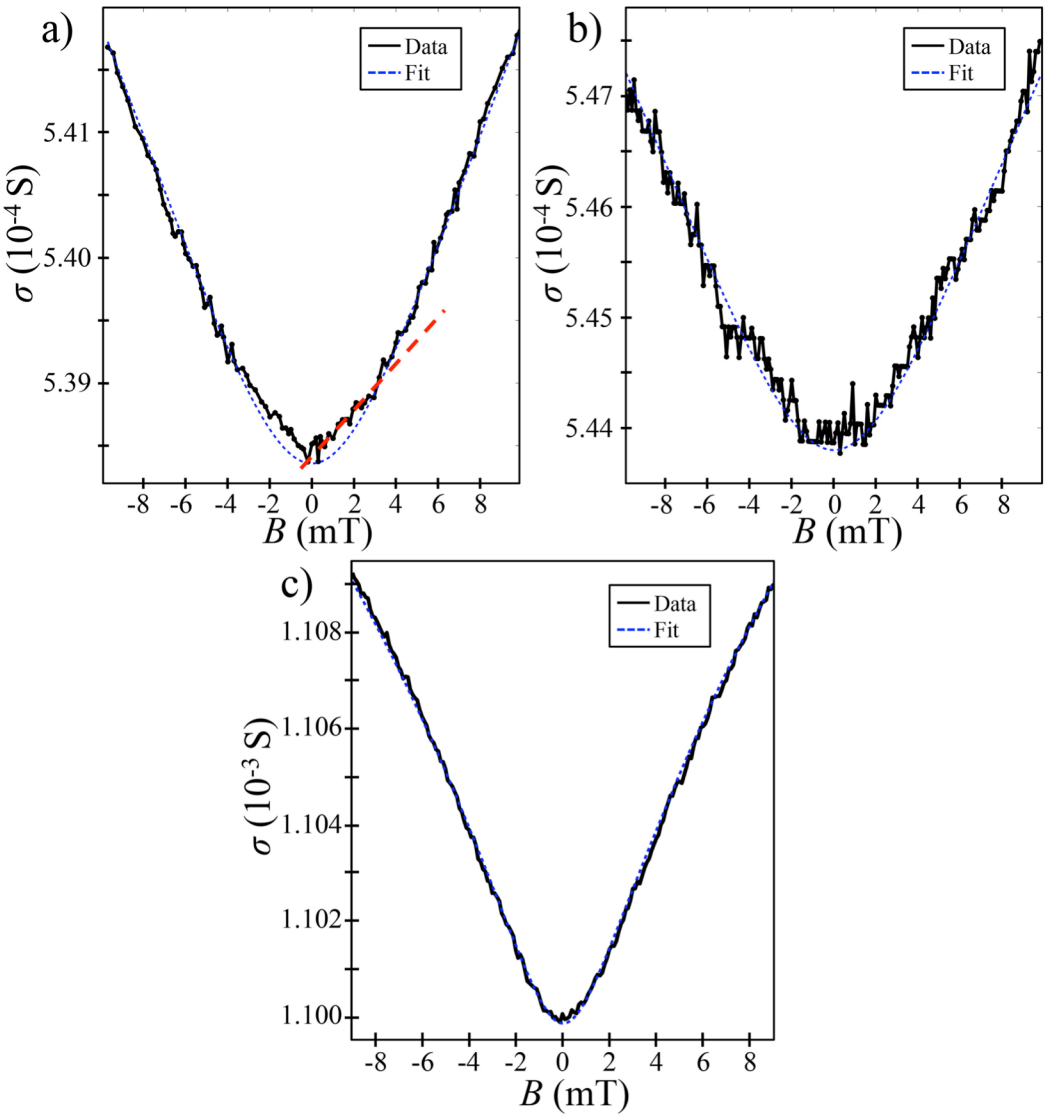

Figure 8.2: (a) Field-cool conductivity measurement of Nb-covered graphene with V_g = -20 V (solid black line). For $|B| < 3$ mT, a deviation from ordinary graphene WL behavior, fit using equation (2.13) (blue dashed line), is observed. A straight line is added for comparison (red dashed line) (b) Similar measurement for free graphene with comparable resistivity and extracted scattering lengths (solid black line). It can be well described by equation (2.13) (blue dashed line). (c) Similar measurement for free graphene (taken for the other side of the graphene structure), but for graphene with higher conductivity and longer L_φ. Adapted from original in paper **VIII**.

For $|B| < 3$ mT, a deviation from the quadratic low-field behavior, expected for graphene in homogeneous magnetic fields, is observed. The effect is too weak for quantitative analysis using equation (2.14). The magnetic field range where the data deviates from the fit using equation (2.13) corresponds roughly to B_φ. Similar measurements for free graphene (no Nb in close proximity) are shown in Figure 8.2(b) (left-side free graphene) and (c) (right-side free graphene). While field

cooling is not necessary in this case, it is still measured the same way for comparison. There is no observable deviation from the normal graphene WL theory. The left- and right-side free graphene yield $B_\varphi = 2.8$ mT ($L_\varphi = 240$ nm) and $B_\varphi = 0.9$ mT ($L_\varphi = 420$ nm), respectively. Hence, the measurement presented in Figure 8.2(b) provides the most direct comparison with the data for the Nb-covered sample. It is slightly noisier due to less averaging than for those in Figure 8.2(a) and (c).

Graphene offers the possibility to tune L_φ by tuning the carrier concentration using a gate electrode. Measurements of Nb-covered graphene for four different gate voltages are shown in Figure 8.3. Since the sample is n-doped, an increased gate voltage leads to an increased charge carrier density and a larger L_φ. By changing the gate voltage from -20 V to +15 V, L_φ increases from 250 nm to 320 nm (B_φ decreases from 2.6 mT to 1.6 mT). The deviation from normal WL behavior becomes less pronounced with increasing L_φ.

Finally, Figure 8.4 shows WL resistivity for a sample with graphene in close proximity to an unpatterned Nb film, covering the entire substrate, in the absence of field-cool measurements. Instead, the magnetic field is directly swept at 4 K. The

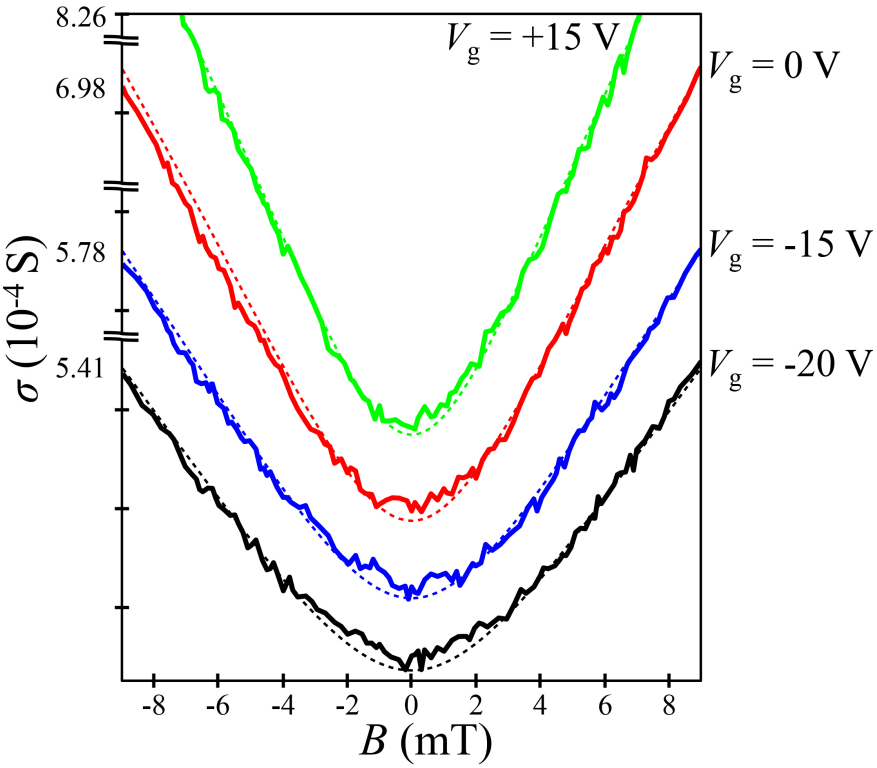

Figure 8.3: Conductivity as a function of magnetic field for Nb-covered graphene for four different gate voltages. As the gate voltage is increased from -20 V to +15 V, the carrier concentration is increased and so is L_φ. The low-field discrepancy becomes less pronounced for increased L_φ. Adapted from original in paper **VIII**.

resistance changes stepwise, where each step is attributed to a vortex avalanche event. The steps are always present at low temperature but their exact positions vary.

8.3 Conclusions

A deviation from the normal graphene WL theory is observed for Nb-covered graphene when measured using the field-cooling technique. The deviation is attributed to the inhomogeneous field induced by proximity to the superconducting thin film. The effect is weak, but observable. Quantitative comparisons could not be made with theories on inhomogeneous WL. Tuning the carrier concentration, and hence the phase coherence length, changes the low-field WL behavior.

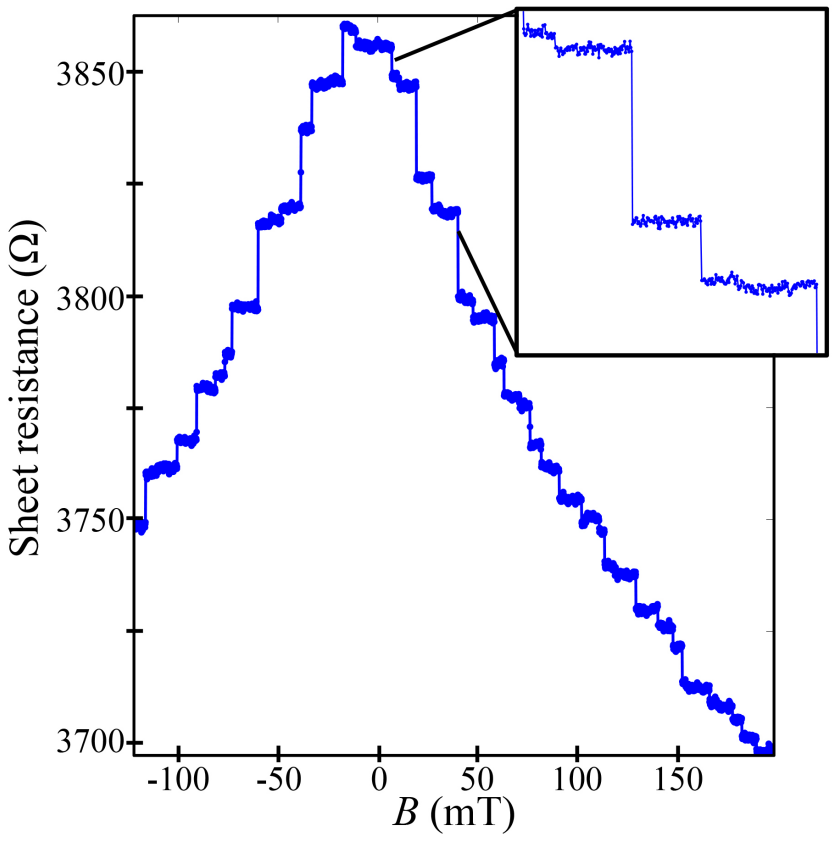

Figure 8.4: Nb-covered graphene WL resistivity in the absence of field cooling. The stepwise changes of resistivity are attributed to vortex avalanches. The inset shows a zoom-in on some of the resistance steps. Adapted from original in paper **VIII**.

9 Summary and outlook

Graphene is an enticing material with all its superlative attributes and possible usage in applications. At first sight, it really appears to be a super material and in a scientific sense it could be argued that so is the case. It is important to note, however, that several challenges remain for graphene to be successful in commercial applications. One such challenge is opening a band gap in graphene while maintaining high mobility. Another challenge is large-scale graphene fabrication, one of the two main focuses of this thesis. As presented in this thesis, it is possible to grow large-area graphene of reasonably high quality ($\mu > 3000$ cm^2/Vs) on Cu using CVD, but achieving homogeneity similar to what can be achieved with traditional semiconductors is so far difficult.

A problematic aspect of graphene fabrication is the transfer of graphene from growth template to the desired target substrate. In this thesis two different techniques were utilized. First, it is possible to chemically etch Cu while a thin polymer is supporting the graphene. This widely used technique is rather reproducible, but leaves lots of residues and the Cu catalyst is consumed in the process. Second, we show that the polymer-protected graphene can instead be delaminated from Cu using hydrogen bubbling. The main advantage for this technology is that the Cu can be reused.

Wet transfer techniques may be acceptable in some manufacturing processes, such as roll-to-roll production of liquid-crystal display (LCD) screens. They are, however, unlikely to be incorporated into any manufacturing based on wafer processing. Also, the use of Cu is not compatible with traditional Si processing due to contamination issues. To avoid the transfer step, the growth of graphene on insulating- and semiconducting substrates was investigated. Such growth is fundamentally different from the catalytic growth on Cu. Graphene grown non-catalytically is nanocrystalline with inferior electronic properties ($\mu \sim$ a few tens of cm^2/Vs). The growth is not self-limiting, but the number of graphene layers can be controlled by the process parameters. Hence, both the electrical conductivity and the optical transmittance of the resulting graphene can be tuned. It has been shown that graphene grown non-catalytically at higher temperature (~1600 °C, as compared to

~1000 °C used in this work) can exhibit significantly higher mobility, rendering hope for high-quality graphene growth on insulators [123].

Graphene devices suffer from a variety of contaminants from microfabrication processing, in particular polymer residues. The mechanical cleaning method presented here can render graphene atomically smooth after processing. In contrast to standard annealing cleaning methods, it can be used for cleaning graphene devices on substrates that are not high-temperature compatible in Ar/H_2 atmosphere, such as BSTO/Nb-STO. A major challenge is scaling up from cleaning single devices to wafer-scale cleaning.

The second part of this thesis concerns experiments combining graphene with superconductors. A graphene-based CEB was realized, where graphene was used as the normal metal absorber. The atomic thickness of graphene makes for a detector with extremely small volume. It shows optical response at 110 GHz and a temperature responsivity of ~0.4 μV/mK around 300 mK. Further device optimization, especially in terms of impedance matching and improving the ratio between low- and high resistive states, is needed to assess the prospects of this technology.

The quantum mechanical Aharonov-Bohm effect was studied in graphene nanorings. Previously, the visibility of Aharonov-Bohm oscillations in Ag was improved by applying superconducting Al strips close to the ring due to a phase memory effect. When applying Al strips close to the graphene nanoring, indeed a significant improvement of the oscillations is seen. With L-mirrors up to third order oscillations are observed. The improvement is, however, not observed for samples with T-mirrors, in contrast with previous experiments on Ag. In addition, the same behavior is observed for samples with mirrors made from normal metal Au instead of superconducting Al, ruling out the phase memory effect as the main reason for the increased visibility in our case. Instead, it is explained by confinement of charge carriers to the nanoring due to the Fermi velocity mismatch between graphene and the metal mirrors.

Weak localization, another quantum mechanical effect, was studied for graphene in inhomogeneous magnetic fields. A type-II superconducting Nb thin film was put in close proximity to graphene in order to generate the inhomogeneous field. A small, but detectable, deviation from the standard weak localization behavior for graphene was observed for small fields ($|B| < 3$ mT). Since the effect is small, it is difficult to quantify and to compare with previous measurements on semiconducting 2DEGs. Better sample uniformity may increase the visibility of the effect.

Graphene is still a young material and it remains unclear which applications it may be used in. Maybe its greatest impact will come from opening up the world to other 2D materials, a world that we have only scratched the surface of so far.

Appendix A: Recipes for sample fabrication

Graphene exfoliation

Producing graphene using mechanical exfoliation is part skill and part luck. By proper choices of materials and techniques the production of 20-40 μm monolayer flakes can be reasonably reproducible.

The following parameters (among others) were more or less systematically studied to assess their effect on the yield of monolayer flakes, and their cleanliness, when exfoliating on SiO_2/Si substrates:

- the graphite source material (highly ordered pyrolytic graphite (HOPG), natural graphite, or industrial-grade graphite),
- pre-patterning of the graphite using optical lithography and O_2 plasma,
- the tape used (blue Nitto Denko tape, semi-transparent office tape, thermal release tape, or kapton tape),
- the number of cleavages of the graphite,
- the use of fresh- or reused tape (tape with graphite that has already been used),
- optical inspection of the as-cleaved graphite on the tape to chose specific regions,
- substrate surface treatment (with or without O_2 plasma cleaning, 120 °C annealing in air, or 400 °C in Ar/H_2 atmosphere),
- the temperature of the substrate when the final exfoliation is performed (room temperature, or 120 °C),
- what tool, time and force is used when pushing the graphite/tape towards the substrate,
- and how quickly and at what angle the tape is removed from the substrate.

There is a large contribution of randomness in the yield of monolayer graphene flakes, but at least four parameters were found to play a role: the choice of graphite source material, pre-patterning of that graphite, the choice of tape, and optical

inspection of the as-cleaved graphite on tape. There is not enough statistics to rule out any of the other parameters, but at least these four were found to be of relevance.

Different graphite sources yield different results. HOPG gives a relatively large fraction of monolayer areas with little visible contamination. Sadly, the larger monolayers are rarely freestanding but instead most often attached to various regions of thicker graphite. Commercial-grade graphite also gives a decent fraction of monolayer flakes that are more likely to be freestanding. However, there are visible contaminants on the as-produced graphene flakes and devices made from such graphite show significantly higher doping. The best result is obtained for natural graphite ("graphenium flakes" from NGS Naturgraphit GmbH), which gives the highest yield of freestanding monolayer graphene without visible contamination. Also, devices made from such graphene shows the lowest doping after fabrication. Hence, it is the graphite used in this work.

The yield of large monolayers increases by first pre-patterning the graphite using optical lithography and O_2 plasma (five minutes etching at 100 W). The pattern consisted of squares of different sizes. Despite that this technique improves the exfoliation result, it was not used for the samples in this thesis in order to avoid the risk of doping graphene due to interaction with photoresists.

Essentially any kind of tape can be used to exfoliate graphene. Generally, using a stickier tape gives larger monolayer flakes, but also more contamination. In this work, low levels of contamination are a higher priority than large flake sizes and the not very sticky blue Nitto Denko tape is used.

Optical inspection of the first exfoliation is probably the most important non-material related technique to improve monolayer yield. Ideally, the graphite piece exfoliated on the tape should as thin as possible, shiny, uniform, and continuous.

A typical procedure to produce graphene by mechanical exfoliation is:

- Clean the SiO_2/Si substrates in an acetone ultrasonic bath (high power, 5 min), then put them in isopropanol and finally blow dry using N_2. Then, clean in O_2 plasma (100 W, 3 min). Finally, anneal in Ar/H_2 atmosphere at 400 °C for 60 min.
- Put a piece of natural graphite on a piece of pre-cut Nitto Denko tape that is ~2 mm larger than the graphite flake. Push the graphite firmly with your finger (using gloves) to make sure it is in close contact with the tape. Remove the bulk of graphite using sharp tweezers.
- Inspect the graphite as described previously. If it does not look thin and uniform, restart the procedure.
- Cut an approximately 100 × 100 mm^2 piece of tape and put it on a table, sticky side up. Push the small piece of tape, graphite side down, towards the large

sheet of tape. Make sure they are in close contact by pushing it down with your finger. Exfoliate slowly, ~5 s.

- Repeat the previous step 5-15 times, each time on a fresh area of the tape. The thickness of the graphite after the first exfoliation on the small piece of tape decides how many exfoliations are needed. The thinner the flake, the fewer exfoliations. There should be barely visible pieces of graphite left on the large piece of tape after the last exfoliation when enough many iterations have been made.
- Finally, push the small piece of tape towards a SiO_2/Si substrate, graphite side down, push in firm contact using your finger, and exfoliate slowly, ~5 s.

Then find the monolayer regions using an optical microscope.

EBL graphene etch recipe

The most straightforward way to etch graphene is by oxygen plasma etching. While all resists leave residues that affect the properties of graphene, e-beam ones (PMMA, ZEP) seem to cause less doping than photolithography ones (S1813, AZ). A standard EBL etching recipe using ZEP resist is as follows:

- Substrate cleaning, first in acetone (1 min), then isopropanol (1 min), and finally N_2 blow dry.
- Spin coat ZEP520A:anisole 1:1, 4 krpm, 1 min.
- Soft bake of resist, 5 min at 160 °C on a hot plate.
- EBL exposure, 100 kV, 300 $\mu C/cm^2$.
- Develop in o-xylene 60 s, rinse in isopropanol (30 s), and N_2 blow dry.
- Etch in oxygen plasma, 10 s at 50 W (using a Plasma Therm BatchTop PE/RIE m/95). 10 s is enough to etch few-layer-thick pieces of graphite but most graphite pieces from mechanical exfoliation will remain. Hence, it is important to adjust both the etch- and electrode patterns to avoid short-circuits.
- Remove all resist in 1165 remover and clean in acetone (~10 min), rinse in isopropanol (30 s) and N_2 blow dry.

EBL lift-off recipe

There are many options on how to define electrodes to graphene. This is a standard recipe, which works for many purposes:

- Substrate cleaning, first in acetone (1 min), then isopropanol (1 min), and finally N_2 blow dry.

- Spin coat copolymer (EL10), 4 krpm, 1 min.
- Soft bake of resist, 5 min at 160 °C on a hot plate.
- Spin coat PMMA (A2), 4 krpm, 1 min.
- Soft bake of resist, 5 min at 160 °C on a hot plate.
- EBL exposure, 100 kV, 300 $\mu C/cm^2$.
- Develop in isobutyl ketone:isopropanol 1:1 90 s, rinse in isopropanol (30 s), and N_2 blow dry.
- Metal deposition. A common choice of materials for electrodes is Au (80 nm)/Ti (3nm) deposited by electron beam evaporation. This recipe has proven to work for 200+ nm thick films.
- Lift-off is performed in hot acetone (~50 °C, just under the boiling point), then rinse in isopropanol, and finally N_2 blow dry.

Acknowledgements

First I want to thank my supervisor August Yurgens for guiding me through the world of Science and in particular the world of graphene. Always full of ideas and new experiments! Thanks for always taking your time to help and to discuss all my questions.

I am very fortunate to have had the possibility to work together with my co-supervisor Jie Sun. So many interesting discussions about almost everything in life!

I want to thank my other co-supervisor Dag Winkler and my examiner Mikael Fogelström for their advice regarding how to work in research.

Thanks Youngwoo Nam for all the nice hours spent in different labs and thanks a lot for showing me Korea, an experience I will never forget!

Grigory, thanks for all the interesting discussions and the creative time spent together in the cleanroom.

I want to thank the great master students I have had the privilege to work together with: Abhay, Kishan, Galib, César, and Alex!

Thank you Niklas Lindahl and Johannes Svensson for interesting collaborations. Both of you share a remarkable enthusiasm for Physics!

I am very grateful for the help from Tim Booth and Peter Bøggild from DTU, and from Olof Bäcke, Markus Löffler, and Eva Olsson from Chalmers, regarding TEM analysis.

Alexey Kalabukhov, thanks for all your advice, teaching, patience, and never-matched working pace. I learned a lot (but could never keep up)!

I want to thank Mikhail Tarasov, Sumedh Mahashabde, and Leonid Kuzmin for interesting collaborations regarding bolometers.

Thank you Omid for all discussions and exchange of processing knowledge!

Thanks to my office mate Riccardo, for creating an awesome working environment! Food and Science, in perfect harmony.

I am very grateful to Susannah, Marie, Debora, and Ann-Marie for the administrative support as well as to Lars and Staffan who create wonders in the machine shop.

Thanks to all the cleanroom staff for the process support and training, wonders are created there too!

I want to give a special thanks to Samuel, for always being there to help with all possible matters!

I thank Philip, André, Sophie, Reza, Andreas (Saffran), Michaël, Arsalan, Simon, Marco, Pier Paolo, Io-Chun, Sebastian, Saroj, Tom, Thomas, Shahid, Mengyue, Zhaoyao, Lihui, Justin, Arseniy, Edoardo, Luca, Minshu, Ida-Maria, Maria, Astghik, David, Thilo, Jonas, Floriana, Sergey, Per, and all other past and present QDP staff who make this such an inspiring place to work at!

Finally, I would like to thank my friends and family, especially my mother and my brother, for their support over the years!

Most importantly, thank you Carro! For everything.

Bibliography

[1] K. S. Novoselov, D. Jiang, F. Schedin, T. J. Booth, V. V. Khotkevich, S. V. Morozov, and A. K. Geim, "Two-dimensional atomic crystals", PNAS vol. **102**, pp 10451-10453, 2005.

[2] K. S. Novoselov, A. K. Geim, S. V. Morozov, D. Jiang, Y. Zhang, S. V. Dubonos, I. V. Grigorieva, and A. A. Firsov, "Electric field effect in atomically thin carbon films", Science vol. **306**, pp 666-669, 2004.

[3] G. Ruess, and F. Vogt, "Höchstlamellarer Kohlenstoff Aus Graphitoxyhydroxyd - Über Den Ort Der Aktiven Eigenschaften Am Kohlenstoffkristall", Monatsh. Chem. vol. **78**, pp 222-242, 1948.

[4] H. P. Boehm, A. Clauss, G. O. Fischer, and U. Hofmann, "Das Adsorptionsverhalten Sehr Dunner Kohlenstoff-Folien", Z. Anorg. Allg. Chem. vol. **316**, pp 119-127, 1962.

[5] S. Horiuchi, T. Gotou, M. Fujiwara, T. Asaka, T. Yokosawa, and Y. Matsui, "Single graphene sheet detected in a carbon nanofilm", Appl. Phys. Lett. vol. **84**, pp 2403-2405, 2004.

[6] A. J. Van Bommel, J. E. Crombeen, and A. Van Tooren, "LEED and Auger electron observations of the SiC(0001) surface", Surf. Sci. vol. **48**, pp 463-472, 1975.

[7] R. Rosei, M. De Crescenzi, F. Sette, C. Quaresima, A. Savoia, and P. Perfetti, "Structure of graphitic carbon on Ni(111): A surface extended-energy-loss fine-structure study", Phys. Rev. B vol. **28**, pp 1161-1164, 1983.

[8] Y. B. Zhang, Y. W. Tan, H. L. Stormer, and P. Kim, "Experimental observation of the quantum Hall effect and Berry's phase in graphene", Nature vol. **438**, pp 201-204, 2005.

[9] X. S. Li, W. W. Cai, J. H. An, S. Kim, J. Nah, D. X. Yang, R. Piner, A. Velamakanni, I. Jung, E. Tutuc *et al.*, "Large-area synthesis of high-quality and uniform graphene films on copper foils", Science vol. **324**, pp 1312-1314, 2009.

[10] R. E. Peierls, "Quelques propriétés typiques des corps solides", Ann. I. H. Poincare vol. **5**, pp 177-222, 1935.

[11] L. D. Landau, "Zur Theorie der phasenumwandlungen II", Phys. Z. Sowjetunion vol. **11**, pp 26-35, 1937.

[12] N. D. Mermin, "Crystalline order in two dimensions", Phys. Rev. vol. **176**, pp 250-254, 1968.

[13] A. Barth, and W. Marx, "Graphene - a rising star in view of scientometrics", arXiv:0808.3320v3, 2008.

[14] M. D. Stoller, S. J. Park, Y. W. Zhu, J. H. An, and R. S. Ruoff, "Graphene-based ultracapacitors", Nano Lett. vol. **8**, pp 3498-3502, 2008.

[15] P. L. McEuen, J. S. Bunch, S. S. Verbridge, J. S. Alden, A. M. van der Zande, J. M. Parpia, and H. G. Craighead, "Impermeable atomic membranes from graphene sheets", Nano Lett. vol. **8**, pp 2458-2462, 2008.

[16] C. Lee, X. Wei, J. W. Kysar, and J. Hone, "Measurement of the elastic properties and intrinsic strength of monolayer graphene", Science vol. **321**, pp 385-388, 2008.

[17] A. S. Mayorov, R. V. Gorbachev, S. V. Morozov, L. Britnell, R. Jalil, L. A. Ponomarenko, P. Blake, K. S. Novoselov, K. Watanabe, T. Taniguchi *et al.*, "Micrometer-scale ballistic transport in encapsulated graphene at room temperature", Nano Lett. vol. **11**, pp 2396-2399, 2011.

[18] J. Baringhaus, M. Ruan, F. Edler, A. Tejeda, M. Sicot, I. Taleb, A.-P. Li, Z. Jiang, E. H. Conrad, C. Berger *et al.*, "Exceptional ballistic transport in epitaxial graphene nanoribbons", Nature vol. **506**, pp 349-354, 2014.

[19] A. A. Balandin, S. Ghosh, W. Z. Bao, I. Calizo, D. Teweldebrhan, F. Miao, and C. N. Lau, "Superior thermal conductivity of single-layer graphene", Nano Lett. vol. **8**, pp 902-907, 2008.

[20] R. R. Nair, P. Blake, A. N. Grigorenko, K. S. Novoselov, T. J. Booth, T. Stauber, N. M. R. Peres, and A. K. Geim, "Fine structure constant defines visual transparency of graphene", Science vol. **320**, pp 1308-1308, 2008.

[21] F. Bonaccorso, Z. Sun, T. Hasan, and A. C. Ferrari, "Graphene photonics and optoelectronics", Nature Photon. vol. **4**, pp 611-622, 2010.

[22] M. Liu, X. Yin, and X. Zhang, "Double-layer graphene optical modulator", Nano Lett. vol. **12**, pp 1482-1485, 2012.

[23] A. Tzalenchuk, S. Lara-Avila, A. Kalaboukhov, S. Paolillo, M. Syvajarvi, R. Yakimova, O. Kazakova, T. J. B. M. Janssen, V. Fal'ko, and S. Kubatkin, "Towards a quantum resistance standard based on epitaxial graphene", Nature Nanotech. vol. **5**, pp 186-189, 2010.

[24] X. Huang, X. Qi, F. Boey, and H. Zhang, "Graphene-based composites", Chem. Soc. Rev. vol. **41**, pp 666-686, 2012.

[25] S. Bae, H. Kim, Y. Lee, X. F. Xu, J. S. Park, Y. Zheng, J. Balakrishnan, T. Lei, H. R. Kim, Y. I. Song *et al.*, "Roll-to-roll production of 30-inch graphene films for transparent electrodes", Nature Nanotech. vol. **5**, pp 574-578, 2010.

[26] K. S. Kim, Y. Zhao, H. Jang, S. Y. Lee, J. M. Kim, K. S. Kim, J. H. Ahn, P. Kim, J. Y. Choi, and B. H. Hong, "Large-scale pattern growth of graphene films for stretchable transparent electrodes", Nature vol. **457**, pp 706-710, 2009.

[27] L. G. De Arco, Y. Zhang, C. W. Schlenker, K. Ryu, M. E. Thompson, and C. W. Zhou, "Continuous, highly flexible, and transparent graphene films by chemical vapor deposition for organic photovoltaics", ACS Nano vol. **4**, pp 2865-2873, 2010.

[28] M. C. Lemme, F. H. L. Koppens, A. L. Falk, M. S. Rudner, H. Park, L. S. Levitov, and C. M. Marcus, "Gate-activated photoresponse in a graphene p–n junction", Nano Lett. vol. **11**, pp 4134-4137, 2011.

[29] S. Rumyantsev, G. Liu, M. S. Shur, R. A. Potyrailo, and A. A. Balandin, "Selective gas sensing with a single pristine graphene transistor", Nano Lett. vol. **12**, pp 2294–2298, 2012.

[30] G. Konstantatos, M. Badioli, L. Gaudreau, J. Osmond, M. Bernechea, F. P. G. de Arquer, F. Gatti, and F. H. L. Koppens, "Hybrid graphene-quantum dot phototransistors with ultrahigh gain", Nature Nanotech. vol. **7**, pp 363-368, 2012.

[31] G. E. Moore, "Cramming more components onto integrated circuits", Electronics vol. **38**, 1965.

[32] G. E. Moore, "Progress in digital integrated electronics", IEEE IEDM Tech. Dig. vol. **21**, pp 11-13, 1975.

[33] Y. Q. Wu, Y. M. Lin, A. A. Bol, K. A. Jenkins, F. N. Xia, D. B. Farmer, Y. Zhu, and P. Avouris, "High-frequency, scaled graphene transistors on diamond-like carbon", Nature vol. **472**, pp 74-78, 2011.

[34] L. Liao, J. W. Bai, R. Cheng, Y. C. Lin, S. Jiang, Y. Q. Qu, Y. Huang, and X. F. Duan, "Sub-100 nm channel length graphene transistors", Nano Lett. vol. **10**, pp 3952-3956, 2010.

[35] F. Schwierz, "Graphene transistors", Nature Nanotech. vol. **5**, pp 487-496, 2010.

[36] Y. M. Lin, A. Valdes-Garcia, S. J. Han, D. B. Farmer, I. Meric, Y. N. Sun, Y. Q. Wu, C. Dimitrakopoulos, A. Grill, P. Avouris *et al.*, "Wafer-scale graphene integrated circuit", Science vol. **332**, pp 1294-1297, 2011.

[37] F. Torrisi, T. Hasan, W. Wu, Z. Sun, A. Lombardo, T. S. Kulmala, G.-W. Hsieh, S. Jung, F. Bonaccorso, P. J. Paul *et al.*, "Inkjet-Printed Graphene Electronics", ACS Nano vol. **6**, pp 2992-3006, 2012.

[38] J. Xiao, D. Mei, X. Li, W. Xu, D. Wang, G. L. Graff, W. D. Bennett, Z. Nie, L. V. Saraf, I. A. Aksay *et al.*, "Hierarchically porous graphene as a lithium–air battery electrode", Nano Lett. vol. **11**, pp 5071-5078, 2011.

[39] X. Zhao, C. M. Hayner, M. C. Kung, and H. H. Kung, "In-plane vacancy-enabled high-power Si–graphene composite electrode for lithium-ion batteries", Adv. Energy Mater. vol. **1**, pp 1079-1084, 2011.

[40] P. Matyba, H. Yamaguchi, M. Chhowalla, N. D. Robinson, and L. Edman, "Flexible and metal-free light-emitting electrochemical cells based on graphene and PEDOT-PSS as the electrode materials", ACS Nano vol. **5**, pp 574-580, 2010.

[41] J. Hou, Y. Shao, M. W. Ellis, R. B. Moore, and B. Yi, "Graphene-based electrochemical energy conversion and storage: fuel cells, supercapacitors and lithium ion batteries", Phys. Chem. Chem. Phys. vol. **13**, pp 15384-15402, 2011.

[42] "An analysis of worldwide patent filings relating to graphene", Patent Informatics Team, Intellectual Property Office, Concept House, Cardiff Rd, Newport, South Wales, NP10 8QQ, UK, 2011.

[43] H. Kroemer, "Nano-whatever: Do we really know where we are heading?", Phys. Status Solidi A vol. **202**, pp 957-964, 2005.

[44] R. H. Baughman, A. A. Zakhidov, and W. A. de Heer, "Carbon nanotubes - the route toward applications", Science vol. **297**, pp 787-792, 2002.

[45] Y. Lifshitz, "Diamond-like carbon - present status", Diam. Relat. Mater. vol. **8**, pp 1659-1676, 1999.

[46] H. C. Tsai, and D. B. Bogy, "Characterization of diamond-like carbon-films and their application as overcoats on thin-film media for magnetic recording", J. Vac. Sci. Technol. A vol. **5**, pp 3287-3312, 1987.

[47] A. Schinwald, F. A. Murphy, A. Jones, W. MacNee, and K. Donaldson, "Graphene-based nanoplatelets: A new risk to the respiratory system as a consequence of their unusual aerodynamic properties", ACS Nano vol. **6**, pp 736-746, 2012.

[48] K. Donaldson, and C. A. Poland, "Nanotoxicology new insights into nanotubes", Nature Nanotech. vol. **4**, pp 708-710, 2009.

[49] K. Welsher, S. P. Sherlock, and H. J. Dai, "Deep-tissue anatomical imaging of mice using carbon nanotube fluorophores in the second near-infrared window", PNAS vol. **108**, pp 8943-8948, 2011.

[50] A. K. Geim, and K. S. Novoselov, "The rise of graphene", Nature Mater. vol. **6**, pp 183-191, 2007.

[51] K. S. Novoselov, V. I. Falko, L. Colombo, P. R. Gellert, M. G. Schwab, and K. Kim, "A roadmap for graphene", Nature vol. **490**, pp 192-200, 2012.

[52] A. C. Ferrari, F. Bonaccorso, V. Fal'ko, K. S. Novoselov, S. Roche, P. Boggild, S. Borini, F. H. L. Koppens, V. Palermo, N. Pugno *et al.*, "Science and technology roadmap for graphene, related two-dimensional crystals, and hybrid systems", Nanoscale vol. **7**, pp 4598-4810, 2015.

[53] N. Lindvall, "Licentiate thesis: Towards graphene-based devices: Fabrication and characterization", Chalmers University of Technology, Department of Microtechnology and Nanoscience (MC2), ISSN 1652-0769, MC2-230, 2012.

[54] A. H. Castro Neto, F. Guinea, N. M. R. Peres, K. S. Novoselov, and A. K. Geim, "The electronic properties of graphene", Rev. Mod. Phys. vol. **81**, pp 109-162, 2009.

[55] M. I. Katsnelson, K. S. Novoselov, and A. K. Geim, "Chiral tunnelling and the Klein paradox in graphene", Nature Phys. vol. **2**, pp 620-625, 2006.

[56] J. M. Chen, J. Y. Xi, D. Wang, and Z. G. Shuai, "Carrier Mobility in Graphyne Should Be Even Larger than That in Graphene: A Theoretical Prediction", J. Phys. Chem. Lett. vol. **4**, pp 1443-1448, 2013.

[57] K. I. Bolotin, K. J. Sikes, J. Hone, H. L. Stormer, and P. Kim, "Temperature-dependent transport in suspended graphene", Phys. Rev. Lett. vol. **101**, 2008.

[58] S. Kim, J. Nah, I. Jo, D. Shahrjerdi, L. Colombo, Z. Yao, E. Tutuc, and S. K. Banerjee, "Realization of a high mobility dual-gated graphene field-effect transistor with Al_2O_3 dielectric", Appl. Phys. Lett. vol. **94**, p. 062107, 2009.

[59] M. Shayegan, "Flatland electrons in high magnetic fields", arXiv:cond-mat/0505520v1, 2005.

[60] K. von Klitzing, G. Dorda, and M. Pepper, "New method for high-accuracy determination of the fine-structure constant based on quantized Hall resistance", Phys. Rev. Lett. vol. **45**, pp 494-497, 1980.

[61] K. S. Novoselov, E. McCann, S. V. Morozov, V. I. Fal'ko, M. I. Katsnelson, U. Zeitler, D. Jiang, F. Schedin, and A. K. Geim, "Unconventional quantum Hall effect and Berry's phase of 2 pi in bilayer graphene", Nature Phys. vol. **2**, pp 177-180, 2006.

[62] C. W. J. Beenakker, and H. Vanhouten, "Quantum transport in semiconductor nanostructures", Solid State Phys. vol. **44**, pp 1-228, 1991.

[63] C. Kittel, "Introduction to solid state physics", pp 543-544, Wiley, 2005.

[64] V. T. Petrashov, V. N. Antonov, P. Delsing, and R. Claeson, "Phase memory effects in mesoscopic rings with superconducting ‘‘mirrors’’", Phys. Rev. Lett. vol. **70**, pp 347-350, 1993.

[65] V. T. Petrashov, V. N. Antonov, R. S. Shaikhaidarov, S. V. Maksimov, P. Meeson, R. Souhami, and M. Springford, ""Giant" Aharonov-Bohm effect in mesoscopic silver rings with bismuth electrodes", Europhys. Lett. vol. **34**, pp 593-598, 1996.

[66] B. J. F. Lin, M. A. Paalanen, A. C. Gossard, and D. C. Tsui, "Weak Localization of Two-Dimensional Electrons in Gaas-Alxga1-Xas Heterostructures", Phys. Rev. B vol. **29**, pp 927-934, 1984.

[67] G. Bergmann, "Physical Interpretation of Weak Localization - a Time-of-Flight Experiment with Conduction Electrons", Phys. Rev. B vol. **28**, pp 2914-2920, 1983.

[68] F. V. Tikhonenko, A. A. Kozikov, A. K. Savchenko, and R. V. Gorbachev, "Transition between Electron Localization and Antilocalization in Graphene", Phys. Rev. Lett. vol. **103**, 2009.

[69] F. V. Tikhonenko, D. W. Horsell, R. V. Gorbachev, and A. K. Savchenko, "Weak localization in graphene flakes", Phys. Rev. Lett. vol. **100**, 2008.

[70] S. V. Morozov, K. S. Novoselov, M. I. Katsnelson, F. Schedin, L. A. Ponomarenko, D. Jiang, and A. K. Geim, "Strong suppression of weak localization in graphene", Phys. Rev. Lett. vol. **97**, 2006.

[71] A. M. R. Baker, J. A. Alexander-Webber, T. Altebaeumer, T. J. B. M. Janssen, A. Tzalenchuk, S. Lara-Avila, S. Kubatkin, R. Yakimova, C. T. Lin, L. J. Li *et al.*, "Weak localization scattering lengths in epitaxial, and CVD graphene", Phys. Rev. B vol. **86**, 2012.

[72] E. McCann, K. Kechedzhi, V. I. Fal'ko, H. Suzuura, T. Ando, and B. L. Altshuler, "Weak-localization magnetoresistance and valley symmetry in graphene", Phys. Rev. Lett. vol. **97**, 2006.

[73] J. Rammer, and A. L. Shelankov, "Weak localization in inhomogeneous magnetic fields", Phys. Rev. B vol. **36**, pp 3135-3146, 1987.

[74] S. J. Bending, K. von Klitzing, and K. Ploog, "Weak localization in a distribution of magnetic flux tubes", Phys. Rev. Lett. vol. **65**, pp 1060-1063, 1990.

[75] A. K. Geim, "Nonlocal Magnetoresistance of Bismuth-Films in Nonuniform Field of Abrikosov Vortices", JETP Lett. vol. **50**, pp 389-393, 1989.

[76] A. K. Geim, S. J. Bending, I. V. Grigorieva, and M. G. Blamire, "Ballistic 2-Dimensional Electrons in a Random Magnetic-Field", Phys. Rev. B vol. **49**, pp 5749-5752, 1994.

[77] A. Smith, R. Taboryski, L. T. Hansen, C. B. Sorensen, P. Hedegard, and P. E. Lindelof, "Magnetoresistance of a 2-Dimensional Electron-Gas in a Random Magnetic-Field", Phys. Rev. B vol. **50**, pp 14726-14729, 1994.

[78] M. R. Masir, and F. M. Peeters, "Scattering of Dirac electrons by a random array of magnetic flux tubes", J. Comput. Electron. vol. **12**, pp 115-122, 2013.

[79] M. R. Masir, P. Vasilopoulos, and F. M. Peeters, "Graphene in inhomogeneous magnetic fields: bound, quasi-bound and scattering states", J. Phys.-Condens. Mat. vol. **23**, 2011.

[80] P. Roy, T. K. Ghosh, and K. Bhattacharya, "Localization of Dirac-like excitations in graphene in the presence of smooth inhomogeneous magnetic fields", J. Phys.-Condens. Mat. vol. **24**, 2012.

[81] A. A. Abrikosov, "On the Magnetic Properties of Superconductors of the Second Group", JETP Lett. vol. **5**, pp 1174-1183, 1957.

[82] L. Kuzmin, "Ultimate cold-electron bolometer with strong electrothermal feedback", P. Soc. Photo-Opt. Ins. vol. **5498**, pp 349-361, 2004.

[83] A. T. Lee, P. L. Richards, S. W. Nam, B. Cabrera, and K. D. Irwin, "A superconducting bolometer with strong electrothermal feedback", Appl. Phys. Lett. vol. **69**, pp 1801-1803, 1996.

[84] P. L. Richards, "Bolometers for Infrared and Millimeter Waves", J. Appl. Phys. vol. **76**, pp 1-24, 1994.

[85] P. Blake, E. W. Hill, A. H. C. Neto, K. S. Novoselov, D. Jiang, R. Yang, T. J. Booth, and A. K. Geim, "Making graphene visible", Appl. Phys. Lett. vol. **91**, p. 063124, 2007.

[86] A. C. Ferrari, and J. Robertson, "Interpretation of Raman spectra of disordered and amorphous carbon", Phys. Rev. B vol. **61**, pp 14095-14107, 2000.

[87] M. S. Dresselhaus, A. Jorio, M. Hofmann, G. Dresselhaus, and R. Saito, "Perspectives on carbon nanotubes and graphene Raman spectroscopy", Nano Lett. vol. **10**, pp 751-758, 2010.

[88] A. C. Ferrari, "Raman spectroscopy of graphene and graphite: Disorder, electron-phonon coupling, doping and nonadiabatic effects", Solid State Commun. vol. **143**, pp 47-57, 2007.

[89] A. C. Ferrari, J. C. Meyer, V. Scardaci, C. Casiraghi, M. Lazzeri, F. Mauri, S. Piscanec, D. Jiang, K. S. Novoselov, S. Roth *et al.*, "Raman spectrum of graphene and graphene layers", Phys. Rev. Lett. vol. **97**, 2006.

[90] L. G. Cancado, A. Jorio, E. H. M. Ferreira, F. Stavale, C. A. Achete, R. B. Capaz, M. V. O. Moutinho, A. Lombardo, T. S. Kulmala, and A. C. Ferrari, "Quantifying Defects in Graphene via Raman Spectroscopy at Different Excitation Energies", Nano Lett. vol. **11**, pp 3190-3196, 2011.

[91] M. M. Lucchese, F. Stavale, E. H. M. Ferreira, C. Vilani, M. V. O. Moutinho, R. B. Capaz, C. A. Achete, and A. Jorio, "Quantifying ion-induced defects and Raman relaxation length in graphene", Carbon vol. **48**, pp 1592-1597, 2010.

[92] C. Virojanadara, M. Syvajarvi, R. Yakimova, L. I. Johansson, A. A. Zakharov, and T. Balasubramanian, "Homogeneous large-area graphene layer growth on 6H-SiC(0001)", Phys. Rev. B vol. **78**, 2008.

[93] Y. Hernandez, V. Nicolosi, M. Lotya, F. M. Blighe, Z. Y. Sun, S. De, I. T. McGovern, B. Holland, M. Byrne, Y. K. Gun'ko *et al.*, "High-yield production of graphene by liquid-phase exfoliation of graphite", Nature Nanotech. vol. **3**, pp 563-568, 2008.

[94] G. Eda, G. Fanchini, and M. Chhowalla, "Large-area ultrathin films of reduced graphene oxide as a transparent and flexible electronic material", Nature Nanotech. vol. **3**, pp 270-274, 2008.

[95] J. M. Cai, P. Ruffieux, R. Jaafar, M. Bieri, T. Braun, S. Blankenburg, M. Muoth, A. P. Seitsonen, M. Saleh, X. L. Feng *et al.*, "Atomically precise bottom-up fabrication of graphene nanoribbons", Nature vol. **466**, pp 470-473, 2010.

[96] B. S. Jessen, M. B. Klarskov, L. K. Tschammer, T. J. Booth, and P. Bøggild, "Automatic identification of single- and/or few-layer thin-film material", US Patent application US 14/419,869, filed 2013.

[97] Y. F. Hao, M. S. Bharathi, L. Wang, Y. Y. Liu, H. Chen, S. Nie, X. H. Wang, H. Chou, C. Tan, B. Fallahazad *et al.*, "The Role of Surface Oxygen in the Growth of Large Single-Crystal Graphene on Copper", Science vol. **342**, pp 720-723, 2013.

[98] W. Gannett, W. Regan, K. Watanabe, T. Taniguchi, M. F. Crommie, and A. Zettl, "Boron nitride substrates for high mobility chemical vapor deposited graphene", Appl. Phys. Lett. vol. **98**, 2011.

[99] I. Vlassiouk, M. Regmi, P. F. Fulvio, S. Dai, P. Datskos, G. Eres, and S. Smirnov, "Role of hydrogen in chemical vapor deposition growth of large single-crystal graphene", ACS Nano vol. **5**, pp 6069-6076, 2011.

[100] A. W. Weimer, J. Dahl, K. Buechler, A. Lewandowski, R. Pitts, C. Bingham, and G. Glatzmaier, "Thermal dissociation of methane using a solar coupled aerosol flow reactor", Proceedings of the 2001 U.S. DOE Hydrogen Program Review, NREL/CP-610-30535, pp 228-270, 2001.

[101] A. N. Obraztsov, E. A. Obraztsova, A. V. Tyurnina, and A. A. Zolotukhin, "Chemical vapor deposition of thin graphite films of nanometer thickness", Carbon vol. **45**, pp 2017-2021, 2007.

[102] Y. Zhang, L. Gomez, F. N. Ishikawa, A. Madaria, K. Ryu, C. A. Wang, A. Badmaev, and C. W. Zhou, "Comparison of graphene growth on single-crystalline and polycrystalline Ni by chemical vapor deposition", J. Phys. Chem. Lett. vol. **1**, pp 3101-3107, 2010.

[103] J. F. Colomer, C. Stephan, S. Lefrant, G. Van Tendeloo, I. Willems, Z. Konya, A. Fonseca, C. Laurent, and J. B. Nagy, "Large-scale synthesis of single-wall carbon nanotubes by catalytic chemical vapor deposition (CCVD) method", Chem. Phys. Lett. vol. **317**, pp 83-89, 2000.

[104] C.-a. Di, D. Wei, G. Yu, Y. Liu, Y. Guo, and D. Zhu, "Patterned graphene as source/drain electrodes for bottom-contact organic field-effect transistors", Adv. Mater. vol. **20**, pp 3289-3293, 2008.

[105] S. Nie, W. Wu, S. Xing, Q. Yu, S.-s. Pei, and K. McCarty, "Growth from below: Bilayer graphene on copper by chemical vapor deposition", arXiv:1202.1031v1, 2012.

[106] S. Bhaviripudi, X. T. Jia, M. S. Dresselhaus, and J. Kong, "Role of kinetic factors in chemical vapor deposition synthesis of uniform large area graphene using copper catalyst", Nano Lett. vol. **10**, pp 4128-4133, 2010.

[107] J. Sun, N. Lindvall, M. Cole, K. Angel, T. Wang, K. Teo, D. Chua, J. Liu, and A. Yurgens, "Low partial pressure chemical vapor deposition of graphene on copper", IEEE Trans. Nanotechnol. vol. **11**, pp 255-260, 2012.

[108] L. Tao, J. Lee, H. Chou, M. Holt, R. S. Ruoff, and D. Akinwande, "Synthesis of high quality monolayer graphene at reduced temperature on hydrogen-enriched evaporated copper (111) films", ACS Nano vol. **6**, pp 2319-2325, 2012.

[109] A. Ismach, C. Druzgalski, S. Penwell, A. Schwartzberg, M. Zheng, A. Javey, J. Bokor, and Y. G. Zhang, "Direct chemical vapor deposition of graphene on dielectric surfaces", Nano Lett. vol. **10**, pp 1542-1548, 2010.

[110] G. I. Kozlov, and V. G. Knorre, "Single-pulse shock tube studies on the kinetics of the thermal decomposition of methane", Combustion and Flame vol. **6**, pp 253-263, 1962.

[111] H. L. Cao, Q. K. Yu, L. A. Jauregui, J. Tian, W. Wu, Z. Liu, R. Jalilian, D. K. Benjamin, Z. Jiang, J. Bao *et al.*, "Electronic transport in chemical vapor deposited graphene synthesized on Cu: Quantum Hall effect and weak localization", Appl. Phys. Lett. vol. **96**, 2010.

[112] Y. Lee, S. Bae, H. Jang, S. Jang, S. E. Zhu, S. H. Sim, Y. I. Song, B. H. Hong, and J. H. Ahn, "Wafer-scale synthesis and transfer of graphene films", Nano Lett. vol. **10**, pp 490-493, 2010.

[113] X. S. Li, C. W. Magnuson, A. Venugopal, J. H. An, J. W. Suk, B. Y. Han, M. Borysiak, W. W. Cai, A. Velamakanni, Y. W. Zhu *et al.*, "Graphene films with large domain size by a two-step chemical vapor deposition process", Nano Lett. vol. **10**, pp 4328-4334, 2010.

[114] E. H. Lock, M. Baraket, M. Laskoski, S. P. Mulvaney, W. K. Lee, P. E. Sheehan, D. R. Hines, J. T. Robinson, J. Tosado, M. S. Fuhrer *et al.*, "High-quality uniform dry transfer of graphene to polymers", Nano Lett. vol. **12**, pp 102-107, 2012.

[115] *Optical image from Jie Sun, department of Microtechnology and Nanoscience, Chalmers University of Technology, Gothenburg, Sweden.*

[116] R. Arvidsson, D. Kushnir, S. Molander, and B. A. Sandén, "Energy and resource use assessment of graphene as a substitute for indium tin oxide in transparent electrodes", Journal of Cleaner Production, doi:10.1016/j.jclepro.2015.04.076, 2015.

[117] L. Gao, W. Ren, H. Xu, L. Jin, Z. Wang, T. Ma, L.-P. Ma, Z. Zhang, Q. Fu, L.-M. Peng *et al.*, "Repeated growth and bubbling transfer of graphene with millimetre-size single-crystal grains using platinum", Nat. Commun. vol. **3**, p. 699, 2012.

[118] C. Lockhart de la Rosa, J. Sun, N. Lindvall, M. T. Cole, Y. Nam, M. Löffler, E. Olsson, K. B. K. Teo, and A. Yurgens, "Frame assisted H_2O electrolysis induced H_2 bubbling transfer of large area graphene grown by chemical vapor deposition on Cu", Appl. Phys. Lett. vol. **102**, p. 022101, 2013.

[119] *Adapted with permission from original figure by Jie Sun, department of Microtechnology and Nanoscience, Chalmers University of Technology, Gothenburg, Sweden.*

[120] J. Sun, N. Lindvall, M. T. Cole, T. Wang, T. J. Booth, P. Boggild, K. B. K. Teo, J. Liu, and A. Yurgens, "Controllable chemical vapor deposition of large area uniform nanocrystalline graphene directly on silicon dioxide", J. Appl. Phys. vol. **111**, p. 044103, 2012.

[121] J. Sun, M. T. Cole, N. Lindvall, K. B. K. Teo, and A. Yurgens, "Noncatalytic chemical vapor deposition of graphene on high-temperature substrates for transparent electrodes", Appl. Phys. Lett. vol. **100**, p. 022102, 2012.

[122] J. Sun, N. Lindvall, M. T. Cole, K. B. K. Teo, and A. Yurgens, "Large-area uniform graphene-like thin films grown by chemical vapor deposition directly on silicon nitride", Appl. Phys. Lett. vol. **98**, p. 252107, 2011.

[123] M. A. Fanton, J. A. Robinson, C. Puls, Y. Liu, M. J. Hollander, B. E. Weiland, M. LaBella, K. Trumbull, R. Kasarda, C. Howsare *et al.*, "Characterization of graphene films and transistors grown on sapphire by metal-free chemical vapor deposition", ACS Nano vol. **5**, pp 8062-8069, 2011.

[124] Y. Miyasaka, A. Nakamura, and J. Temmyo, "Graphite thin films consisting of nanograins of multilayer graphene on sapphire substrates directly grown by alcohol chemical vapor deposition", Jpn. J. Appl. Phys. vol. **50**, 2011.

[125] D. Wei, Y. Liu, H. Zhang, L. Huang, B. Wu, J. Chen, and G. Yu, "Scalable synthesis of few-layer graphene ribbons with controlled morphologies by a template method and their applications in nanoelectromechanical switches", J. Am. Chem. Soc. vol. **131**, pp 11147-11154, 2009.

[126] M. H. Rümmeli, A. Bachmatiuk, A. Scott, F. Börrnert, J. H. Warner, V. Hoffman, J.-H. Lin, G. Cuniberti, and B. Büchner, "Direct low-temperature nanographene CVD synthesis over a dielectric insulator", ACS Nano vol. **4**, pp 4206-4210, 2010.

[127] X. Ding, G. Ding, X. Xie, F. Huang, and M. Jiang, "Direct growth of few layer graphene on hexagonal boron nitride by chemical vapor deposition", Carbon vol. **49**, pp 2522-2525, 2011.

[128] J. Hofrichter, B. N. Szafranek, M. Otto, T. J. Echtermeyer, M. Baus, A. Majerus, V. Geringer, M. Ramsteiner, and H. Kurz, "Synthesis of graphene on silicon dioxide by a solid carbon source", Nano Lett. vol. **10**, pp 36-42, 2010.

[129] P. Y. Teng, C. C. Lu, K. Akiyama-Hasegawa, Y. C. Lin, C. H. Yeh, K. Suenaga, and P. W. Chiu, "Remote Catalyzation for Direct Formation of Graphene Layers on Oxides", Nano Lett. vol. **12**, pp 1379-1384, 2012.

[130] A. Oya, and H. Marsh, "Phenomena of catalytic graphitization", J. Mater. Sci. vol. **17**, pp 309-322, 1982.

[131] K.-B. Kim, C.-M. Lee, and J. Choi, "Catalyst-free direct growth of triangular nano-graphene on all substrates", J. Phys. Chem. C vol. **115**, pp 14488-14493, 2011.

[132] R. A. Barton, J. Parpia, and H. G. Craighead, "Fabrication and performance of graphene nanoelectromechanical systems", J. Vac. Sci. Technol. B vol. **29**, p. 050801, 2011.

[133] J. S. Bunch, A. M. van der Zande, S. S. Verbridge, I. W. Frank, D. M. Tanenbaum, J. M. Parpia, H. G. Craighead, and P. L. McEuen, "Electromechanical resonators from graphene sheets", Science vol. **315**, pp 490-493, 2007.

[134] C. Y. Chen, S. Rosenblatt, K. I. Bolotin, W. Kalb, P. Kim, I. Kymissis, H. L. Stormer, T. F. Heinz, and J. Hone, "Performance of monolayer graphene nanomechanical resonators with electrical readout", Nature Nanotech. vol. **4**, pp 861-867, 2009.

[135] Y. H. Xu, C. Y. Chen, V. V. Deshpande, F. A. DiRenno, A. Gondarenko, D. B. Heinz, S. M. Liu, P. Kim, and J. Hone, "Radio frequency electrical transduction of graphene mechanical resonators", Appl. Phys. Lett. vol. **97**, p. 243111, 2010.

[136] A. M. van der Zande, R. A. Barton, J. S. Alden, C. S. Ruiz-Vargas, W. S. Whitney, P. H. Q. Pham, J. Park, J. M. Parpia, H. G. Craighead, and P. L. McEuen, "Large-Scale Arrays of Single-Layer Graphene Resonators", Nano Lett. vol. **10**, pp 4869-4873, 2010.

[137] M. Wiesner, N. Lindvall, and A. Yurgens, "Detection of graphene microelectromechanical system resonance", J. Appl. Phys. vol. **116**, p. 224510, 2014.

[138] K. I. Bolotin, K. J. Sikes, Z. Jiang, M. Klima, G. Fudenberg, J. Hone, P. Kim, and H. L. Stormer, "Ultrahigh electron mobility in suspended graphene", Solid State Commun. vol. **146**, pp 351-355, 2008.

[139] G. Bergmann, "Weak localization in thin-films - a time-of-flight experiment with conduction electrons", Phys. Rep. vol. **107**, pp 1-58, 1984.

[140] Y. Wang, and J. J. Santiago-Aviles, "Large negative magnetoresistance and strong localization in highly disordered electrospun pregraphitic carbon nanofiber", Appl. Phys. Lett. vol. **89**, 2006.

[141] X. Zhang, Q. Z. Xue, and D. D. Zhu, "Positive and negative linear magnetoresistance of graphite", Phys. Lett. A vol. **320**, pp 471-477, 2004.

[142] A. Faisst, and H. von Lohneysen, "Electrical resistance and magnetoresistance of pyrocarbon at low temperatures in fields up to 14 Tesla", Carbon vol. **40**, pp 321-327, 2002.

[143] V. I. Fal'ko, K. Kechedzhi, E. McCann, B. L. Altshuler, H. Suzuura, and T. Ando, "Weak localization in graphene", Solid State Commun. vol. **143**, pp 33-38, 2007.

[144] *Raman measurement by Matthew Cole, department of Engineering, University of Cambridge, Cambridge, United Kingdom.*

[145] M. A. Tamor, and W. C. Vassell, "Raman fingerprinting of amorphous-carbon films", J. Appl. Phys. vol. **76**, pp 3823-3830, 1994.

[146] J. Schwan, S. Ulrich, V. Batori, H. Ehrhardt, and S. R. P. Silva, "Raman spectroscopy on amorphous carbon films", J. Appl. Phys. vol. **80**, pp 440-447, 1996.

[147] J. Kotakoski, A. V. Krasheninnikov, U. Kaiser, and J. C. Meyer, "From point defects in graphene to two-dimensional amorphous carbon", Phys. Rev. Lett. vol. **106**, 2011.

[148] *TEM image from Olof Bäcke, Markus Löffler, and Eva Olsson from Micropscopy and Microanalysis, Chalmers University of Technology, Gothenburg, Sweden.*

[149] *TEM images from Tim Booth and Peter Bøggild from Micro- and Nanotechnology, DTU Nanotech, Copenhagen, Denmark.*

[150] B. Song, G. F. Schneider, Q. Xu, G. Pandraud, C. Dekker, and H. Zandbergen, "Atomic-scale electron-beam sculpting of near-defect-free graphene nanostructures", Nano Lett. vol. **11**, pp 2247-2250, 2011.

[151] C. O. Girit, J. C. Meyer, R. Erni, M. D. Rossell, C. Kisielowski, L. Yang, C. H. Park, M. F. Crommie, M. L. Cohen, S. G. Louie *et al.*, "Graphene at the edge: Stability and dynamics", Science vol. **323**, pp 1705-1708, 2009.

[152] R. F. Egerton, P. Li, and M. Malac, "Radiation damage in the TEM and SEM", Micron vol. **35**, pp 399-409, 2004.

[153] J. R. Jinschek, E. Yucelen, H. A. Calderon, and B. Freitag, "Quantitative atomic 3-D imaging of single/double sheet graphene structure", Carbon vol. **49**, pp 556-562, 2011.

[154] J. Abrahamson, "The surface energies of graphite", Carbon vol. **11**, pp 337-362, 1973.

[155] J. Biscoe, and B. E. Warren, "An X-Ray study of carbon black", J. Appl. Phys. vol. **13**, pp 364-371, 1942.

[156] L. Fulcheri, and Y. Schwob, "From methane to hydrogen, carbon black and water", Int. J. Hydrogen Energ. vol. **20**, pp 197-202, 1995.

[157] N. Z. Muradov, and T. N. Veziroğlu, "From hydrocarbon to hydrogen–carbon to hydrogen economy", Int. J. Hydrogen Energ. vol. **30**, pp 225-237, 2005.

[158] I. Khrapach, F. Withers, T. H. Bointon, D. K. Polyushkin, W. L. Barnes, S. Russo, and M. F. Craciun, "Novel Highly Conductive and Transparent Graphene-Based Conductors", Adv. Mater. vol. **24**, pp 2844-2849, 2012.

[159] S. Adam, E. H. Hwang, V. M. Galitski, and S. Das Sarma, "A self-consistent theory for graphene transport", PNAS vol. **104**, pp 18392-18397, 2007.

[160] J. Martin, N. Akerman, G. Ulbricht, T. Lohmann, J. H. Smet, K. Von Klitzing, and A. Yacoby, "Observation of electron-hole puddles in graphene using a scanning single-electron transistor", Nature Phys. vol. **4**, pp 144-148, 2008.

[161] E. A. Kim, and A. H. C. Neto, "Graphene as an electronic membrane", Europhys. Lett. vol. **84**, 2008.

[162] J. H. Chen, C. Jang, S. Adam, M. S. Fuhrer, E. D. Williams, and M. Ishigami, "Charged-impurity scattering in graphene", Nature Phys. vol. **4**, pp 377-381, 2008.

[163] Y. B. Zhang, V. W. Brar, C. Girit, A. Zettl, and M. F. Crommie, "Origin of spatial charge inhomogeneity in graphene", Nature Phys. vol. **5**, pp 722-726, 2009.

[164] Y. P. Dan, Y. Lu, N. J. Kybert, Z. T. Luo, and A. T. C. Johnson, "Intrinsic response of graphene vapor sensors", Nano Lett. vol. **9**, pp 1472-1475, 2009.

[165] X. Du, I. Skachko, A. Barker, and E. Y. Andrei, "Approaching ballistic transport in suspended graphene", Nature Nanotech. vol. **3**, pp 491-495, 2008.

[166] F. Chen, J. L. Xia, D. K. Ferry, and N. J. Tao, "Dielectric screening enhanced performance in graphene FET", Nano Lett. vol. **9**, pp 2571-2574, 2009.

[167] M. Ishigami, J. H. Chen, W. G. Cullen, M. S. Fuhrer, and E. D. Williams, "Atomic structure of graphene on SiO_2", Nano Lett. vol. **7**, pp 1643-1648, 2007.

[168] A. Reina, H. Son, L. Jiao, B. Fan, M. S. Dresselhaus, Z. Liu, and J. Kong, "Transferring and identification of single- and few-layer graphene on arbitrary substrates", J. Phys. Chem. C vol. **112**, pp 17741-17744, 2008.

[169] Z. Cheng, Q. Zhou, C. Wang, Q. Li, C. Wang, and Y. Fang, "Toward intrinsic graphene surfaces: A systematic study on thermal annealing and wet-chemical treatment of SiO_2-supported graphene devices", Nano Lett. vol. **11**, pp 767-771, 2011.

[170] A. Nourbakhsh, M. Cantoro, A. Klekachev, F. Clemente, B. Sorée, M. H. van der Veen, T. Vosch, A. Stesmans, B. Sels, and S. De Gendt, "Tuning the Fermi level of SiO_2-supported single-layer graphene by thermal annealing", J. Phys. Chem. C vol. **114**, pp 6894-6900, 2010.

[171] W. Z. Bao, F. Miao, Z. Chen, H. Zhang, W. Y. Jang, C. Dames, and C. N. Lau, "Controlled ripple texturing of suspended graphene and ultrathin graphite membranes", Nature Nanotech. vol. **4**, pp 562-566, 2009.

[172] J. Moser, A. Barreiro, and A. Bachtold, "Current-induced cleaning of graphene", Appl. Phys. Lett. vol. **91**, p. 163513, 2007.

[173] Y. D. Kim, H. Kim, Y. Cho, J. H. Ryoo, C.-H. Park, P. Kim, Y. S. Kim, S. Lee, Y. Li, S.-N. Park *et al.*, "Bright visible light emission from graphene", Nature Nanotech. vol. **10**, pp 676-681, 2015.

[174] Z. Liu, P. Boggild, J. R. Yang, Y. Cheng, F. Grey, Y. L. Liu, L. Wang, and Q. S. Zheng, "A graphite nanoeraser", Nanotechnology vol. **22**, p. 265706, 2011.

[175] R. Jalilian, L. A. Jauregui, G. Lopez, J. F. Tian, C. Roecker, M. M. Yazdanpanah, R. W. Cohn, I. Jovanovic, and Y. P. Chen, "Scanning gate microscopy on graphene: Charge inhomogeneity and extrinsic doping", Nanotechnology vol. **22**, p. 295705, 2011.

[176] A. M. Goossens, V. E. Calado, A. Barreiro, K. Watanabe, T. Taniguchi, and L. M. K. Vandersypen, "Mechanical cleaning of graphene", Appl. Phys. Lett. vol. **100**, p. 073110, 2012.

[177] N. Lindvall, A. Kalabukhov, and A. Yurgens, "Cleaning graphene using atomic force microscope", J. Appl. Phys. vol. **111**, pp 064904-064904, 2012.

[178] F. Giannazzo, S. Sonde, V. Raineri, G. Patane, G. Compagnini, F. Aliotta, R. Ponterio, and E. Rimini, "Optical, morphological and spectroscopic characterization of graphene on SiO_2", Phys. Status Solidi C vol. **7**, pp 1251-1255, 2010.

[179] P. K. Day, H. G. LeDuc, B. A. Mazin, A. Vayonakis, and J. Zmuidzinas, "A broadband superconducting detector suitable for use in large arrays", Nature vol. **425**, pp 817-821, 2003.

[180] A. J. Miller, S. W. Nam, J. M. Martinis, and A. V. Sergienko, "Demonstration of a low-noise near-infrared photon counter with multiphoton discrimination", Appl. Phys. Lett. vol. **83**, pp 791-793, 2003.

[181] J. Yan, M. H. Kim, J. A. Elle, A. B. Sushkov, G. S. Jenkins, H. M. Milchberg, M. S. Fuhrer, and H. D. Drew, "Dual-gated bilayer graphene hot-electron bolometer", Nature Nanotech. vol. **7**, pp 472-478, 2012.

[182] M. Tarasov, N. Lindvall, L. Kuzmin, and A. Yurgens, "Family of graphene-based superconducting devices", JETP Lett. vol. **94**, pp 329-332, 2011.

[183] J. C. Johannsen, S. Ulstrup, M. Bianchi, R. Hatch, D. Guan, F. Mazzola, L. Hornekaer, F. Fromm, C. Raidel, T. Seyller *et al.*, "Electron-phonon coupling in quasi-free-standing graphene", J. Phys.-Condens. Mat. vol. **25**, 2013.

[184] Y. Nam, N. Lindvall, J. Sun, Y. W. Park, and A. Yurgens, "Graphene p–n–p junctions controlled by local gates made of naturally oxidized thin aluminium films", Carbon vol. **50**, pp 1987-1992, 2012.

[185] S. Russo, J. B. Oostinga, D. Wehenkel, H. B. Heersche, S. S. Sobhani, L. M. K. Vandersypen, and A. F. Morpurgo, "Observation of Aharonov-Bohm conductance oscillations in a graphene ring", Phys. Rev. B vol. **77**, 2008.

[186] J. S. Yoo, Y. W. Park, V. Skakalova, and S. Roth, "Shubnikov-de Haas and Aharonov Bohm effects in a graphene nanoring structure", Appl. Phys. Lett. vol. **96**, 2010.

[187] M. Huefner, F. Molitor, A. Jacobsen, A. Pioda, C. Stampfer, K. Ensslin, and T. Ihn, "The Aharonov-Bohm effect in a side-gated graphene ring", New J. Phys. vol. **12**, 2010.

[188] M. Huefner, F. Molitor, A. Jacobsen, A. Pioda, C. Stampfer, K. Ensslin, and T. Ihn, "Investigation of the Aharonov-Bohm effect in a gated graphene ring", Phys. Status Solidi B vol. **246**, pp 2756-2759, 2009.

[189] A. Rycerz, "Aharonov-Bohm effect and valley polarization in nanoscopic graphene rings", Acta Phys. Pol. A vol. **115**, pp 322-325, 2009.

[190] P. Recher, B. Trauzettel, A. Rycerz, Y. M. Blanter, C. W. J. Beenakker, and A. F. Morpurgo, "Aharonov-Bohm effect and broken valley degeneracy in graphene rings", Phys. Rev. B vol. **76**, 2007.

[191] Y. Nam, J. S. Yoo, Y. W. Park, N. Lindvall, T. Bauch, and A. Yurgens, "The Aharonov-Bohm effect in graphene rings with metal mirrors", Carbon vol. **50**, pp 5562-5568, 2012.

[192] E. Altshuler, and T. H. Johansen, "Colloquium: Experiments in vortex avalanches", Rev. Mod. Phys. vol. **76**, pp 471-487, 2004.

[193] M. S. Welling, R. J. Westerwaal, W. Lohstroh, and R. J. Wijngaarden, "Huge compact flux avalanches in superconducting Nb thin films", Physica C vol. **411**, pp 11-17, 2004.

Appended papers